# INVESTIGATING MECHANISMS OF ANTIANDROGEN RESISTANCE IN HUMAN PROSTATE CANCER

by

Zeda Zhang

A Dissertation
Presented to the Faculty of the Louis V. Gerstner, Jr.
Graduate School of Biomedical Sciences,
Memorial Sloan Kettering Cancer Center
In Partial Fulfillment of the Requirement for the degree of
Doctor of Philosophy

New York, NY
September 2020

| | |
|---|---|
| Charles L. Sawyers, MD | Date |
| Dissertation Mentor | |

# DEDICATION

I would like to dedicate this thesis to my parents: Jianjun Zhang and Li Cai. Without their unconditional support, none of these would have been possible.

# ABSTRACT

Despite the development of highly effective next-generation antiandrogens, acquired resistance to hormone therapy remains a major challenge in the treatment of advanced prostate cancer (PCa). Through the analysis of mouse models, prostate organoid culture, and clinical samples, we find that cancer-associated fibroblasts (CAF) can promote resistance to antiandrogen therapy through secretion of neuregulin 1 (NRG1). Through biochemical purification, we identified NRG1 as the critical resistance factor in CAF supernatant, which promotes resistance in tumor cells through the activation of HER3. Pharmacological blockade of the NRG1/HER3 axis using clinical-grade blocking antibodies re-sensitized tumors to hormone deprivation in vitro and in vivo. Furthermore, patients with castration-resistant prostate cancer with elevated tumor NRG1 activity have a statistically inferior response to next-generation antiandrogen therapy. Taken together, this work reveals a paracrine mechanism of antiandrogen resistance in prostate cancer amenable to clinical testing using currently available targeted therapies.

## ACKNOWLEDGEMENTS

I would first like to thank my thesis advisor Dr. Charles Sawyers for his tremendous support and very responsible mentorship during my Ph.D. Dr. Sawyers has been provided me critical guidance to my scientific career and I truly respect him. During the past six years, I have learned enormously from him, from a scientific standpoint as well as from a great human being and citizen. I would thank Dr. Ping Mu, a former postdoc fellow in the Sawyers lab and now an assistant professor at UT Southwestern Medical Center, who is the person that brought me into the lab and taught me almost everything during my first 4 years of Ph.D. He taught me always to fight against obstacles and never give up. His competitive spirit and resilience have a great impact on me and help me go through some most difficult times. Here I also have a special thanks to one of my best friends Zeyu Chen, who always gave me support towards my research career and also gave me the biggest support during my most difficult times in graduate school. And I was fortunate to make it. I would then thank Dr. Wouter Karthaus, who is my colleague and one of the smartest scientists I ever met. With his help (and also lab mentorship), I finally generated my first meaningful data and really begin to move forward my thesis project. Following my graduate school, Dr. Karthaus has continuously provided me critical input both in research projects and in future directions. I would also thank Dr. Xuejun Jiang, professor at the Cell Biology Program. Dr. Jiang has provided me critical help with his unique biochemical skills. I spent a year and a half working closely with him and we were finally able to purify the resistance-promoting factor that is secreted by cancer-associated fibroblasts. This is really the most important step that finally turned my thesis project around. Without his help and expertise, this project will never be finished. I would also like to thank Dr. Philip Watson, who was a senior scientist in the lab and now our lab manager. He has made the initial observation that CWR22Pc cancer-associated fibroblasts may have some protective effect on cancer cells in an in

vitro culture mixture. Starting from his observation, I have spent the past 6 years embarking on this project and was very fortunate to have it published (* by the time when the thesis was written, it was accepted at Cancer Cell). As a non-native English speaker, I would also thank Drs. Liz Adams and Cynthia Jung, who have helped me tremendously in my English writing, both of them have spent lots of time unselfishly helped me editing my grammars and wordings for nearly every single grant application and manuscripts. I would also thank every other lab members who helped me with my writing (Wouter K, Elizabeth W., and others). I would like to thank Dr. Rohit Bose, who was a clinical fellow in the lab and now an assistant professor at UCSF. Dr. Bose not only gave me very informative scientific suggestions on how to dig out new biology and how to propose new concepts that are clinically relevant, but he also taught me tremendously in terms of interpersonal relationship and managing skills, which are critical in every aspect. I would also like to thank Chao Wu, Young Sun Lee, Ninghui Mao, Chuanli Zhou, and Xiaoling Li, who have helped me tremendously with experiments during the past few years. Without your help, I cannot finish all three projects together. I would also express my gratitude to Vianne Gao and Menghan Liu, who have provided their computational expertise to help analyze high-throughput data from both patient samples and from my experimental systems (RNA-seq). Without Vianne's help, this paper will never pass the editor's hand. And Menghan's timely analysis helped us to finish revisions very smoothly.

I also have a tremendous thanks to all the people in Dr. Xiaodong Wang's lab at the National Institute of Biological Sciences, Beijing (NIBS), where I first received rigorously scientific training in modern cell and molecular biology. It is the place where I decided to dedicate myself to study cancer biology with a personal aim to bring benefits to patients in one day. Without my special experience at NIBS, it is impossible to go to this world-class Memorial Sloan Kettering Cancer Center to pursue my Ph.D. in Cancer Biology, and without Dr. Wang's insight and encouragement, I would never join Dr. Sawyers' laboratory to do my Ph.D. I have tremendous respect for Dr. Wang, who is truly a role model to me as a great scientist with his ambition, high-standard, and his vision. His enterprise is a rare example that truly changes lots of cancer patients destine, which I am also aspired to achieve in one day. Experience at NIBS lays a critical foundation for my next stage of career as a graduate student, where I have a special thanks to Dr. Weiliang Fan, who was a postdoc fellowship in the Wang lab. Dr. Fan obtained his Ph.D. at Zhejiang-UC Berkeley University and published multiple first-author papers within three years. He is my lab role model, as he is ambitious, dedicated, smart but at the same time a very caring person with great humanity. He turned down several offers from top labs in the US but chose to join the Wang lab at NIBS and explained that:" I want to make truly important scientific discoveries in Wang lab, but not just high-profile CNS papers from a flashy lab". His words have rooted deep in my heart and become one of the mottoes that I will always remember. I would also like to thank Dr. Jiang Xian, who was a graduate student and now a postdoc fellow at Stanford University. She is my first lab mentor who provided my first experience in molecular biology during the SURP program at NIBS. I would also thank Dr. Chenjie Pan, who was a graduate student and now a postdoc fellow at Stanford University. He is my best friend and colleague in the Wang lab and I respected his hard-will and his spirit of never-give-up. There are great personals that have a huge positive impact on my scientific career.

Finally, I want to thank my parents, Jianjun Zhang, and Li Cai. I also have a special thanks to my partner Menghan Liu for her support and encouragement and her patience and tolerance throughout my Ph.D. None of these can be done without their dedication and unconditional love.

# TABLE OF CONTENTS

## LIST OF TABLES

## LIST OF FIGURES

# LIST OF ABBREVIATIONS

ADT: Androgen deprivation therapy

AR: Androgen receptor

CAF: Cancer-associated fibroblast

CRPC: Castration-resistant prostate cancer

GEMM: Genetically engineered mouse model

GR: Glucocorticoid receptor

NRG1: Neuregulin 1

PCa: Prostate cancer

PI3K: Phosphoinositide 3-kinase

RTK: Receptor tyrosine kinase

TME: Tumor microenvironment

# INTRODUCTION

## *Epidemiology of human prostate cancer*

According to cancer statistics 2020, prostate cancer is the most commonly diagnosed cancer in men in the US (*3*). It is also the second leading cause of cancer death in man and therefore causes a significant social-economical burden. While the overall incidence of prostate cancer is higher in the western population, this disease is most aggressive in African American populations (*4*). Although the current incidence of prostate cancer in the Asian population is relatively low, it is also fast accelerated (*5*). Worldwide, prostate cancer is the second most common malignancies (after lung cancer), accounting for more than 1 million newly diagnosed cases each year, the majority of which are diagnosed in elderly man ( > 65 years) (*6*). When diagnosed in an early stage, localized prostate cancer is highly curable by surgery. However, there is currently no cure when the disease becomes metastatic (*7*).

## *Understanding from a normal prostate*

A male prostate is an exocrine gland that mainly functions to provide prostatic fluid that contributes to the volumes of semen. The alkalic nature of prostatic fluid neutralizes the acid environment in the vaginal tract and thus protect spermatozoon (8). The development of the prostate has been intensively studied from the past 30 years and is thought to originate from the embryonic urogenital sinus (UGS) (9). A mature prostate epithelium is composed of luminal secretory cells, basal cells as well as a rare population of neuroendocrine cells (10). During development, signaling cross-talk between different prostate epithelial cells as well as their surrounding stromal cells plays an essential role in tissue specification as well as maturation. Prostate epithelium and its surrounding stroma express a high level of androgen receptor and therefore are highly responsive to endocrine androgen signaling. In mammals, the majority (~85%) of androgen (also called testosterone) is produced from a testis while the rest (~15%) is produced from the hypothalamic-pituitary-adrenal axis (8). The majority of primary prostate cancer is manifested as a "luminal type" of the tumor due to the clinical-pathological knowledge that during the disease initiation stage, the increase of hyperproliferative luminal cells, as well as the reduction of basal cells, is generally observed. A few transcription factors such as NKX3.1 and FOXA1 have recently been shown to play critical roles in the development and morphogenesis of a normal prostate (11, 12). Despite morphological differences across different species, the function of the prostate gland in mammals is relatively conserved (13).

### *Modeling prostate cancer*

Despite large genomic-sequencing efforts, the research of prostate cancer is lagging behind compared to many other cancers including its sexual counterpart breast cancer. One of the biggest obstacles that hinder prostate cancer research is lacking in appropriate, clinically-relevant disease models. In particular, so far we are still not able to faithfully recapitulate the disease onset as well as its primary stage when the tumors are androgen-responsive. This technical limitation has recently been improved with the development of prostate organoid 3D culture technology, where normal or cancer organoid of a prostate from either mouse or patients can be generated and maintained ex vivo (14-16). Besides, several newly developed genetically engineered mouse models (GEMM) of prostate cancer allows us to investigate the development of late-stage prostate cancer under certain oncogenic alterations such as p53, PTEN, RB or MYC (17-19). Most recently, the development of somatic engineering methods such as electroporation in vivo also facilitates the fast modeling of prostate cancer harboring various genetic alterations (20). With advanced disease modeling platform, researchers are now being able to perform functional investigations on how complex genetic alterations seen in patients influence prostate cancer tumorigenesis.

### *Understanding of prostate cancer from its molecular basis*

During the past decade, large genomic sequencing efforts in cancer patients revealed numerous and fruitful genetic abnormalities underlying human cancer including prostate cancer (*21, 22*). While we further appreciate the essential role of androgen receptor in both disease initiation and in advanced castration-resistant prostate cancer, multiple new subclasses of prostate cancer become more evident according to their distinct molecular compositions and distinct clinical phenotypes. For example, SPOP mutations render hyper-sensitivity to antiandrogen therapy, while it is significantly mutually exclusive with ETS-ERG fusion (*23-25*). While the loss of CHD1 is mutually exclusive to PTEN deficiency in primary disease, they tend to co-occur in the advanced castration-resistant prostate cancer (CRPC) (*26-28*). In particular, TP53 alteration is dramatically elevated in CRPC and manifests reduced sensitivity to therapy (*29, 30*). Other genetic alterations such as mutations in a transcription pioneer factor, forkhead box protein A1 (FOXA1), and its oncogenicity was just begun to be revealed (*31-34*). Besides exonic alterations, alterations in intronic regions, as well as large chromosomal rearrangements, deletions, translocations, and amplifications, are also detected through various assays such as long-reads DNA sequencing (*35*). As a complementary approach, functional genomics as a reverse genetics method enables rapid discoveries and validations of numerous tumor suppressor genes through a principle of “loss-of-function” assay (*36*). Such methods also enable the identification of genetic modulators of drug sensitivity (*37*). Limitations of current functional genomics approaches include less efficient in identifying “gain-of-function” oncogenic event as well as to uncover multiple genetic interactions and their functional output simultaneously.

### *Clinical management of human prostate cancer*

While prostate cancer has the second cancer incidence in men worldwide, the 5-year mortality rate is an early-stage disease is less than 5% (*3*). One reason is most of the prostate cancers are indolent disease with a very slow clinical progression. Many patients carry the indolent disease for decades without the need for acute intervention. The other reason being since the prostate gland is not an essential organ, surgery or localized radiotherapy often can clear the diseased organ without devastating complications. However, once the localized primary disease begins to invade to multiple adjacent lymph nodes and eventually form metastasis, the disease becomes most incurable by all means (*38*). Androgen receptor signaling plays a dominant role in prostate cancer at almost every stage of the disease. Targeting the transcriptional activity of the androgen receptor has always been a paradigm in the management of prostate cancer (*7*). Recently, the FDA approval of Enzalutamide (an androgen receptor direct antagonist) as the standard first-line therapy to replace docetaxel-based chemotherapy regimens further solidifies the central roles of androgen receptor signaling in prostate cancer (*39*). Recently, there is an emergence of diverse mechanisms of resistance which encompasses from cancer cell plasticity to heterogeneous composition of the tumor microenvironment. In addition, a more thorough understanding about the prostate cancer genome also generates clinical success with specific driver mutations such as PARP inhibitor (*40*).

### *Mechanisms of resistance to hormone therapy*

Hormone therapy attacks the androgen receptor (AR) signaling in prostate tumors in which AR is a lineage survival factor for luminal cancer cells and plays an essential role in cancer progression and drug resistance (*7*). The second-generation of hormone therapies such as enzalutamide (Enz) or abiraterone is widely used to treat CRPC, however, these agents are not curative and most patients will eventually die from the relapsed disease(*7*). Therefore, elucidating the mechanisms underlying CRPC is critical for developing better therapeutics. Role of the tumor microenvironment in drug resistance Previous efforts to understand Enz resistance focused mainly on cell-intrinsic mechanisms. For instance, a gatekeeper AR F876L mutation converts enzalutamide from an antagonist to agonist; in some cases up-regulation of the glucocorticoid receptor (GR) will promote cancer survival as a result of relief the feedback inhibition of AR; in other cases under certain genetic deficiencies such as TP53 and Rb1 loss, luminal cancers can undergo a lineage switch and thus becomes less dependent on AR signaling; treatment-induced neuroendocrine differentiation is another mechanism of AR-targeted therapy resistance; finally, dysregulation chromatin stability such as loss of CHD1 also facilitates the development of such resistance(*18, 29, 42-45*).

### *Role of the tumor microenvironment in cancer*

Tumor cells constantly exchange signals and nutrients with their local environment. It becomes increasingly clear that microenvironment could strongly influence tumor progression and drug resistance in a variety of cancer types. While only a minority of cancers are directly caused by germline mutations, the majority are linked to somatic mutations and environmental factors(*46*). Growing tumors constantly experience different environmental stress such as nutrient deficiency or hypoxia(*46*). Tumors can often cope with these stresses by rapidly adapting themselves to a different environment. There is increasing evidence implicating the microenvironment (stroma and inflammatory cells) as a driver of drug resistance in various cancers (*47, 48*). Examples include melanoma, glioma, breast, lung, lymphoma, and prostate cancer, where secretion of various growth factors (HGF, WNTs) and cytokines (IL-6, IL-8) have been implicated in resistance to kinase inhibitors or to chemotherapy (*49-54*). In prostate cancer, tumor-infiltrating B lymphocytes and myeloid-derived immune suppressor cells (MDSCs) promote castration-resistant prostate cancer (CRPC) through the production of inflammatory cytokines such as IL-23 (*55, 56*). Fibroblast growth factors (FGFs) can also play a role in CRPC, through autocrine or paracrine production (*57*). The ability of microenvironment cells to promote drug resistance is likely linked to the role of these cells in development and tumor initiation. For example, PTEN loss, TGFBRII loss, or NF-κB activation in the stroma can elicit early neoplastic changes in mammary, prostate and pancreatic epithelium (*58-62*).

### *Receptor tyrosine kinase in cancer*

Receptor tyrosine kinases (RTK) are a family of proteins that have a dual function serving as a cell surface receptor and harboring intracellular enzymatic kinase activity. As cell surface receptors, RTKs have a high binding affinity to a variety of growth factors, cytokines, chemokines and hormones. Upon interacting with these ligands, they go through a conformational change and form dimers or oligomers at their C-terminus where the kinase domain usually locates. Ligand-mediated signal transduction starts from RTKs and therefore they are one of the most important signaling molecules that connecting a cell to its surrounding environment. Among RTKs, the ErbB family of proteins is one of the most intensively studied and plays pivotal roles in both normal physiology and in cancer. In mammals, the ErbB family consists of epidermal growth factor receptor (EGFR) as well as three other highly consensus members ErbB2(HER2), ErbB3(HER3) and ErbB4(HER4). EGFR mutation and HER3 amplification are iconic oncogenic alterations in non-small cell lung cancer and breast cancer, respectively. Although mutations in HER3/HER4 are not common, results from recent basket trials also indicate their clinical importance(*63*). As a monomeric protein, ErbB protein has little activity and not stable. Upon activation, the same or different ErbB members can form either homodimers or heterodimers (i.e HER2/HER3 dimers) and thus reach their full kinase activity. HER2 does not have a known ligand and its normal ligand-mediated kinase activity requires forming heterodimers with other ErbB members. In contrast, HER3 is a pseudo-kinase and has do form heterodimers with other ErbB members to transmit its ligand-mediated signal. The HER2/HER3 heterodimer is among one of the most potent activators of the phosphoinositide 3-kinase (PI3K) pathway, which plays critical roles in many human cancers.

### *Neuregulin 1 (NRG1)*

Neuregulin (NRGs) are a family of growth factors that stimulate the ErbB family RTK proteins(*64, 65*). To date, there are a total of six members in the NRG family (NRG1-6). Among them, NRG1 is the first discovered and the most intensively studied. All NRGs are synthesized as membrane-bound precursors that require proteolytic cleavage by membrane-associated proteases to generate a mature soluble growth factor. Thus, NRGs can function either through direct cell-cell contact or through secretion. All NRGs harbor a central “EGF-like” domain by which they are able to bind to ErbB proteins on the cell surface. Of note, there are an enormous number of isoforms in the NRG proteins (>30 in NRG1 and >15 in NRG3) that are generated by alternative splicing. To date, the isoform-specific functions of NRG proteins are not very clear. NRG-ErbB signaling plays an important role in several physiological processes such as neural development and heart growth(*66-70*). Dysregulation of NRG-ErbB signaling has been implicated in multiple human diseases such as schizophrenia and bipolar disorder(*65*). Recent studies also showed elevated NRG1 activity have tumor-promoting roles in non-small cell lung cancers, breast cancers, ovarian cancers and head-and-neck cancers(*53, 71-73*).

### *Introduction to the thesis*

Although second-generation antiandrogens such as enzalutamide (Enz), abiraterone acetate and apalutamide have significantly improved patient survival, patients rarely achieve complete response even with combinations of the most potent AR signaling inhibitors (*74, 75*). Understanding survival mechanisms in persisting tumor cells are critical to achieve a complete response. A state of drug tolerance or persistence has been characterized in lung adenocarcinoma and melanoma, where transcriptional, epigenetic or metabolic changes induced by treatment render previously susceptible tumors insensitive to the therapy (*76, 77*).

In prostate cancer, efforts to understand resistance to AR targeted therapy have focused mainly on cell-intrinsic mechanisms (*18, 29, 42-44, 78*), however, how does the TME influence response to AR targeted therapy is less known. Indeed, AR expression in prostate stroma plays a crucial role in morphogenesis and maturation of a normal prostate gland (*79, 80*), implicating the potential interactions between AR signaling and the TME.

Further investigation of cancer-associated stromal cells has converged on the concept of reactive stroma, now documented in multiple cancers including pancreas, prostate, breast and colorectal tumors (*81*). In breast and colorectal cancer, the increased reactive stroma is associated with poorer clinical outcomes (*82, 83*). In localized primary prostate cancer, the reactive stroma is often associated with a more aggressive disease, which is often missed through CT-scanning. This thesis aims to understand the mechanisms of how prostate cancer reactive stroma mediates cancer progression resistance to AR targeted therapy.

# MATERIALS AND METHODS

## *Generation of 22Pc-EP and 22Pc-CAF Models*

The CWR22Pc prostate cancer cell line was kindly provided by Marja Nevalainen (*1*). We found that this cell line contained a subpopulation of cells with fibroblast-like morphology that were human EpCAM-negative and confirmed to be of mouse origin. In order to purify tumor cells and mouse fibroblasts, we plated CWR22Pc at 400-800 cells per well (6-well) in 50% conditioned media. Numerous multi-clonal, cancer epithelial islands visually free of fibroblasts were isolated by cloning cylinders and then pooled to derive the pure epithelial subline, CWR22Pc-EP, in short 22Pc-EP. Human EpCAM-negative cancer-associated mouse fibroblasts were obtained by performing mouse-specific H-2K$^b$ and H-2D$^b$ MHC class I sorting (Biolegend #114608) and the FACs purified cancer-associated fibroblasts were termed as CWR22Pc-CAF, in short 22Pc-CAF. Purified 22Pc-EP and 22Pc-CAF cells were transduced with eGFP (SGEP-Renilla) (*84*) or tdTomato (QCXIP-tdTomato, Clontech #9136-1). tdTomato was derived from vector p-tdTomato (Clontech #632531) and cloned into the AgeI and EcoRI sites of QCXIP retroviral vector. Both were and selected with 1μg/mL puromycin (Gibco #A1113803) for 5 days.

## *Tissue and Organoid Cultures*

__*Source of cell line and organoid:*__ LNCaP cells were purchased from ATCC (#CRL-1740™). VCaP cells were purchased from ATCC (#CRL-2876™). 22Rv1 cells were purchased from ATCC (#CRL-2505™). LAPC4 cells were generated in the Sawyers laboratory (*85*). MSK-PCa2 human prostate cancer organoid was generated by Gao et al. at MSKCC (*15*). Trp53$^{\Delta/\Delta}$ and Rb1$^{\Delta/\Delta}$ mouse organoid were generated from GEMM mice by introducing a lentiviral-expressing Cre recombinase (*18*). Pten$^{\Delta/\Delta}$-Rosa26-ERG organoid was generated from GEMM mice (*86*).

*Maintenance of cell line and organoid:* All organoids were maintained according to established organoid culture protocol (*16*). All cell lines and organoids were periodically tested negative for mycoplasma (Lonza #LT07-318). Cell lines used in this study were maintained in a 37°C and 5% $CO_2$ incubator. CWR22Pc, 22Pc-EP, 22Pc-CAF and patient-derived primary CAF cells were cultured in RPMI-1640 with FBS (10%), PenStrep (1%), L-glutamine (1%), sodium pyruvate (1%) and HEPES pH=7.6 (1%). VCaP cells were cultured in DME-HG with FBS (10%), PenStrep (1%), L-glutamine (1%), sodium pyruvate (1%) and HEPES pH=7.6 (1%). 22Pc-EP cells were cultured on collagen I-coated plates. (Fisher Scientific #356450). All serums used in cell culture came from Omega Scientific (FBS, #FB-11, #lot:101943; CSS, #FB-11, #lot: 761007).

*Isolation of Primary CAFs:* Isolation of cancer-associated fibroblasts (CAFs) from mouse tumors or patient samples was performed using a previously established protocol (*87, 88*). For patient-derived CAFs, human tissue acquisition and usage were conducted under approved IRB protocol numbers: 12-001, 12-245, and 90-040.

### *Quantitative Co-Culture Assays*

Day 1: 22Pc-EP$^{eGFP}$ (2500 cells/well) or 22Pc-EP$^{eGFP}$ (2500 cells/well) plus 22Pc-CAF$^{tdTomato}$ (150 cells/well) were plated into black-walled, collagen I collated 96-well plate (Corning™ #356700) to reduce fluorescent background. Day 2: Bicalutamide (10μM) or Enz (1μM) or vehicle (DMSO) was added into each well in triplicates. Fresh media and drugs were replaced every 3 days, and images were taken every 7 days using a ZEISS ZEN Widefield microscope. Individual images were stitched using an automated program from MetaMorph. Fluorescent intensity was quantified using MetaMorph software (MetaMorph Inc). Assays were repeated with at least two independent biological replicates.

### *Conditioned Media Assays*

*Collection: Day 0:* 4x106 CAFs or cancer cells were plated in a 10cm dish. Day 1: cells were washed twice with PBS and replaced with serum-free media. Day 3: the first batch of conditioned media was collected and replaced with serum-free media. Collected conditioned media was filtered with a 0.45μM filter (Millex, #SLHA033SS) to remove cell debris and then stored at 4°C. Day 5: the second batch of conditioned media was collected and filtered. Media from the first and second collections were combined and then concentrated to a 10x (for assays) or 50x stock (for purification) using Vivaspin™ protein concentrator spin columns (Sartorius #VS15T02, #VS6002). Concentrated conditioned media could be stored at 4°C for 2 weeks, or up to 6 months at - 80°C without significant activity loss.

*Antiandrogen Assay:* Day 0: 22Pc-EP (3000 cells/well) or VCaP (5000 cells/well) were plated in 96-well plates. Day 1: conditioned media (10x) was mixed with 10%FBS-containing media at a 1:1 ratio. Antiandrogens (Enz 0.1μM or Bic 10μM) or DMSO was added into the culture (1:1000 dilution). Day 4: media and drugs in each well were replaced. Day 7: cell viability/number was measured by CellTiter-Glo luminescent cell viability assay (Promega #G9243). All assays were repeated in at least two independent biological replicates.

*Androgen Deprivation Assay:* Day 0: 22Pc-EP (3000 cells/well), VCaP (5000 cells/well), LAPC4 (5000 cells/well) or MSK-PCa2 (3000 single-cell organoids/well) cells were plated in 96-well plates. Day 1: conditioned media (10x) was first diluted with serum-free media into a working solution (2.5x) and then mixed with 10% CSS media (charcoal-dextran stripped FBS, hereafter CSS) at a 1:1 ratio. The final experimental media contains 5% CSS and 1.25x conditioned media. For MSK-PCa2, CSS media was replaced with DHT- and EGF- deficient human prostate organoid media. Day 4: cell viability/number was measured by CellTiter-Glo luminescent cell viability assay (Promega #G9243).

*Antiandrogen (enzalutamide or bicalutamide) assay:* Day 0: 22Pc-EP (3000 cells/well), VCaP (5000 cells/well), LAPC4 (5000 cells/well) or MSK-PCa2 (3000 single-cell organoids/well) cells were plated in a 96-well plate in triplicates. Day1: conditioned media (10x) was first diluted with serum-free media into a working solution (2.5x) and then mixed with 10% FBS media at a 1:1 ratio. The final experimental media contains 5% FBS and 1.25x conditioned media (For MSK-PCa2, FBS media was replaced with DHT- and EGF- deficient human prostate organoid media). The mixture was added into the 96-well plate (100µL/mL). Antiandrogen (Enz or Bic) or Veh (DMSO) was also added to the plate. Day 4: media and drug were replaced. For growth curve analysis (Figure 2. Development of an androgen-dependent CWR22Pc system to model tumor-stroma interaction.E,F), cell viability/number was measured by CellTiter-Glo luminescent cell viability assay (Promega #G9243). Day 7: for viability assay or growth curve analysis, cell viability/number was measured by CellTiter-Glo luminescent cell viability assay (Promega #G9243). Enz dosage: 22Pc-EP (0.1µM), VCaP and MSK-PCa2 (1µM), LAPC4 and 22Rv1 (10µM). Bic dosage: 22Pc-EP (10µM).

*RTK Signaling:* Day 0: 22Pc-EP (106 cells/well) cells were plated in a 6-well plate. Day 1: cells were serum-starved for 1hr with serum-free RPMI-1640 media and stimulated with conditioned media for 10 minutes in a 37°C and 5% CO2 incubator. 10%FBS and serum-free RPMI-1640 media were used as control. Cells were then washed with cold PBS on ice and lysates were collected for western blot. The following experimental procedure can be found in western blot method section.

Growth Factor Assay: The procedure was the same as Conditioned Media Assay but growth factors were added directly into the cell culture with corresponding culture media. Growth factors used were listed: NRG1 (Cell Signaling Technology #5218) and EGF (Stemcell Technology #78006.1).

*Cell and Organoid Growth Assay*

*2D-cell growth:* CellTiter-Glo luminescent cell viability assay (Promega #G9243) was carried out in a 96-well plate format per manufacturer's instructions. The luminescent signal representing the relative number of cells was recorded as RLU (relative light units) according to the manufacturer's instructions. CellTiter-Glo 2.0 reagent was aliquoted into working solutions, stored at - 80°C and thawed to room temperature at each assay time point. Equal volume of reagent was added into each well of 96-well plates using a multichannel pipette. Plates were incubated in room temperature on an orbital shaker for 10 minutes to stabilize the reaction. Luminescence was read by GloMax 96 Microplate Luminometer. Cells were seeded in 100µl/well of media in triplicate per condition on day 0 and media was replaced every 3 days. The baseline level of luminescence that was measured on day 1 was subtracted from each corresponding plate at other time points to determine the relative cell growth (increase in luminescence signal). All growth assays were repeated in at least two independent biological replicates.

*3D-organoid growth:* Human and mouse organoids were trypsinized into a single-cell solution and counted. MSK-PCa2 (5000 cells), Trp53-KO (2000 cells), Rb1-KO (2000 cells) or PTENΔ/Δ -Rosa26-ERG (2000 cells) single organoids were seeded in 4x15ul Matrigel domes (Corning #356231) in a 48-well plate with 300ul organoid culture media and media was replenished every 3 days. After 6 days, the media was withdrawn and 100µl cell recovery solution (Corning #354253) was added. The organoid plate was then incubated at 4°C on a rotator for 60 minutes. Equal volume (100µl) of CellTiter-Glo reagents (Promega #G7571) was added into the organoid suspension, mixed and incubated in room temperature on an orbital shaker for 15 minutes to stabilize the reaction. A total of 200µl reaction volume was transferred to a 96-well plate for CellTiter-Glo assay.

*Xenograft Experiment*

For CWR22Pc, 22Pc-EP and VCaP xenograft experiments, 2 x 106 cells were mixed into a 50% Matrigel suspension (Corning #356237) and injected subcutaneously (100µl/injection) into flanks of castrated male C.B-17 SCID mice at age 6-8 weeks (Taconic). For co-injection experiments, 5 x 105 22Pc-EP-$^{eGFP}$ and 5x 105 22Pc-CAF-$^{tdTomato}$ cells were mixed and grafted into the mice of the same genetic background. For all xenograft experiments, 5 mice per group were grafted at both flanks (10 tumors per group). Tumor measurement began when tumors became palpable and were performed weekly using the tumor measuring system Peira TM900 (Peira bvba, Belgium). For drug treatment experiments, 20mg/kg neratinib (0.5% methylcellulose + 0.4% Tween80) was given by oral gavage 5 times a week. 20mg/kg AMG888 (PBS) was given by intraperitoneal injection twice a week. 25mg/mL YW538.24.71 (PBS) was given by intraperitoneal injection once a week. All animal experiments were approved by the Institutional Animal Care and Use Committee (IACUC) at Memorial Sloan Kettering Cancer Center.

*Clinical Specimen*

*General information:* Human tissue acquisition and usage were performed under approved IRB protocol numbers: 12-001, 12-245, and 90-040. Patient information was de-identified prior to any analysis. For prostate tissue microarray staining, archival formalin-fixed paraffin-embedded (FFPE) material was used under an IRB-approved protocol (15-331). For hormone naïve primary prostate adenocarcinoma tissues (20 patients in total), tumor tissue was obtained from radical prostatectomy specimens. The

Gleason scores ranged from 7 (3+4) to 9 (4+5). For neoadjuvant ADT treated primary prostate adenocarcinoma tissues (23 patients in total), tumor tissue was obtained from radical prostatectomy specimens after neoadjuvant ADT treatment. The Gleason scores ranged from 7 (3+4) to 10 (5+5). Please refer to detailed information in supplementary table 1. Each case was represented at least in duplicate (two cores per case) on the TMA. Most cases were represented in triplicate (three cores per case).

NRG1 Immunohistochemistry Analysis: NRG1 antibody (1:200, Cell Signaling Technology #2573) was used in human tissue immunohistochemistry. Human NRG1 immunohistochemistry was performed by the Department of Pathology at MSKCC using the anti-NRG1 antibody (Cell Signaling Technology #2573) at a 1:200 dilution, on a bond III automated immunostained (Leica Microsystems, IL, USA). Formalin-fixed paraffin-embedded (FFPE) tissue sections were de-paraffinized and endogenous peroxidase was inactivated. Antigen retrieval was performed using the Bond Epitope Retrieval Solution 1 (ER1) at 99-100°C for 60 minutes (Leica Microsystems). Sections were then incubated sequentially with the primary antibody overnight, post-primary for 15 minutes and polymer for 25 minutes, followed by a 10-minute colorimetric development with diaminobenzidine (DAB) (Bond Polymer Refine Detection; Leica Microsystems). FFPE material from CHL-1 human melanoma cell line xenografts with known levels of NRG1 was used as positive controls. FFPE materials from an SKBR3 human breast cancer cell line that do not express NRG1 were used as negative controls. IHC staining result was evaluated by a pathologist with experience in genitourinary pathology (A.G.). NRG1 expression was considered positive when there was cytoplasmic membranous or granular staining in the tumor or stromal cells. NRG1 staining intensity was scored following a three-tiered system (negative=0, weak=1, and strong=2). The immunohistochemistry detection of anti-human $\alpha$-SMA and vimentin antibody were performed at the Molecular Cytology Core Facility at Memorial Sloan Kettering Cancer

Center using Discovery XT processor (Ventana Medical Systems). Tissue microarrays were purchased from US Biomax (#PR243d and #PR481). The tissue sections were blocked first for 30 min in MOM Blocking reagent (Vector Labs; #: MKB-2213) in PBS. A mouse $\alpha$-SMA antibody (Sigma #A5228) was used in a 1 µg/mL concentration and incubated for 3 hours and followed by 30 minutes incubation with biotinylated anti-mouse secondary (M.O.M. Kit, Vector Labs, #BMK-2202), in 1:200 dilution. The Blocker D, Streptavidin- HRP and DAB detection kit (Ventana Medical Systems) was used according to the manufacturer's instructions. For vimentin; the tissue sections were blocked first for 30 min in mouse IgG Blocking Reagent (Vector Labs; #MKB-2213) in PBS. The primary antibody incubation (mouse vimentin anti-human antibody (Vector Lab #VP-V684, concentration 0.1µg/mL) was done for 3.5 hours and was followed by a 52-minute incubation of biotinylated mouse Secondary (M.O.M. Kit, Vector Labs, #BMK-2202), in 1:200 dilution. The Blocker D, Streptavidin-HRP and DAB detection kit (Ventana Medical Systems) were used according to the manufacturer's instructions.

*CRISPR-Cas9 Gene Targeting with Retroviral Transduction*

*CRISPR-Cas9:* Ten pairs of guides against the EGF-like domain of mouse NRG1 (exon2 or exon3) were designed using the guide design tool found here: (https://zlab.bio/guide-design-resources/) with the input of mouse Nrg1 EGF-like domain sequence :"AAGTGTGCGGAGAAGGAGAAAACTTTCTGTGTGAATGGAGGCGAGTGCTTCATGGTGAAGGACCTGTCAAACCCCTCAAGATACTTGTGCAAGTGCCCAAATGAGTTTACTGGTGATCGTTGCCAAAACTAC" After CRISPR-deletion efficiency validation, we chose 4 pairs for functional experiments. Guide sequences were cloned into the Lentiviral CRISPR/Cas9 vectors that were previously described (*29, 45*).

*Retroviral Transduction:* Lentiviral or retroviral transduction of cells for gRNA was performed as previously described (*29*). Cells were selected with 1µg/mL puromycin for

5 days or with 10μg/mL blasticidin for 5 days. To generate Nrg1-KO 22Pc-CAF, transduced cells were first selected with blasticidin for Cas9-expression and then sorted by flow cytometry to enrich for the mRFP-positive population carrying the gRNA against mouse Nrg1.

*Western Blot*

Cell lysates were collected using M-PER Mammalian Protein Extraction Reagent (Thermo Fisher Scientific # PI78501), in the presence of 1% protease inhibitor cocktail set (Calbiochem/EMD #539134) and 1% phosphatase inhibitor cocktail set (Millipore #524636). For tumor tissues, T-PER Tissue Protein Extraction Reagent (Thermo Fisher Scientific #78501) was used. Protein concentration was measured with Pierce™ BCA Protein Assay Kit (ThermoFisher #23225) following the manufacturer's instructions. Three volumes of proteins were mixed with 4x NuPAGE LDS Sample Buffer (Thermo Fisher Scientific #NP0008) and boiled at 95°C for 5 minutes. Boiled protein samples were stored at -80°C until usage. Proteins were run on pre-cast gels (Invitrogen). A full-range Rainbow protein marker was used (Fisher Scientific #RPN800E). Gels were run using 1x MOPS running buffer (Teknova #M1088) at 150 volts. Gels were transferred using a home-made 1x transfer buffer. Nitrocellulose membrane paper (Immobilon #IPVH00010) was used for transfer and was activated in 100% methanol (Fisher Scientific #A412-20). The transfer was performed at 4°C for 1.5 hours at 90 volts and the membrane was then blocked with 5% non-fat milk for 1 hour prior to the addition of primary antibody. The membrane was washed with 1X TBST (Teknova #T9511). Antibodies used were listed in detail in the Key Resources Table.

*Therapeutic Antibody*

YW538.24.71 was acquired from Genentech through an MTA request (ID #OR-216518). AMG888 (*89*) was kindly provided by Dr. Sarat Chandarlapaty at Memorial Sloan Kettering Cancer Center.

### *Column Purification of Conditioned Media*

50x conditioned media from 22Pc-CAF was collected as described above. Total 5ml (50x) conditioned media was first diluted into 20ml with buffer A (20mM Hepes, pH 7.5, 15mM NaCl) as Input and injected into HiTrap Q HP anion exchange chromatography column (GE Healthcare #17115401). 500µl of Input was saved for future analysis. During sample loading, 5ml of flow-through (FT) was collected and saved for further analysis. After samples were loaded on the column, the first elution was performed with 5% of buffer B (20mM Hepes, pH 7.5, 1M NaCl) for 5ml to remove weakly bound proteins. A second elution was performed with 5ml of 30% Buffer B. 500ul of Q30 was saved for future analysis. Concurrently, sample collection was initiated with 1ml per fraction. Then the third elution was performed with 5ml of 100% buffer B (Q100), with 1ml/fraction. 500ul of Q100 was saved for future analysis. A total of 4.5ml from fractions Q30 was pooled, dialyzed against Buffer A, and re-injected into a second HiTrap Q HP anion exchange column. Gradient elution from 10% to 45% buffer B was applied and 18 fractions were collected with 1ml / fraction. Then the final elution was applied with 100% buffer B and 4 fractions were collected with 1ml/fraction. All fractions were used immediately for assays, or stored short-term at 4°C and used within 1 week. For protein analysis, a 4x loading buffer was added into each fraction and samples were boiled at 95°C for 5 minutes.

### *Gene Expression Analysis by qRT-PCR*

Total RNA from live cells or frozen tissue was extracted using PureLink™ RNA Mini Kit (Thermo Fisher Scientific #12183025) following the manufacturer's instructions. RNA was diluted into 200ng/µL with DEPC-treated water (Thermo Fisher Scientific #AM9916). Reverse transcription was performed using the high capacity cDNA Reverse Transcriptase Kit (Fisher Scientific, #4368813), following the manufacturer's instructions. The real-time quantitative qRT-PCR analysis was performed using the QuantiFast SYBR Green PCR Kit (QIAGEN #204057) and with QuantStudio 6 Flex Real-Time PCR System. Gene expression was normalized to *ACTB* or *GAPDH*. RT2 qRT-PCR Primer Assays and QuantiTect Primer Assays from QIAGEN were used to perform all gene expression analysis. Individual primers are listed in the Key Resource Table. To distinguish mouse or human gene expression from xenograft tissue, we designed human-specific qRT-PCR primers for *ACTB*: Forward-5'-CACCAACTGGGACGACAT, Reverse-5'-ACAGCCTGGATAGCAACG and used mouse-specific qRT-PCR primers for *actb* (QIAGEN #PPM02945B-200). All gene expression assays were repeated in at least two independent biological replicates.

*RNA-Seq*

*<u>Sample and Library Preparation for RNA-seq:</u>* 1x$10^6$ 22Pc-EP cells were plated in a 6-well plate, growing in regular RPMI-1640 containing 10% FBS. Enzalutamide (500nM) or recombinant NRG1 peptide (10ng/mL) was added the next day. After 48 hours, cells were trypsinized and collected by spinning at 500 g for 1.5 min at 4°C. Cells were then washed once with cold 1X PBS and spun down at 500 g for 1.5 min at 4°C. After discarding the supernatant, cells were lysed using 50 mL cold lysis buffer (10 mM Tris-HCl pH 7.4, 10 mM NaCl, 3 mM MgCl2, 0.1% IGEPAL CA-360) and spun down immediately at 500 g for 10 min, 4°C. RNA was extracted using PureLink™ RNA Mini Kit (Thermo Fisher Scientific #12183025) following the manufacturer's instructions. RNA

was diluted into 200ng/µL with DEPC-treated water (Thermo Fisher Scientific #AM9916). RNA-Seq libraries were prepared using the Illumina TruSeq stranded mRNA kit, with 10 cycles of PCR amplification, starting from 500 ng of total RNA, at the Genome Technology Center (GTC) at New York University Langone Medical Center. Barcoded RNA-Seq was run as paired-end read 50 nucleotides in length on the Illumina NovaSeq 6000 and Poly-A selection was performed.

*Raw Data Processing and Quantification:* For each read, the first 6 and the last nucleotides were trimmed to the point where the Phred score of an examined base fell below 20 using in-house scripts. If, after trimming, the read was shorter than 45 bp, the whole read was discarded. Trimmed reads were mapped to the human reference genome (hg38) with HISAT2 v2.1.0 indicating that reads correspond to the reverse complement of the transcripts**.** Alignments with a quality score below 20 were excluded from further analysis. Gene counts were produced with StringTie v1.3.3b and the Python script “prepDE.py” provided in the package. StringTie was limited to reads matching the reference annotation GENCODE v27. After obtaining the matrix of reading counts, differential expression analysis was conducted, and normalized counts were produced using DESeq2. P-values were adjusted for multiple testing using the Benjamini-Hochberg procedure.

*AR Signature:* A list of Enz suppressed genes in 22PC-EP was used to construct an AR signature gene list (DMSO versus Enz condition, log2 fold change>2 or <-2, adjusted p-value < 0.05). Top 24 ranking genes were selected. GP2 (ranking=25th, log2 fold change=1.996, adjusted p value=3.71x10-5) and FKBP5 (ranking=26th, log2 fold change=1.972, adjusted p value=$2.31x10^{-51}$) adjusted p value=$2.31x10^{-51}$) were also included in this AR signature gene list. The final AR signature consists of 26 genes. AR output score was calculated by the quantification of the composite expression of this 26-

gene signature in each condition following method in TCGA (*21*) AR score with two other AR signature gene lists was calculated similarly (*42, 90*).

GO Term Enrichment Analysis: Gene Ontology Enrichment Pathway analysis was performed using PANTHER to determine molecular and biological functional categories that were enriched in both AR and NRG1 co-activated genes. The input gene lists were generated from the overlapping of differentially up-regulated genes in two comparisons based on adjusted p value<0.05 (FBS+Enz compared to FBS+DMSO, FBS+NRG1 compared to FBS+DMSO) which consists of 303 genes in total. 303 genes were further filtered by log2 Fold Change>0.5. Cutoff values of FDR<0.05 were used to select top enriched pathways.

*Gene Set Enrichment Analysis (GSEA):* GSEA statistical analysis was carried out with publicly available software from the Broad Institute (http://www.broadinstitute.org/gsea/index.jsp). Weighted GSEA enrichment statistic and Signal2Noise metric for ranking genes were used. RNA-seq data have been deposited in the Sequence Read Archive (SRA) with the accession numbers GSE147976.

### *Stroma Gene Signature and Pathway Enrichment Analysis in Patients*

Analysis in primary prostate cancer patient cohort was performed in cBioportal.org and Python environment using The Cancer Genome Altas (TCGA) database (Cancer Genome Atlas Research, 2015) database (Cancer Genome Atlas Research, 2015; Cerami et al., 2012; Gao et al., 2013). Reactive prostate stroma signature gene list was obtained from Dakhova et al., and was used to calculate a reactive stromal signature score(*91*). High-grade prostate tumor-associated stroma gene list was obtained from Tyekucheva et al., and was used to calculate high-grade tumor stroma signature score(*2*). All tumor-stroma signature score was calculated using the same method as in Tyekucheva et al.,(*2*). Specifically, we used the ssGSEA algorithm to assign an enrichment score of genes in each gene list above for each sample. We compared the ssGSEA score of high-grade tumor stroma signature and reactive stroma signature in patients stratified by histology (tumor vs normal) and Gleason score (low (<7) vs high (>=7)). Higher ssGSEA scores correspond to more joint upregulation of genes in each signature. Gene signatures were subsetted to the genes measured in the TCGA dataset. Differential gene expression analysis was first performed between patients with high reactive stroma scores and low reactive stroma scores. (p value<0.05) GO-term pathway enrichment analysis was then performed with the list of differentially expressed genes. (p value< 0.05, FDR<0.25). Gene set enrichment analysis was performed with GSEA version 4.0.0 from the Broad Institute at MIT. Tumor purity was calculated using the ABSOLUTE method(*92*).

*Time on Drug Treatment Analysis with NRG1 Signature*

Processed 444 SU2C metastatic prostate cancer patient cohort (*30*). RNA-seq data and enzalutamide/abiraterone treatment data were downloaded from cBioPortal (http://www.cbioportal.org/). 128 patients of this cohort with metastatic CRPC have baseline biopsy and matched clinical data. 75 patients of this 128 sub-cohort have gene expression data captured by poly-A RNA-seq. 56 patients of these 75 sub-cohort have records of time on treatment with either enzalutamide or abiraterone. NRG1 signature gene list was obtained from Nagashima et al., and calculated using the Single Sample Gene Set Enrichment Analysis (ssGSEA) method(*93*). Histogram of NRG1 signature score distribution was generated with the Seaborn package in Python. The probability of treatment duration figure was generated using the Kaplan Meier method and Log-Rank test implemented in the Lifelines package in Python. Pearson correlation analysis was conducted between time on first-ARSI (androgen receptor signaling inhibitor) and NRG1 signature score ($p = 0.005$). Cox Hazard Ratio analysis was performed by R Studio (Version 1.1.453).

### *Quantification and Statistical Analysis*

GraphPad Prism 8.0 was used for statistical calculations. For all comparisons between two groups of independent datasets, multiple t-tests were performed, p-value and standard error of the mean (SEM) were reported. For all comparisons among more than two groups (>2), one-way or two-way ANOVA was performed, p values and SEM were reported; and p values were adjusted by multiple testing corrections (Bonferroni) when applicable. Results from all in vitro assays are representatives of at least two independent biological repeats. In all figures, not significant (n.s), $p < 0.05$ (*), $p < 0.01$ (**), $p < 0.001$ (***) and $p < 0.0001$ (****). The usage of all statistical approaches was examined by our bioinformatics collaborators. All bioinformatics analyses and comparisons are described in detail below.

# CHAPTER 1

## *1.1 Introduction*

In prostate cancer, the reactive stroma is characterized by expression of tenascin and fibroblast activating protein (FAP), with extensive matrix remodeling as evidenced by collagen deposition. A major component of the reactive prostate stroma is the myofibroblast, defined as α-SMA/vimentin double-positive cells (*94, 95*). Despite distinct molecular and histological features of reactive prostate stroma, their role in mediating resistance to AR-targeted therapy is not well studied. Here we first characterized reactive stroma activity in prostate cancer patients in TCGA and found reactive stroma activity is significantly higher in cancer versus normal prostate gland and is associated with more advanced disease. Results from pathway enrichment analysis suggest reactive stroma may be functionally different from the normal prostate stroma.

## *1.2 Reactive stroma in prostate cancer*

Using a prostate-specific reactive stroma gene signature (*91*), we first examined the prostate cancer TCGA dataset for associations with cancer and with tumor grade. The reactive stroma score was significantly higher in tumor samples compared to the normal prostate gland ($p = 2 \times 10^{-6}$) (Figure 1A) and also in higher grade tumors ($p = 2 \times 10^{-4}$) based on Gleason score (Figure 1B). This association was confirmed using a second signature enriched for genes expressed in high-grade tumor-associated stroma (*2*) ($p = 3 \times 10^{-6}$) (Figure 1C). We further validated the association of reactive stroma with primary prostate cancer using immunohistochemical staining for $\alpha$-SMA and vimentin in an independent cohort from MSK (Figure 1D-H). Notably, PI3K-AKT-mTOR and RTK signaling were among the top pathways enriched in high-stroma score patients based on gene set enrichment analysis (GSEA) of the TCGA dataset (Figure 1I).

### *1.3 Model tumor-stroma interaction using a CWR22Pc model*

To follow up on these clinical associations, we modeled tumor-stroma interaction using the patient-derived xenograft model CWR22Pc which is initially castration-sensitive but can progress to castration-resistance (*1*). We found that a cell line derived from this model has a population of murine fibroblasts. To obtain a pure epithelial population, we used flow cytometry with species-specific antibodies against surface antigens to individually purify human cancer (epithelial) cells from the mouse fibroblasts, which we named CWR22Pc-EP hereafter called 22Pc-EP (*29*) and CWR22Pc-CAF (22Pc-CAF), respectively (Figure 2A,B). Interestingly, when 22Pc-EP cells were isolated from 22Pc-CAF, acquisition of bicalutamide (Bic) resistance was substantially delayed compared to the mixed epithelial/fibroblast parental CWR22Pc population (152 versus 48 days) and enzalutamide (Enz) resistance was never observed (Figure 3A,B). Based on this observation, we hypothesized that CAFs may contribute to the acquisition of an antiandrogen resistant state.

We next developed a co-culture assay to model CAF/cancer cell interactions in vitro and in vivo. We labeled 22Pc-EP with eGFP and 22Pc-CAF with tdTomato using viral transduction (Figure 3H). 22Pc-EPe$^{\mathrm{GFP}}$ cells were cultured either with or without 22Pc-CAF$^{\mathrm{tdTomato}}$ cells in the presence of vehicle, Bic, or Enz and eGFP fluorescence intensity was measured to quantify the relative 22Pc-EP cell number (Figure 3C). We observed significantly more 22Pc-EP$^{\mathrm{eGFP}}$ cells in the co-culture condition following antiandrogen treatment but no difference with vehicle treatment (Figure 3D-F). Thus, the CAFs confer a pro-growth/survival signal to 22Pc-EP cells only in the setting of AR blockade. We then evaluated whether 22Pc-CAF also promotes castration-resistance in vivo. To this end, we first grafted parental CWR22Pc (with CAFs) or 22Pc-EP (without CAFs) into castrated male mice to mimic the clinical scenario of chronic androgen deprivation therapy (ADT) and found that parental CWR22Pc tumors grew significantly faster than 22Pc-EP (Figure 3G). To further test the contribution of CAFs to castration-resistance, 22Pc-EP$^{eGFP}$ cells were grafted into castrated mice with or without 22Pc-CAF$^{tdTomato}$ cells. Like the CAF-containing parental CWR22Pc, 22Pc-EP tumors grew significantly faster when co-injected with CAFs (Figure 3I). Analysis of tumors from the co-injection group by immunofluorescence (of eGFP or tdTomato) revealed infiltration of 22Pc-CAF in the tumor mass, suggestive of interactions between CAFs and adjacent tumor cells in vivo (Figure 3J). Taken together, these data establish that 22Pc-CAF can promote antiandrogen and castration-resistance of 22Pc-EP.

### *1.4 CAF-secreted factors promote antiandrogen resistance*

We posited that the growth-promoting effects of CAFs on cancer cell growth during antiandrogen treatment could be occurring through two possible mechanisms: fibroblast-epithelial cell-to-cell contact or secretion of CAF-derived soluble factors. To test the latter hypothesis, we collected conditioned media from either 22Pc-CAF (22Pc-CAF$^{CM}$) or 22Pc-EP (22Pc-EP$^{CM}$) and tested their ability to stimulate the growth of 22Pc-EP cells treated with androgen deprivation (modeled by the use of 5% charcoal-dextran stripped FBS, hereafter CSS) or antiandrogens (Bic or Enz). 22Pc-CAF$^{CM}$ promoted resistance of 22Pc-EP to CSS and antiandrogens, while 22Pc-EP$^{CM}$ or serum-free media (negative control) did not (Figure 4A,B), indicating that one or more soluble factor(s) secreted by CAFs was responsible for growth. Furthermore, concentrating the 22Pc-CAF$^{CM}$ by 2-4 folds increased the resistance promoting activity, suggesting a dose-dependent effect (Figure 5A). Exposure of 22Pc-CAF$^{CM}$ to either heat (95°) or proteinase K abolished the ability of 22Pc-CAF$^{CM}$ to rescue the growth phenotypes (Figure 4C,D and Figure 5B), suggesting that the soluble factors responsible for the promotion of resistance were proteins. 22Pc-CAF$^{CM}$ also promoted resistance to CSS and Enz in two additional androgen-dependent human prostate models, the VCaP cell line and the patient-derived cancer organoid MSK-PCa2 (Figure 4I-L).

AR signaling is critical for prostate oncogenesis, and AR pathway reactivation in advanced PCa is one of the primary mechanisms of acquired resistance to AR targeted therapies (*7*). Therefore, we next asked if secreted protein factors from 22Pc-CAF reactivate AR signaling in 22Pc-EP even in the presence of Enz. We observed sustained growth of 22Pc-EP cells in CSS or in Enz in the presence of 22Pc-CAF$^{CM}$ (Figure 2E,F). Notably, several canonical AR target genes remained suppressed despite abundant AR mRNA expression (Figure 4G,H and Figure 6C). Collectively, these results suggest that secreted protein factors from 22Pc-CAF promote antiandrogen resistance in 22Pc-EP through a mechanism that does not immediately result in AR reactivation.

### *1.5 Summary*

Using the CWR22Pc system to model tumor-stroma interaction in vitro and in vivo, we found 22Pc-CAF promotes antiandrogen and castration resistance through secretion of unknown protein factors. This finding was subsequently validated in additional cell lines and organoid models. We will move forward in the next chapter to identify such resistance-promoting protein factors from 22Pc-CAF.

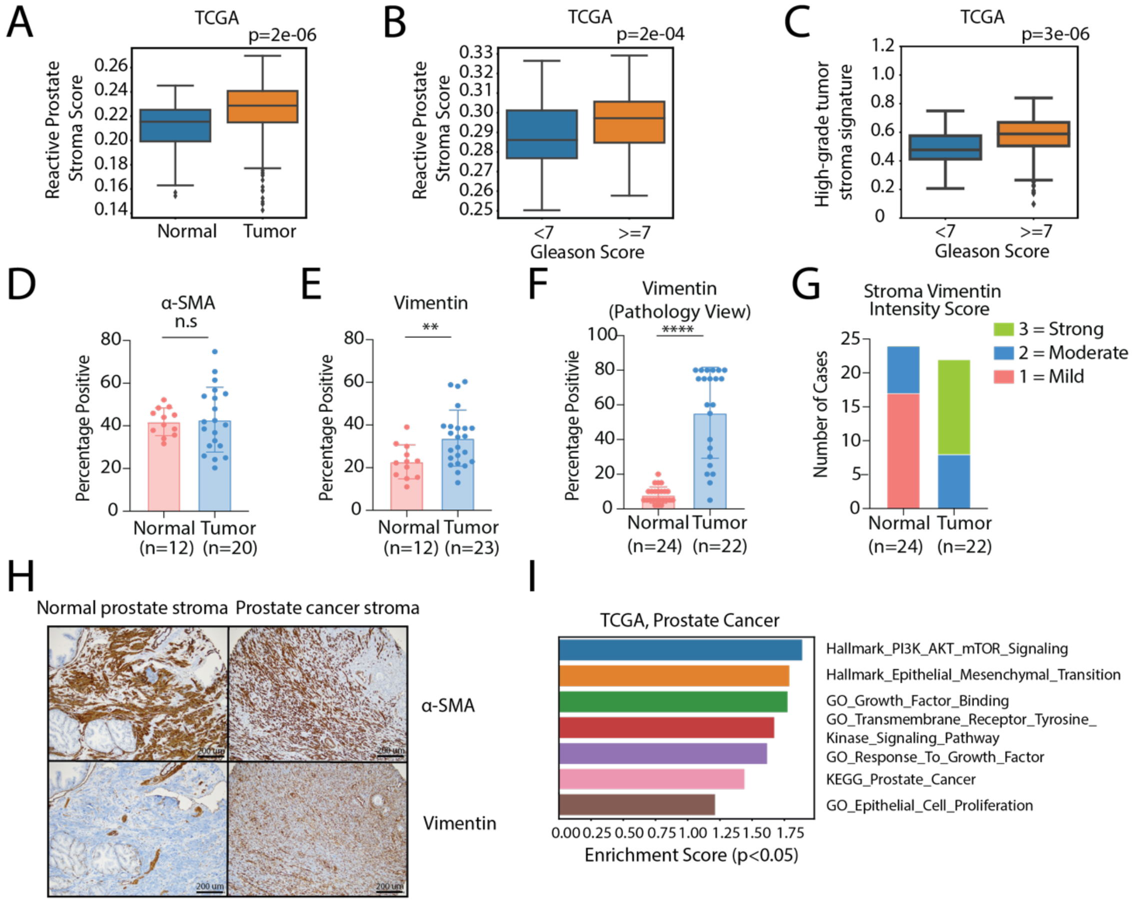

**Figure 1. Reactive stroma in localized prostate cancer is associated with higher tumor grade and PI3K-AKT pathway activation.**

(A) Comparison of reactive prostate stroma score between normal prostate tissue and primary prostate cancer tissue in TCGA cohort, p value=$2x10^{-6}$. See details in methods. (B) Comparison of reactive prostate stroma score between tumors with Gleason score <7 and those >=7, p value=$2x10^{-4}$. See details in methods. (C) Comparison of high-grade tumor associated stroma signature score between tumors with Gleason score <7 and those >=7 , p value=$3x10^{-6}$. See details in methods. (D-E) Quantification of immunohistochemistry analysis of α-SMA (D) or vimentin (E) in the prostate tissue array using ImageJ IHC profiler plugin (**p<0.01, Student's t-test, error bar presents±SD). (F) Quantification of stroma-specific vimentin intensity in the prostate cancer tissue microarray. ****p<0.0001, Student's t-test, error bar presents±SD. (G) Histogram showing distribution of vimentin intensity case numbers in the prostate cancer tissue microarray (1=mild, 2=moderate and 3=strong). (H) Immunohistochemistry analysis of α-SMA and vimentin in normal prostate gland and prostate cancer specimens in the prostate cancer tissue microarray. (I) Pathway enrichment analysis showing top-ranking enriched pathways between tumors with high reactive stroma activity versus those with low reactive stroma activity in TCGA cohort (p value<0.05, FDR<0.25).

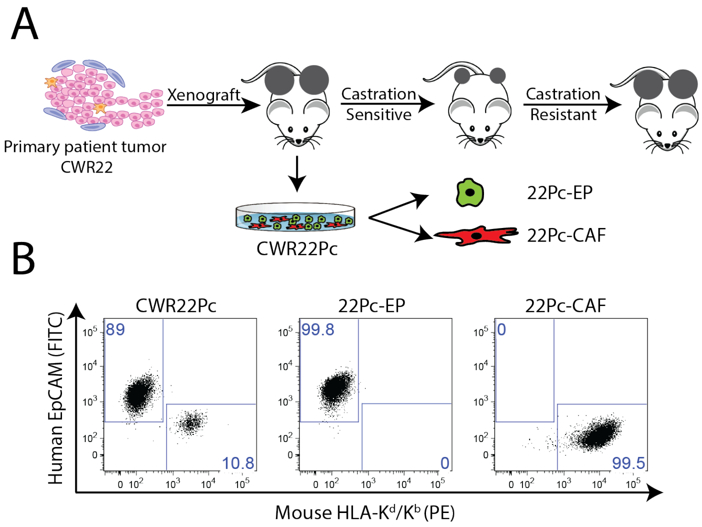

**Figure 2. Development of an androgen-dependent CWR22Pc system to model tumor-stroma interaction.**

(A) Schematic diagram depicting the origin and characteristics of the CWR22Pc model(*1*). CWR22Pc contains both murine cancer -associated fibroblasts (22Pc-CAF) and human cancer cells (22Pc-EP), as previously described. (B) Isolation of 22Pc-EP and 22Pc-CAF by FACS using human-specific EpCAM and mouse-specific H-2K$^b$/H-2D$^b$ MHC class I surface marker staining.

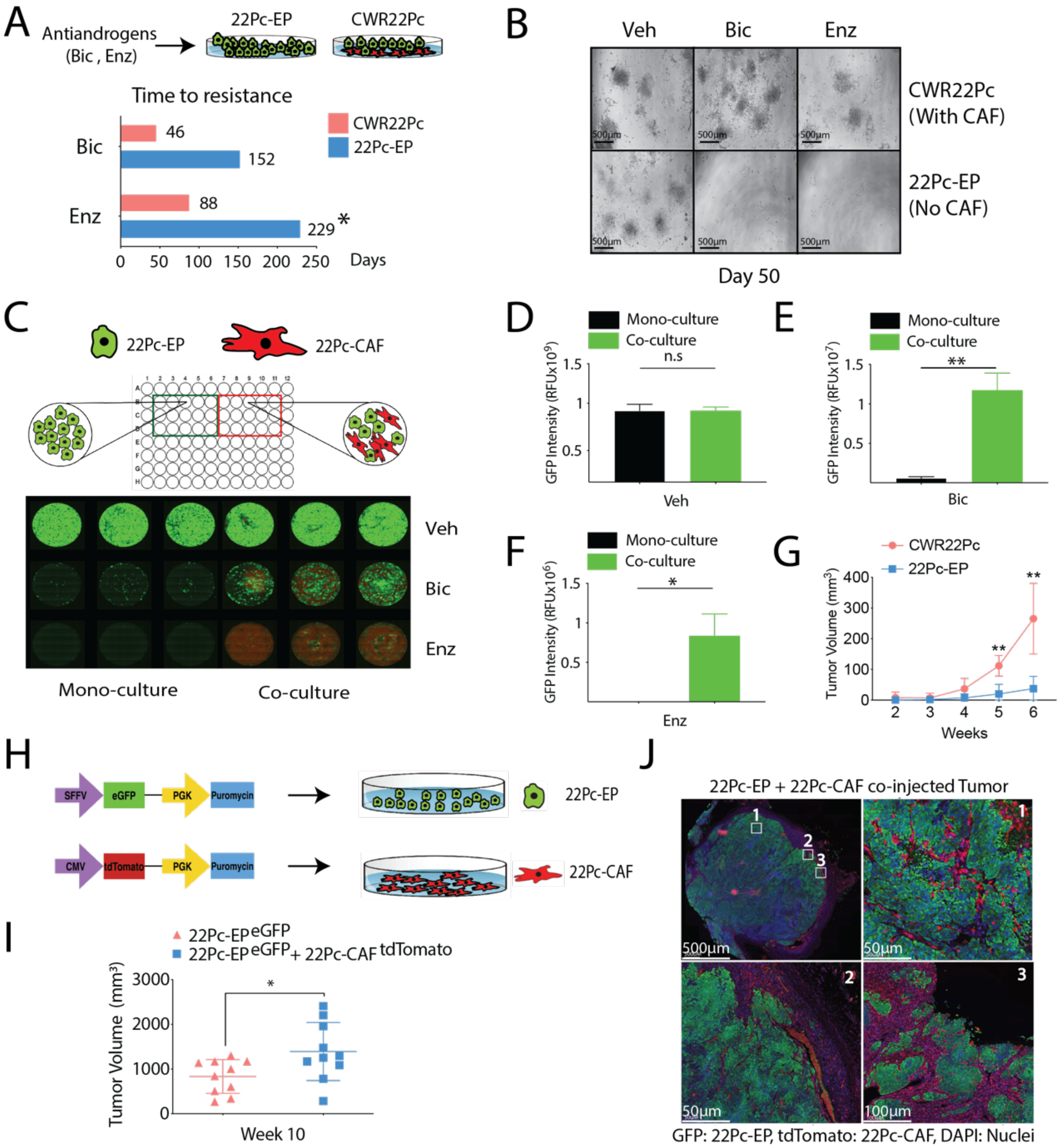
A
Antiandrogens
(Bic , Enz)
22Pc-EP
CWR22Pc
Time to resistance
Bic
Enz
46
152
88
229
*
0
50
100
150
200
250
Days
CWR22Pc
22Pc-EP
B
Veh
Bic
Enz
CWR22Pc
(With CAF)
22Pc-EP
(No CAF)
500μm
Day 50
C
22Pc-EP
22Pc-CAF
Veh
Bic
Enz
Mono-culture
Co-culture
D
Mono-culture
Co-culture
n.s
GFP Intensity (RFUx10⁹)
1.5
1
0.5
Veh
E
Mono-culture
Co-culture
**
GFP Intensity (RFUx10⁷)
1.5
1
0.5
Bic
F
Mono-culture
Co-culture
*
GFP Intensity (RFUx10⁶)
1.5
1
0.5
Enz
G
CWR22Pc
22Pc-EP
Tumor Volume (mm³)
400
300
200
100
0
**
**
2
3
4
5
6
Weeks
H
SFFV
eGFP
PGK
Puromycin
22Pc-EP
CMV
tdTomato
PGK
Puromycin
22Pc-CAF
I
22Pc-EP eGFP
22Pc-EP eGFP + 22Pc-CAF tdTomato
*
Tumor Volume (mm³)
3000
2000
1000
0
Week 10
J
22Pc-EP + 22Pc-CAF co-injected Tumor
1
2
3
500μm
50μm
50μm
100μm
GFP: 22Pc-EP, tdTomato: 22Pc-CAF, DAPI: Nuclei

Figure 3

**Figure 3. Cancer-associated fibroblasts (CAF) promote antiandrogen resistance in CWR22Pc.**

(A) Bar graph showing time to development of resistance to Bic (10μM) or Enz (1μM) in CWR22Pc and 22Pc-EP. Asterisk (*) denotes that 22Pc-EP remain growth arrested on day 229 in Enz. (B) Representative images showing results of colony formation assay of CWR22Pc and 22Pc-EP cells treated with Veh (DMSO), Bic (10μM) or Enz (0.1μM) on day 50. (C) Top: Cartoon showing 22Pc-EP$^{eGFP}$ + 22Pc-CAF$^{tdTomato}$ co-culture or 22Pc-EP$^{eGFP}$ mono-culture. Bottom: Fluorescent images of co-culture assay showing number of 22Pc-EP$^{eGFP}$ cells (green) and 22Pc-CAF$^{tdTomato}$ cells (red) in the presence of Bic (10μM), Enz (1μM) or Vehicle (Veh, DMSO) on day 30 (triplicates). (D-F) Quantification of eGFP fluorescence signal intensity using relative fluorescence unit (RFU) in three experimental conditions (Veh, Bic or Enz) shown in C (**p<0.01, *p<0.05, n.s: not significant. Student's t-test, error bar represents ±SD). (G) Growth of CWR22Pc or 22Pc-EP tumor xenografts in castrated mice (n=5 mice per group, **p<0.01, multiple t-test, error bar represents ±SEM). (H) Schematic of the generation of 22c-EP$^{eGFP}$ and 22Pc-CAF$^{tdTomato}$ by viral transduction. (I) Tumor volumes of 22Pc-EP$^{eGFP}$ or co-injected 22c-EP$^{eGFP}$ + 22Pc-CAF$^{tdTomato}$ xenografts at week 10 (n=5 mice per group, *p<0.05, Student's t-test, error bar presents ±SEM). (J) Immunofluorescence analysis of tumor infiltrating 22Pc-CAF$^{tdTomato}$ cells in 22c-EP$^{eGFP}$ + 22Pc-CAF$^{tdTomato}$ co-injected xenografts at week 10 (Green: 22c-EP$^{eGFP}$, Red: 22Pc-CAF$^{tdTomato}$).

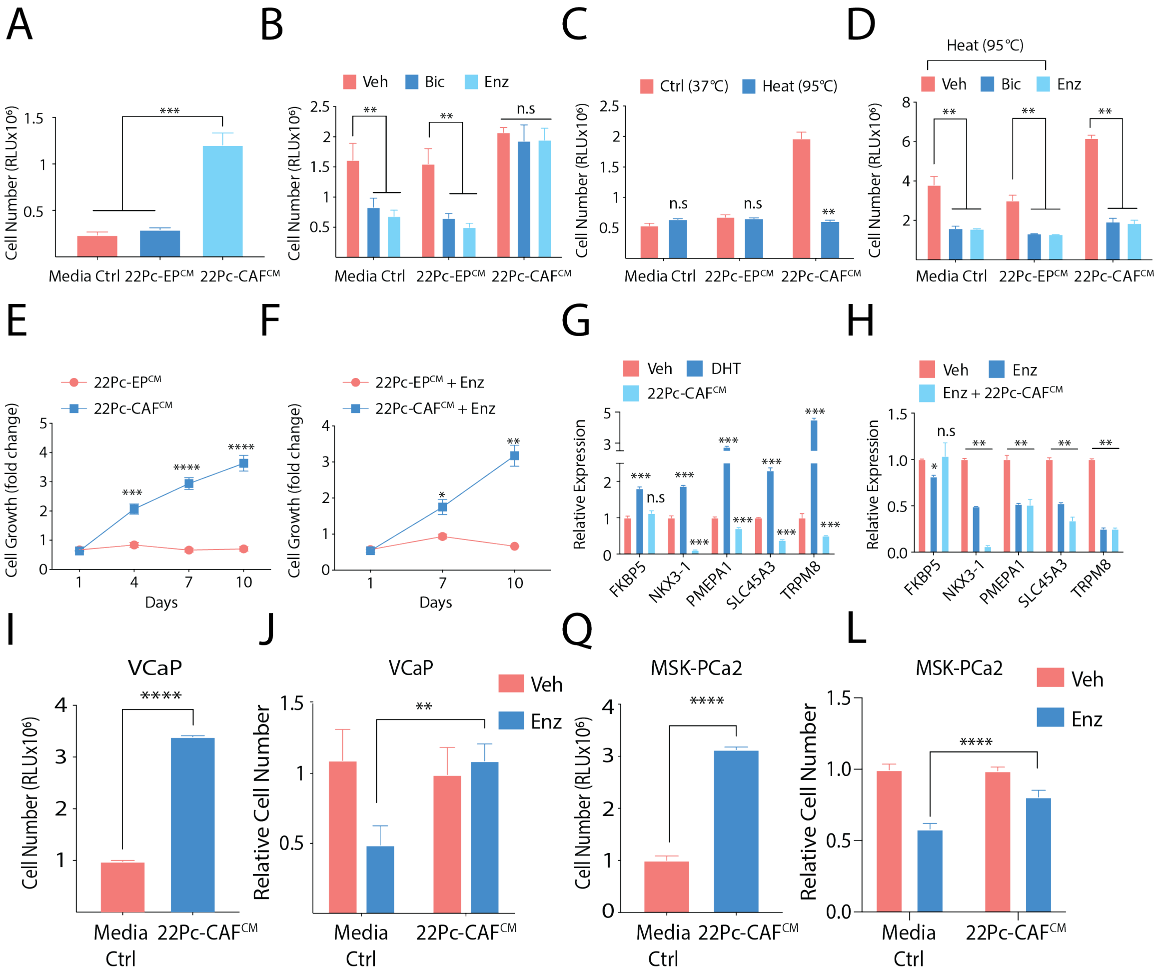
A
Cell Number (RLUx10⁶)
1.5
1
0.5
***
Media Ctrl
22Pc-EPCM
22Pc-CAFCM
B
Veh
Bic
Enz
Cell Number (RLUx10⁶)
2.5
2
1.5
1
0.5
**
**
n.s
Media Ctrl
22Pc-EPCM
22Pc-CAFCM
C
Ctrl (37℃)
Heat (95℃)
Cell Number (RLUx10⁶)
2.5
2
1.5
1
0.5
n.s
n.s
**
Media Ctrl
22Pc-EPCM
22Pc-CAFCM
D
Heat (95℃)
Veh
Bic
Enz
Cell Number (RLUx10⁶)
8
6
4
2
**
**
**
Media Ctrl
22Pc-EPCM
22Pc-CAFCM
E
22Pc-EPCM
22Pc-CAFCM
Cell Growth (fold change)
5
4
3
2
1
0
***
****
****
1
4
7
10
Days
F
22Pc-EPCM + Enz
22Pc-CAFCM + Enz
Cell Growth (fold change)
4
3
2
1
0
*
**
1
7
10
Days
G
Veh
DHT
22Pc-CAFCM
Relative Expression
5
3
2
1
0
***
n.s
***
***
***
***
***
***
***
***
FKBP5
NKX3-1
PMEPA1
SLC45A3
TRPM8
H
Veh
Enz
Enz + 22Pc-CAFCM
Relative Expression
1.5
1.0
0.5
0.0
n.s
*
**
**
**
**
FKBP5
NKX3-1
PMEPA1
SLC45A3
TRPM8
I
VCaP
Cell Number (RLUx10⁶)
4
3
2
1
****
Media Ctrl
22Pc-CAFCM
J
VCaP
Veh
Enz
Relative Cell Number
1.5
1
0.5
**
Media Ctrl
22Pc-CAFCM
Q
MSK-PCa2
Cell Number (RLUx10⁶)
4
3
2
1
0
****
Media Ctrl
22Pc-CAFCM
L
MSK-PCa2
Veh
Enz
Relative Cell Number
1.5
1.0
0.5
0.0
****
Media Ctrl
22Pc-CAFCM

Figure 4

**Figure 4. CAF-secreted factors promote antiandrogen resistance in multiple models.**

(A) Growth of 22Pc-EP cells in CSS media supplemented with either conditioned media from 22Pc-EP (hereafter, 22Pc-EP$^{CM}$) or from 22Pc-CAF (hereafter, 22Pc-CAF$^{CM}$). CellTiter-Glo reading on day 4. Media Ctrl: serum free media. (B) Growth of 22Pc-EP cells in FBS media supplemented with either 22Pc-EP$^{CM}$ or 22Pc-CAF$^{CM}$ treated with Veh (DMSO), Bic (10μM) or Enz (0.1μM). CellTiter-Glo reading on day 7. Media Ctrl: serum free media. (C) Growth of 22Pc-EP cells in CSS media supplemented with either heat-inactivated 22Pc-EP$^{CM}$ or 22Pc-CAF$^{CM}$. CellTiter-Glo reading on day 4. Media Ctrl: serum free media. (D) Growth of 22Pc-EP cells in FBS media supplemented with heat-inactivated 22Pc-EP$^{CM}$ or 22Pc-CAF$^{CM}$ treated with Veh (DMSO), Bic (10μM) or Enz (0.1μM). CellTiter-Glo reading on day 7. Media Ctrl: serum free media. (E) Growth curve of 22Pc-EP cells in CSS media supplemented with 22Pc-EP$^{CM}$ or 22Pc-CAF$^{CM}$. CellTiter-Glo reading on day 1, 4, 7 and 10. (F) Growth curve of 22Pc-EP cells in FBS media supplemented with 22Pc-EP$^{CM}$ or 22Pc-CAF$^{CM}$ treated with Enz (0.1μM). CellTiter-Glo reading on day 1, 7 and 10. (G) qRT-PCR analysis of AR target genes in 22Pc-EP cells in CSS media treated with Veh (DMSO), DHT (1nM) or 22Pc-CAF$^{CM}$ for 24 h (normalized to *ACTB*). (H) qRT-PCR analysis of AR target genes in 22Pc-EP cells in FBS media treated with Veh (DMSO), Enz (0.1μM) or Enz + 22Pc-CAF$^{CM}$ for 24 h (normalized to *ACTB*). (I) Growth of VCaP cells in CSS media supplemented with 22Pc-CAF$^{CM}$. CellTiter-Glo reading on day 4. Media Ctrl: serum free media. (J) Growth of VCaP cells in Enz (1μM) or Veh (DMSO) containing FBS media supplemented with 22Pc-CAF$^{CM}$. CellTiter-Glo reading on day 7. Media Ctrl: serum free media. (K) Growth of patient-derived cancer organoid MSK-PCa2 in DHT-depleted organoid media supplemented with 22Pc-CAF$^{CM}$. CellTiter-Glo reading on day 4. Media Ctrl: EGF-deficient organoid media. (L) Growth of patient-derived cancer organoid MSK-PCa2 in Enz (1μM) or Veh (DMSO) containing human organoid media supplemented with 22Pc-CAF$^{CM}$. CellTiter-Glo reading on day 7. Media Ctrl: EGF-deficient organoid media. (****$p<0.0001$, ***$p<0.001$, **$p<0.01$, *$p<0.05$, n.s: not significant, Student's t-test, error bar represents ±SD)

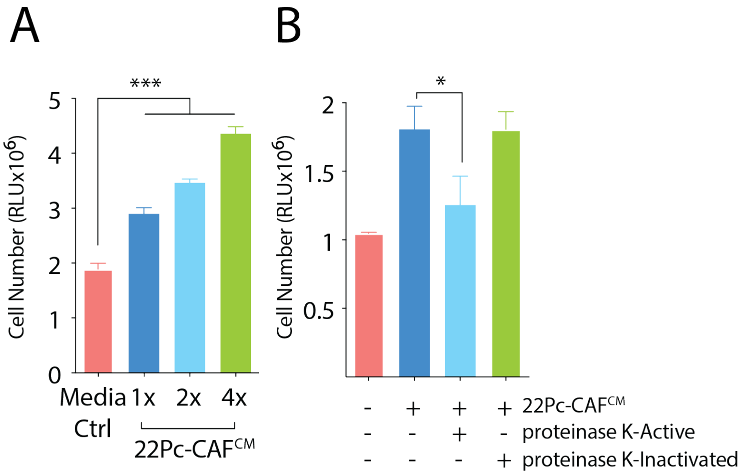

**Figure 5. Resistance-promoting factors from CAF are likely to be protein.**
(A) Growth of 22Pc-EP cells in CSS media supplemented with increasing concentration of 22Pc-CAF$^{CM}$ (1x, 2x and 4x). CellTiter-Glo reading on day 4. Media Ctrl: serum free media. (B) Growth of 22Pc-EP cells in CSS media supplemented with 22Pc-CAF$^{CM}$ treated with proteinase K (200µg/mL) or heat-inactivated proteinase K. CellTiter-Glo reading on day 4. Media Ctrl: serum free media. (***$p<0.001$, *$p<0.05$,, Student's t-test, error bar represents ±SD)

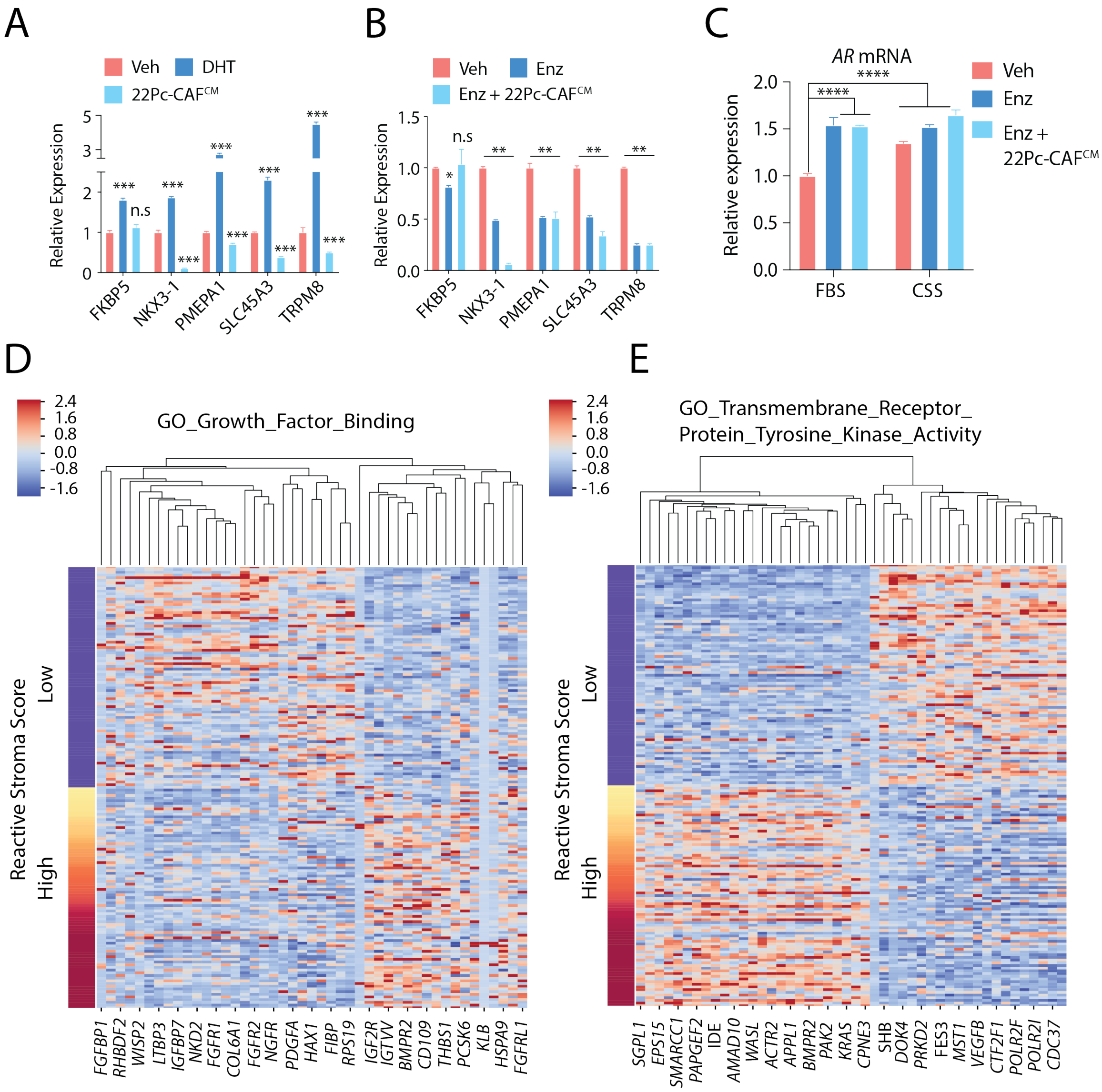

**Figure 6. Canonical AR targets are not re-activated by CAF-secreted factors.** (A) qRT-PCR analysis of AR target genes in 22Pc-EP cells in CSS media treated with Veh (DMSO), DHT (1nM) or 22Pc-CAF$^{CM}$ for 24 hr (normalized to *ACTB*). (B) qRT-PCR analysis of AR target genes in 22Pc-EP cells in FBS media treated with Veh (DMSO), Enz (0.1µM) or Enz + 22Pc-CAF$^{CM}$ for 24 hr (normalized to *ACTB*). (D) Heatmap showing unsupervised clustering with Growth Factor Binding gene signature between tumors with high reactive stroma score and tumors with low score (TCGA). (E) Heatmap showing unsupervised clustering using Transmembrane Receptor Protein Tyrosine Kinase Activity signature between tumors with high reactive stroma score and tumors with low score (TCGA). See details in methods.

# CHAPTER 2

## *2.1 Introduction*

Cell-cell interactions usually occur by direct contact or through secreted factors (paracrine or endocrine mechanisms). In the co-culture assay, we observed that survived GFP-positive 22Pc-EP tumor cells are not necessarily spatially adjacent to 22Pc-CAFs. Therefore, we reasoned 22Pc-CAF may promote antiandrogen resistance in 22Pc-EP through secreted factor(s) and we subsequently validated this hypothesis through the conditioned media assay. Next, we seek to identify the potential protein factor(s) from 22Pc-CAF. We also reasoned that by simply profiling the transcriptome of 22Pc-CAF, we may not be able to identify the resistance-promoting factor(s) due to a low signal to noise ratio. Therefore, we decide to undertake a classical biochemical purification approach as an enrichment strategy and aim to identify this resistance-promoting activity.

## *2.2 Biochemical fractionation indicates neuregulin 1 (NRG1)*

To identify the key protein(s) present in 22Pc-CAF$^{CM}$ responsible for antiandrogen resistance we undertook a biochemical fractionation approach and analyzed the resolved fractions in two parallel assays: (1) the 22Pc-EP growth assay as a readout of antiandrogen resistance-activity; (2) activation of human receptor tyrosine kinases (RTKs) in 22Pc-EP cells. The rationale for the RTK assay was based on prior work from our group and others demonstrating that RTK activation enables pro-tumorigenic AR bypass signaling in PCa(*96-98*). Furthermore, the GSEA of reactive prostate stroma revealed growth factor binding and RTK activity as highly enriched pathways (Figure 6D,E).

To carry out the purification, serum-free 22Pc-CAF$^{CM}$ was collected, concentrated and applied to a Q-Superose anion exchange column, from which we eluted two protein peaks by using 30% and 100% high-salt buffer B (termed Q30 and Q100 respectively; see STAR Methods for further detail) (Figure 7A). Resistance promoting activity resided in fraction Q30, but not Q100 (Figure 7B). Further resolving of Q30 by gradient elution on a Q-Superose column yielded fractions Q6-Q8 which promote 22Pc-EP growth in CSS (Figure 7C). In parallel, results from an RTK array showed that 22Pc-CAF$^{CM}$ strongly activated HER2 and HER3 in 22Pc-EP (Figure 7D). This result, as well as FGFR activation, was confirmed by western blot (Figure 7E,F). [We tested FGFR based on recent data implicating FGF in CRPC (*57*).] Analysis of Q30 and its subfractions, as well as Q100, for RTK activity revealed that HER3 (and downstream AKT) phosphorylation activity was present in Q30 but not Q100, and specifically in the Q6-10 subfractions of Q30. The fact that the resistance promoting activity elutes in precisely the same fractions as the HER3 phosphorylation activity (Figure 7G) suggests that two are functionally linked.

To determine whether HER3 activation contributes to resistance, we treated 22Pc-EP cells with a clinical-grade blocking antibody to HER3 or with small molecule inhibitors to HER2 (lapatinib and neratinib) or FGFR (AZD4547, BGJ398, PD173074). The HER3 blocking antibody and the HER2 kinase inhibitors blocked the resistance promoting activity of 22Pc-CAF$^{CM}$ whereas FGFR inhibitors did not, despite the pharmacological blockade of FGFR kinase activity (Figure 7H,I; Figure 8A-C). Since NRG1 (neuregulin-1) is the principal ligand for HER3 (*65*), we next asked if NRG1 could be detected in active Q subfractions. Indeed, we observed NRG1 protein exclusively in the active Q subfractions (Q6-10) from 22Pc-CAF$^{CM}$ (Figure 7G) but not in 22Pc-EP (Figure 7J, Figure 9C). To determine if other neuregulin family members are also expressed, we measured mRNA levels of Nrg1-4 by qRT-PCR and found that Nrg1 is the dominantly expressed neuregulin in 22Pc-CAF (Figure 9E).

Taken together, these data suggest that NRG1 acts in a paracrine manner to activate HER3 in tumor cells in vivo. Consistent with this model, Nrg1 mRNA levels (detected using mouse-specific Nrg1 primers) are significantly elevated in parental CWR22Pc tumor xenografts (which contain 22Pc-CAF) compared to 22Pc-EP tumors (Figure 9A). To determine the spatial relationship between Nrg1-expressing mouse cells and HER3-expressing tumor cells, we performed RNA in situ hybridization (RNA-ISH). Using a murine-specific RNA-ISH probe, Nrg1 mRNA was detected in the stromal compartment in both models (CWR22Pc and 22Pc-EP) but with a stronger signal in parental CWR22Pc xenografts (Figure 9B, brown dots). No signal was detected using a human NRG1 RNA-ISH probe, as expected (Figure 9D). To visualize the spatial expression pattern of Nrg1 relative to HER3, we applied multi-color RNA-FISH staining and found murine Nrg1 (green) co-localized with the stromal marker Vim (white) but not with human HER3 (red) staining (Figure 9F) providing further support for the model that NRG1 expressed by tumor-infiltrating CAFs acts on cancer cells through a paracrine mechanism.

### *2.3 Functional investigation of NRG1 in cell line, organoid and xenograft models*

Having established that HER3 activation is required for the resistance promoting activity of CAFs, we performed additional experiments to determine if NRG1 is the responsible factor. NRG1 is known to have >30 isoforms, all of which share the consensus EGF-like domain (*64, 65*). To determine if the loss of NRG1 in 22Pc-CAF impairs their ability to promote resistance, we targeted the EGF-like domain of Nrg1 using CRISPR-Cas9 to disrupt all isoforms (Figure 10A). Conditioned media from sgNrg1 22Pc-CAF had significantly reduced capacity to activate HER3/AKT phosphorylation and to promote resistance to CSS or Enz in 22Pc-EP compared with conditioned media from 22Pc-CAF expressing a non-targeting sgRNA (Figure 10B-D). As an independent confirmation of its essential role in conditioned media, we immunoprecipitated NRG1 from the 22Pc-CAF$^{CM}$ and found that NRG1-depleted conditioned media lost the ability to activate HER3-AKT and to promote resistance to CSS (Figure 11A,B). A clinical-grade NRG1α/β neutralizing antibody YW538.24.71 (Genentech) also blocked the ability of 22Pc-CAF$^{CM}$ to activate HER3/AKT as well as to promote resistance of 22Pc-EP to Enz or CSS (Figure 10E-G), as did the clinical-grade HER3 blocking antibody AMG888 (Figure 10H-J). To determine if NRG1 itself was sufficient to promote antiandrogen resistance in 22Pc-EP or if other ErbB RTK ligands such as EGF could substitute for NRG1, we treated 22Pc-EP with increasing concentrations of each. Recombinant NRG1 activated HER3/AKT and promoted resistance to CSS or Enz in 22Pc-EP. EGF also induced AKT phosphorylation (without inducing HER3 phosphorylation) but was not sufficient to confer resistance (Figure 10K-M). Recombinant NRG1 also promoted resistance to CSS or Enz in three additional human prostate models (22Rv1, LAPC4 and VCaP) (Figure 11C-F) and in organoids derived from three genetically engineered mouse models (P53-deficient, RB-deficient and PTEN$^{\Delta/\Delta}$ -Rosa26-ERG) (Figure 11G-L).

Having established paracrine NRG1-HER3 signaling as a primary driver of in vitro resistance in these models, we next explored the physiological relevance of this signaling using in vivo mouse xenograft models. We first documented increased levels of NRG1 (stroma) and phospho-HER3 (tumor cells) in lysates from CWR22Pc xenografts grown in castrated mice compared to intact mice (Figure 12A,B). We then treated established, castration-resistant CWR22Pc xenografts with a blocking antibody to HER3 (AMG888) or a HER2 kinase inhibitor (neratinib) and observed potent growth inhibition, as well as tumor regressions with combination therapy (Figure 12C,D). The NRG1 neutralizing antibody (YW538.24.71) also had potent antitumor activity in this assay, given alone or in combination with neratinib (Figure 12E-G). We extended these findings to a castration-sensitive model of CWR22Pc, showing that NRG1 blockade significantly enhanced the antitumor effect of castration, either alone or in combination with neratinib (Figure 12H,I). Corresponding analysis of tumor lysates confirmed the reduction of pHER2/pHER3 in mice treated with NRG1 or HER kinase inhibitors (Figure 12J-L). Thus, the dependence of prostate tumor cells on stromal-derived NRG1 translates to in vivo models and can potentially be exploited for therapeutic benefit using clinical-grade inhibitors of the NRG1-HER3 signaling axis.

### *2.4 Summary*

In this chapter, we successfully identified the resistance-promoting factor NRG1 through the combination of biochemical fractionation and RTK array. We further validated that NRG1 is both sufficient and required to promote antiandrogen and CSS resistance across different cell lines, organoids and xenograft models. Moreover, we also directly detected the spatial expression pattern of NRG1/Nrg1 in both xenografts and in clinical specimens. Importantly, inhibition of NRG1-HER3 signaling achieved a potent anti-tumor effect, indicating a potential for further test and pre-clinical development. We will begin to work out molecular mechanisms of NRG1 regulation and its relationship with AR signaling in the next chapter.

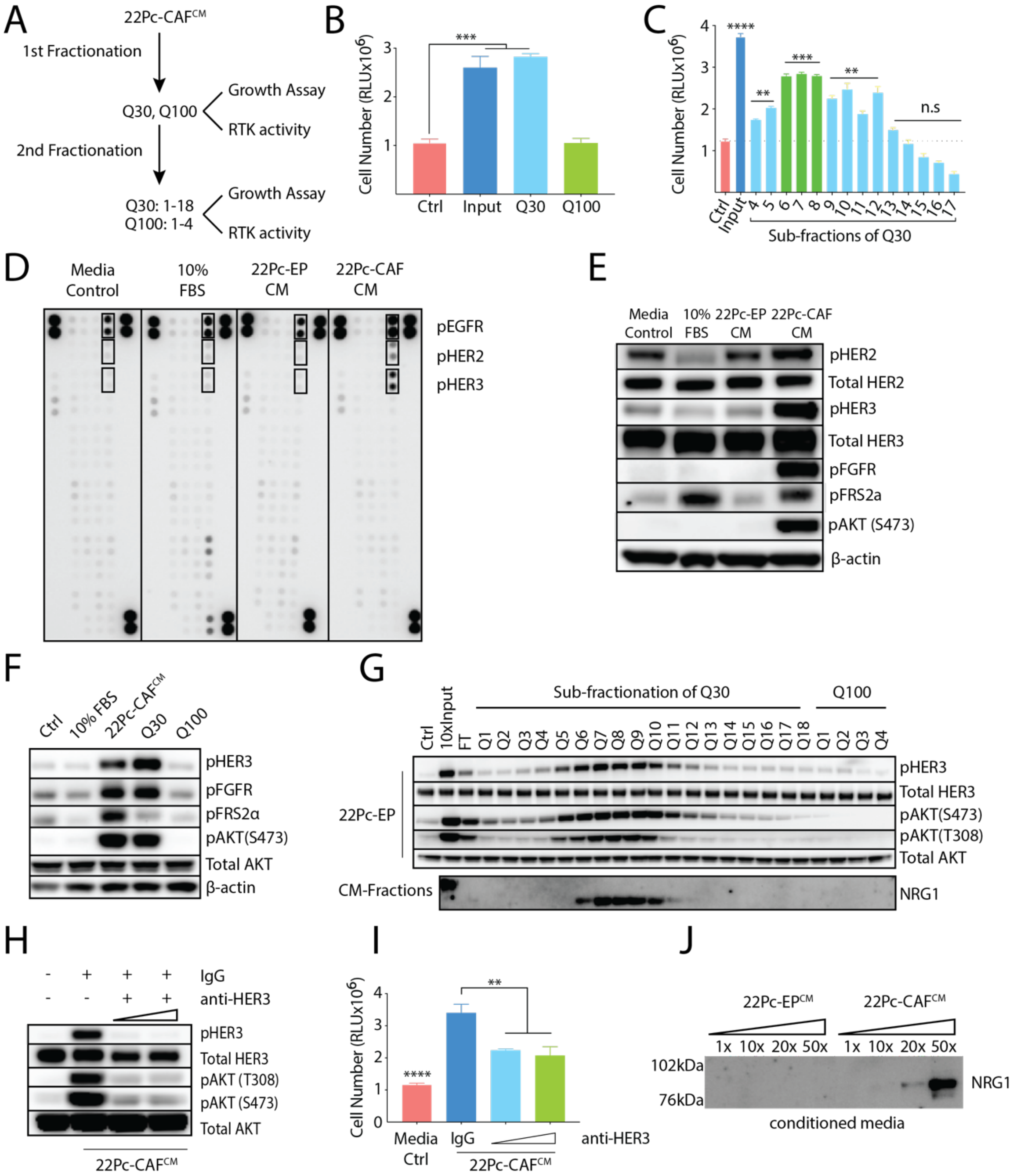
A
22Pc-CAF$^{CM}$
1st Fractionation
Q30, Q100
Growth Assay
RTK activity
2nd Fractionation
Q30: 1-18
Q100: 1-4
Growth Assay
RTK activity
B
Cell Number (RLUx10$^6$)
***
Ctrl
Input
Q30
Q100
C
Cell Number (RLUx10$^6$)
****
**
***
**
n.s
Ctrl
Input
4 5 6 7 8 9 10 11 12 13 14 15 16 17
Sub-fractions of Q30
D
Media Control
10% FBS
22Pc-EP CM
22Pc-CAF CM
pEGFR
pHER2
pHER3
E
Media Control
10% FBS
22Pc-EP CM
22Pc-CAF CM
pHER2
Total HER2
pHER3
Total HER3
pFGFR
pFRS2a
pAKT (S473)
β-actin
F
Ctrl
10% FBS
22Pc-CAF$^{CM}$
Q30
Q100
pHER3
pFGFR
pFRS2α
pAKT(S473)
Total AKT
β-actin
G
Sub-fractionation of Q30
Q100
Ctrl
10xInput
FT
Q1 Q2 Q3 Q4 Q5 Q6 Q7 Q8 Q9 Q10 Q11 Q12 Q13 Q14 Q15 Q16 Q17 Q18
Q1 Q2 Q3 Q4
22Pc-EP
pHER3
Total HER3
pAKT(S473)
pAKT(T308)
Total AKT
CM-Fractions
NRG1
H
IgG
anti-HER3
pHER3
Total HER3
pAKT (T308)
pAKT (S473)
Total AKT
22Pc-CAF$^{CM}$
I
Cell Number (RLUx10$^6$)
**
****
Media Ctrl
IgG
anti-HER3
22Pc-CAF$^{CM}$
J
22Pc-EP$^{CM}$
22Pc-CAF$^{CM}$
1x 10x 20x 50x
1x 10x 20x 50x
102kDa
76kDa
NRG1
conditioned media

Figure 7

**Figure 7. Biochemical fractionation of CAF-secreted resistance activity implicates neuregulin 1.**

(A) Schematics showing purification of resistance activity in 22Pc-CAF$^{CM}$. (B) Growth of 22Pc-EP cells in CSS media supplemented with purified fractions from input (22Pc-CAF$^{CM}$), Q30 or Q100. CellTiter-Glo reading on day 4. Ctrl: PBS. (C) Growth of 22Pc-EP cells in CSS media supplemented with sub-purified fractions (Q3-17) from Q30. CellTiter-Glo reading on day 4. Input: Q30, Ctrl: PBS. (D) Human Receptor Tyrosine Kinase (RTK) array analysis of 22Pc-EP after stimulation with either 10% FBS media, 22Pc-EP$^{CM}$ or 22Pc-CAF$^{CM}$ or serum free media control. (E) Western blot analysis of HER2/3-AKT activation in 22Pc-EP cell lysates from S3A. β-actin serves as loading control. (F) Western blot analysis of HER3 and FGFR activation in 22Pc-EP after stimulation with either FBS media, 22Pc-CAF$^{CM}$, Q30 or Q100. Ctrl: PBS. β-actin serves as loading control. (G) Western blot analysis of HER3-AKT activation in 22Pc-EP after stimulation with different Q fractions and analysis of secreted NRG1 in corresponding fractions. Ctrl: PBS, Input: Q30, FT: Flow Through. Total AKT serves as loading control. (H) Western blot analysis of HER3-AKT activation in 22Pc-EP after stimulation with 22Pc-CAF$^{CM}$ in the presence of a commercial HER3 blocking antibody (10μg/mL, 30μg/mL) or IgG (30μg/mL). Total AKT serves as loading control. (I) Growth of 22Pc-EP cells in CSS media supplemented with 22Pc-CAF$^{CM}$ treated with a commercial HER3 blocking antibody (10μg/mL, 30μg/mL) or IgG (30μg/mL). CellTiter-Glo reading on day 4. Media Ctrl: serum free media. (J) Western blot analysis of NRG1 from 22Pc-EP$^{CM}$ or 22Pc-CAF$^{CM}$ (concentrated 1x, 10x, 20x or 50x). (****$p<0.0001$, ***$p<0.001$, **$p<0.01$, *$p<0.05$, n.s: not significant, B,C: one-way ANOVA compared to Ctrl group, I: Student's t-test compared to anti-HER3 group, error bar represents ±SD)

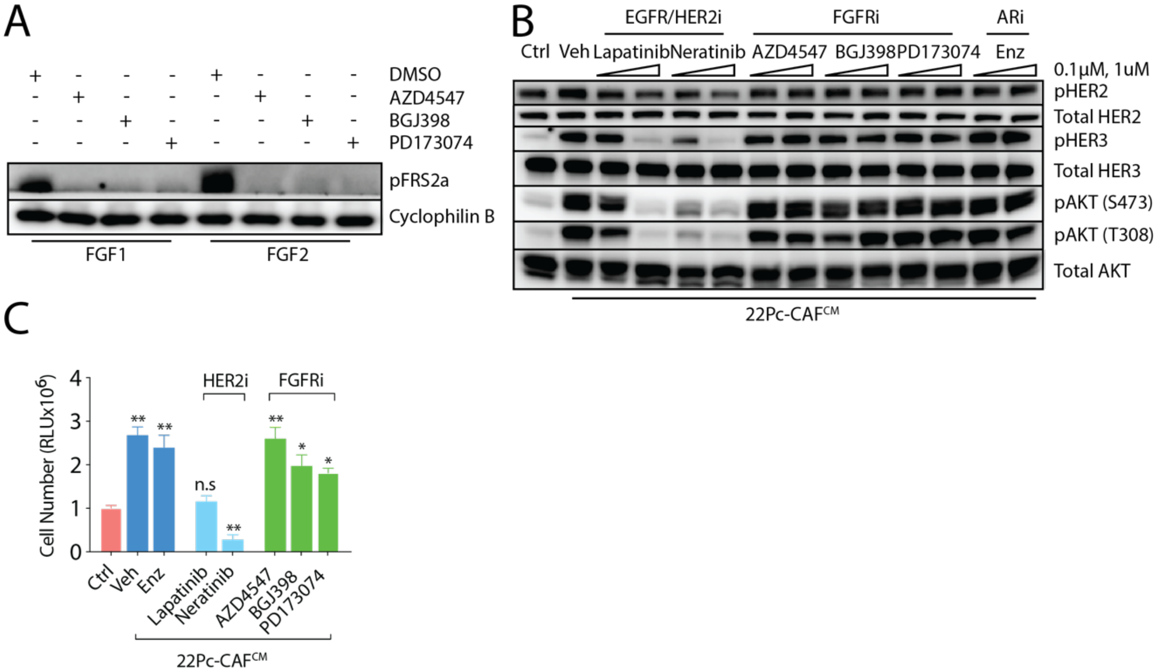

**Figure 8. NRG1-HER3 axis but not FGFR activity mediates antiandrogen resistance in 22Pc-EP.**
(A) Western blot analysis of FGFR activation (pFRS2a) in 22Pc-EP cells after stimulation with FGF1 or FGF2 (50ng/mL) in the presence of different FGFR inhibitors (AZD4547, BGJ398 or PD173074, each at 1µM). Cyclophilin B serves as loading control. (B) Western blot analysis of HER3-PI3K activation in 22Pc-EP cells after stimulation with 22Pc-CAF$^{CM}$ in the presence of inhibitors of either AR (Enz: 0.1µM, 1µM), HER2 (lapatinib: 0.1µM, 1µM or neratinib: 0.1µM, 1µM), FGFR (AZD4547, BGJ398, PD173074; each at 0.1µM, 1µM) or Veh (DMSO). Total AKT serves as loading control. Ctrl: serum free media. (C) Growth of 22Pc-EP cells in CSS media supplemented with 22Pc-CAF$^{CM}$ in the presence of HER2 inhibitors (lapatinib: 1µM or neratinib: 0.1µM), FGFR inhibitors (AZD4547, BGJ398, PD173074, each at 1µM) or Veh (DMSO). CellTiter-Glo reading on day 4. Ctrl: serum free media (**p<0.01, *p<0.05, n.s: not significant, one-way ANOVA, error bar represents ±SD).

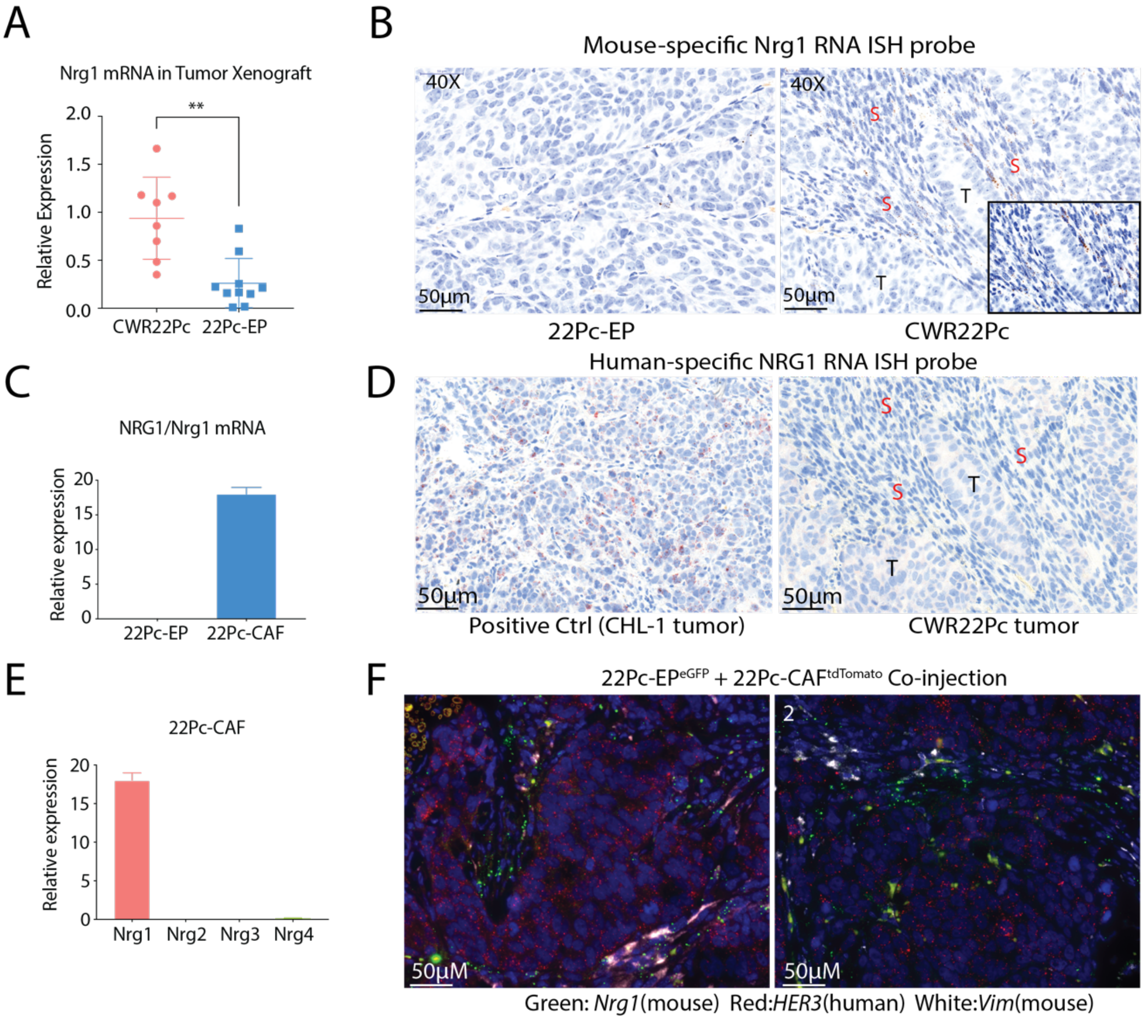

**Figure 9. NRG1 is expressed in the stroma of tumor xenografts.**
(A) qRT-PCR analysis of Nrg1 expression in CWR22Pc or 22Pc-EP tumor xenografts using mouse specific primers (**p<0.01, Student's t-test. n=8 tumors in CWR22Pc group and n=10 tumors in 22Pc-EP group). (B) Representative images showing RNA in situ hybridization (ISH) analysis of mouse Nrg1 expression in CWR22Pc or 22Pc-EP tumor xenografts. T: tumor, S: stroma, mouse specific Nrg1 probe: brown dots. (C) qRT-PCR analysis of NRG1/Nrg1 expression in 22Pc-EP or 22Pc-CAF using species-specific primers. NRG1/Nrg1 expression was normalized to *ACTB/Actb*. (D) Representative images showing RNA in situ hybridization (ISH) analysis of human NRG1 expression in CWR22Pc tumor xenografts. An NRG1 positive human melanoma tumor xenograft (CHL-1) was used as a positive control (T: tumor, S: stroma, human specific NRG1 probe: red dots). (E) qRT-PCR analysis of different Nrg1 family member expressions in 22Pc-CAF. Nrg1 expression was normalized to *Actb*. (F) Representative images showing RNA-FISH analysis of Nrg1 expression in two independent CWR22Pc tumor xenografts (Green: mouse-*Nrg1*, Red: human-*HER3*, White: mouse-*Vim* and Blue: DAPI).

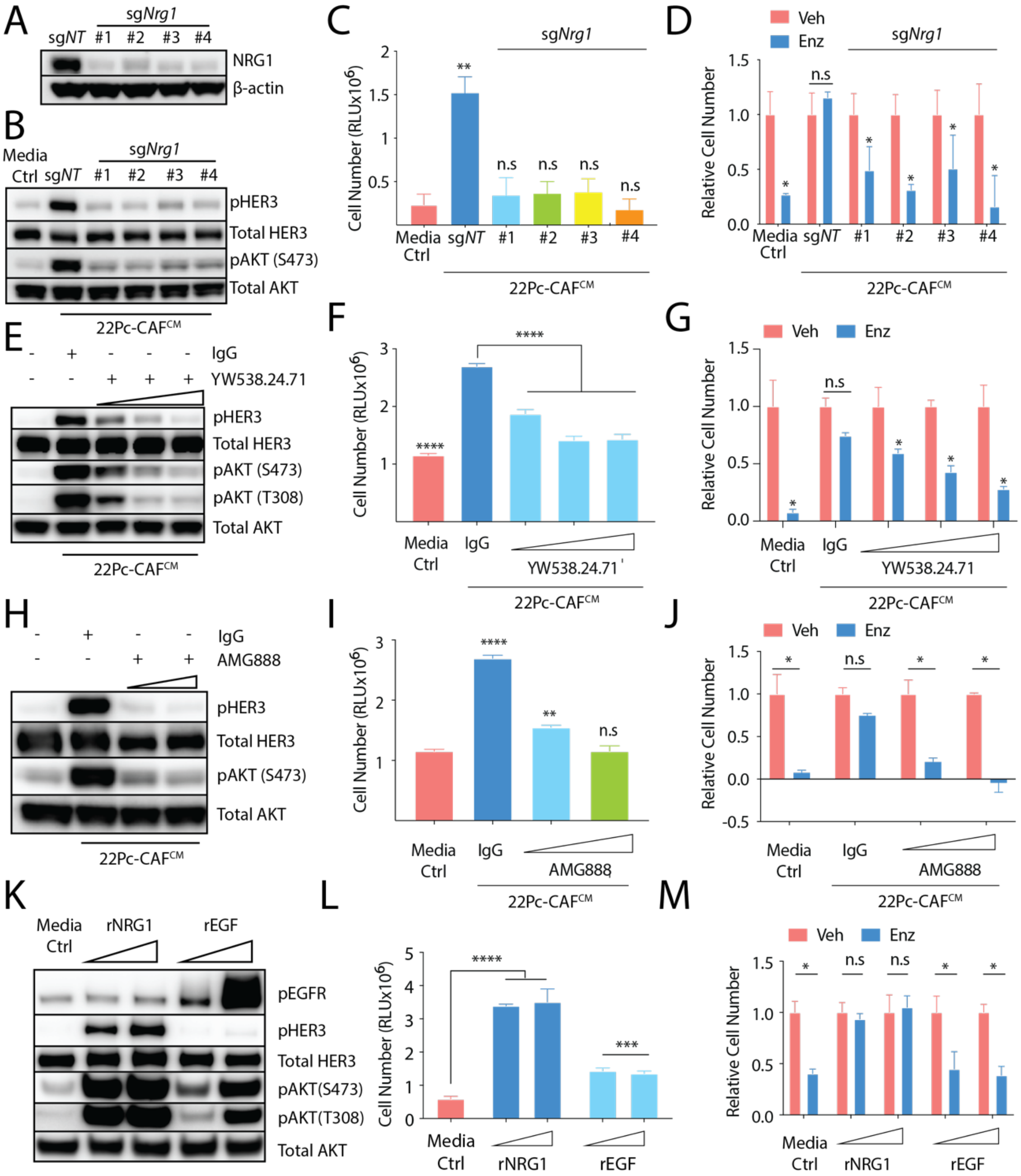
A
sgNrg1
sgNT #1 #2 #3 #4
NRG1
β-actin
B
Media Ctrl sgNT
sgNrg1
#1 #2 #3 #4
pHER3
Total HER3
pAKT (S473)
Total AKT
22Pc-CAF^CM
C
sgNrg1
Cell Number (RLUx10^6)
2
1.5
1
0.5
**
n.s
n.s
n.s
n.s
Media Ctrl sgNT #1 #2 #3 #4
22Pc-CAF^CM
D
Veh
Enz
sgNrg1
Relative Cell Number
1.5
1.0
0.5
0.0
n.s
*
*
*
*
*
Media Ctrl sgNT #1 #2 #3 #4
22Pc-CAF^CM
E
- + - - - IgG
- - + + + YW538.24.71
pHER3
Total HER3
pAKT (S473)
pAKT (T308)
Total AKT
22Pc-CAF^CM
F
Cell Number (RLUx10^6)
3
2
1
****
****
Media Ctrl
IgG
YW538.24.71
22Pc-CAF^CM
G
Veh
Enz
Relative Cell Number
1.5
1.0
0.5
0.0
n.s
*
*
*
*
Media Ctrl
IgG
YW538.24.71
22Pc-CAF^CM
H
- + - - IgG
- - + + AMG888
pHER3
Total HER3
pAKT (S473)
Total AKT
22Pc-CAF^CM
I
Cell Number (RLUx10^6)
3
2
1
****
**
n.s
Media Ctrl
IgG
AMG888
22Pc-CAF^CM
J
Veh
Enz
Relative Cell Number
1.5
1.0
0.5
0.0
-0.5
*
n.s
*
*
Media Ctrl
IgG
AMG888
22Pc-CAF^CM
K
Media Ctrl
rNRG1
rEGF
pEGFR
pHER3
Total HER3
pAKT(S473)
pAKT(T308)
Total AKT
L
Cell Number (RLUx10^6)
5
4
3
2
1
0
****
***
Media Ctrl
rNRG1
rEGF
M
Veh
Enz
Relative Cell Number
1.5
1.0
0.5
0.0
*
n.s
n.s
*
*
Media Ctrl
rNRG1
rEGF

Figure 10

**Figure 10. NRG1 is both sufficient and required to promote antiandrogen resistance in 22Pc-EP.**

(A) Western blot analysis of NRG1 expression in 22Pc-CAF where *Nrg1* was deleted using CRISPR-Cas9. *sgNT*: non-targeting guide control, *sgNrg1* (#1-4): four independent guides targeting *Nrg1*. β-actin serves as loading control. (B) Western blot analysis of HER3-AKT activation in 22Pc-EP after stimulation with either *sgNT*- or *sgNrg1*- 22Pc-CAF$^{CM}$. Total AKT serves as loading control. (C) Growth of 22Pc-EP cells in CSS media supplemented with either *sgNT*- or *sgNrg1*- 22Pc-CAF$^{CM}$. CellTiter-Glo reading on day 4. Media Ctrl: serum free media. (D) Growth of 22Pc-EP cells in FBS media supplemented with either *sgNT*- or *sgNrg1*- 22Pc-CAF$^{CM}$ treated with Enz (0.1μM) or Veh (DMSO). Enz group was normalized to Veh group. CellTiter-Glo reading on day 7. Media Ctrl: serum free media. (E) Western blot analysis of HER3-AKT activation in 22Pc-EP cells after stimulation with 22Pc-CAF$^{CM}$ in the presence of either NRG1 neutralizing antibody YW538.24.71 (1, 10 or 100μg/mL) or IgG (100μg/mL). Total AKT serves as loading control. (F) Growth of 22Pc-EP cells in CSS media supplemented with 22Pc-CAF$^{CM}$ treated with YW538.24.71 (1μg/mL, 10μg/mL or 20μg/mL) or IgG (20μg/mL). CellTiter-Glo reading on day 4. Media Ctrl: serum free media. (G) Growth of 22Pc-EP cells in Enz (0.1μM) or Veh (DMSO) containing FBS media supplemented with 22Pc-CAF$^{CM}$ treated with YW538.24.71 (1μg/mL, 10μg/mL or 20μg/mL) or IgG (20μg/mL). Enz group was normalized to Veh group. CellTiter-Glo reading on day 7. Media Ctrl: serum free media. (H) Western blot analysis of HER3-AKT activation in 22Pc-EP after stimulation with 22Pc-CAF$^{CM}$ in the presence of a HER3 blocking antibody AMG888 (1μg/mL, 10μg/mL) or IgG (10μg/mL). Total AKT serves as loading control.(I) Growth of 22Pc-EP cells in CSS media supplemented with 22Pc-CAF$^{CM}$ treated with AMG888 (1μg/mL, 10μg/mL) or IgG (10μg/mL). CellTiter-Glo reading on day 4. Media Ctrl: serum free media. (J) Growth of 22Pc-EP cells in Enz (0.1μM) or Veh (DMSO) containing FBS media supplemented with 22Pc-CAF$^{CM}$ treated with AMG888 (1μg/mL, 10μg/mL) or IgG (10μg/mL). Enz group was normalized to Veh group. CellTiter-Glo reading on day 7. Media Ctrl: serum free media. (K) Western blot analysis of HER3-AKT activation in 22Pc-EP after stimulation with either recombinant NRG1 or EGF (10ng, 50ng/mL). Total AKT serves as loading control. (L) Growth of 22Pc-EP in CSS media supplemented with either recombinant NRG1 or EGF (10ng, 50ng/mL). CellTiter-Glo reading on day 4. Media Ctrl: serum free media.(M) Growth of 22Pc-EP cells in Enz (0.1μM) or Veh (DMSO) containing FBS media treated with recombinant NRG1 or EGF (10ng, 50ng/mL). Enz group was normalized to Veh group. CellTiter-Glo reading on day 7. Media Ctrl: serum free media. (**** $p<0.0001$, ***$p<0.001$, **$p<0.01$, *$p<0.05$, n.s: not significant, C,D,F,G,I,J,L,M: Student's t-test, error bar represents ±SD)

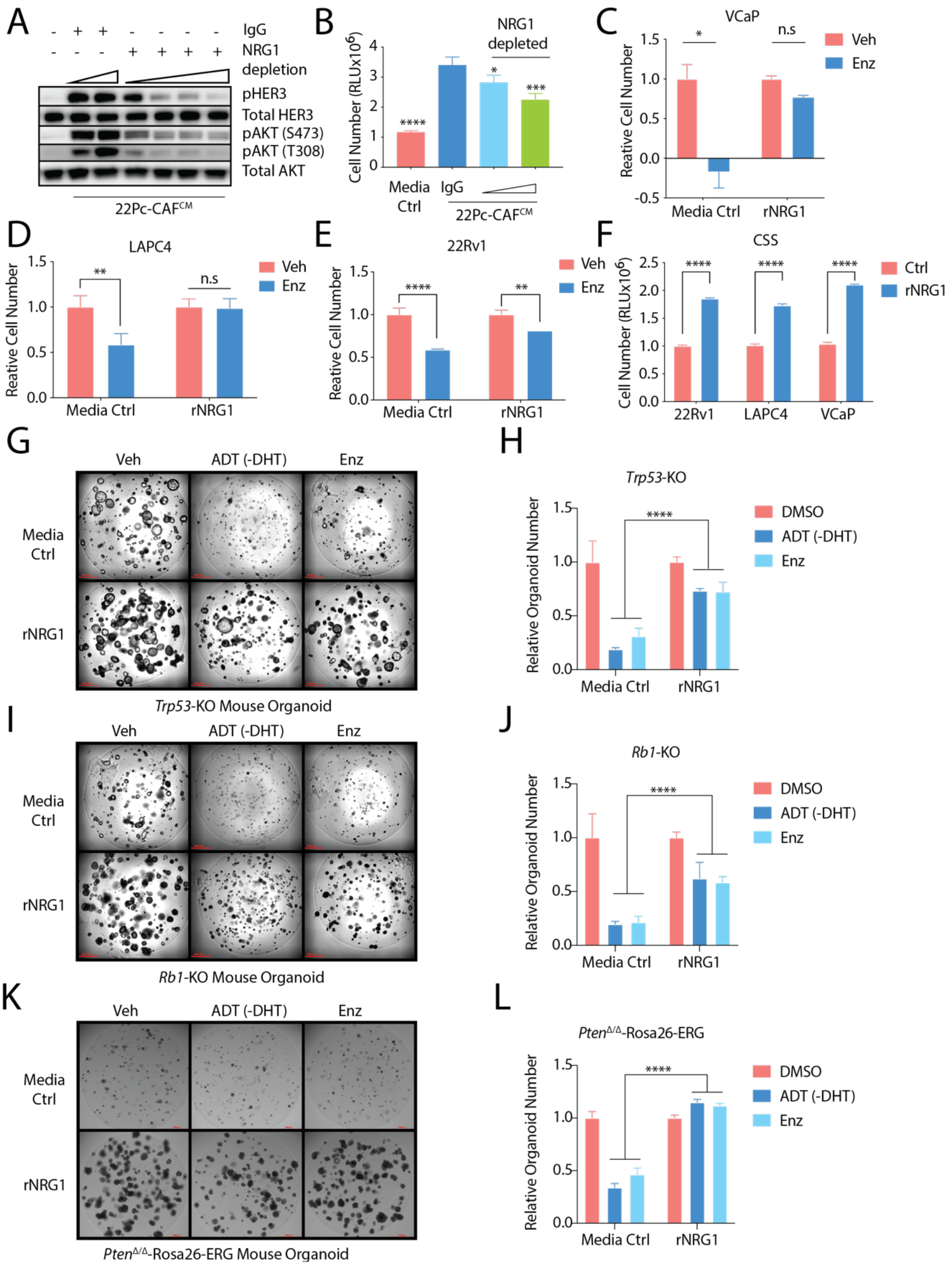
A
IgG
NRG1 depletion
pHER3
Total HER3
pAKT (S473)
pAKT (T308)
Total AKT
22Pc-CAF^CM
B
NRG1 depleted
Cell Number (RLUx10^6)
****
*
***
Media Ctrl
IgG
22Pc-CAF^CM
C
VCaP
Reative Cell Number
*
n.s
Veh
Enz
Media Ctrl
rNRG1
D
LAPC4
Reative Cell Number
**
n.s
Veh
Enz
Media Ctrl
rNRG1
E
22Rv1
Reative Cell Number
****
**
Veh
Enz
Media Ctrl
rNRG1
F
CSS
Cell Number (RLUx10^6)
****
****
****
Ctrl
rNRG1
22Rv1
LAPC4
VCaP
G
Veh
ADT (-DHT)
Enz
Media Ctrl
rNRG1
Trp53-KO Mouse Organoid
H
Trp53-KO
Relative Organoid Number
****
DMSO
ADT (-DHT)
Enz
Media Ctrl
rNRG1
I
Veh
ADT (-DHT)
Enz
Media Ctrl
rNRG1
Rb1-KO Mouse Organoid
J
Rb1-KO
Relative Organoid Number
****
DMSO
ADT (-DHT)
Enz
Media Ctrl
rNRG1
K
Veh
ADT (-DHT)
Enz
Media Ctrl
rNRG1
Pten^Δ/Δ-Rosa26-ERG Mouse Organoid
L
Pten^Δ/Δ-Rosa26-ERG
Relative Organoid Number
****
DMSO
ADT (-DHT)
Enz
Media Ctrl
rNRG1

Figure 11

**Figure 11. NRG1 mediates antiandrogen resistance in multiple androgen-dependent cell line and organoid models.**

(A) Western blot analysis of HER3-AKT activation in 22Pc-EP after stimulation with 22Pc-CAF$^{CM}$ where NRG1 was depleted by immunoprecipitation using a commercial NRG1 antibody (1,10, 30 and 100µg/mL) or IgG (100µg/mL). Total AKT serves as loading control. (B) Growth of 22Pc-EP cells in CSS media supplemented with NRG1-immunodepleted 22Pc-CAF$^{CM}$ by a NRG1 immunoprecipitation antibody (10, 30µg/mL). CellTiter-Glo reading on day 4. Media Ctrl: serum free media. (C) Growth of VCaP cells in Veh (DMSO) or Enz (1µM) containing FBS media supplemented with recombinant NRG1 (10ng/mL). CellTiter-Glo reading on day 7. Enz group is normalized to Veh group. Media Ctrl: serum free media. (D) Growth of LAPC4 cells in Veh (DMSO)/FBS media or Enz (10µM)/CSS media supplemented with recombinant NRG1 (10ng/mL). CellTiter-Glo reading on day 7. Enz group is normalized to Veh group. Media Ctrl: serum free media. (E) Growth of 22Rv1 cells in Veh (DMSO)/FBS media or Enz (10µM)/CSS media supplemented with recombinant NRG1 (10ng/mL). CellTiter-Glo reading on day 7. Enz group is normalized to Veh group. Media Ctrl: serum free media. (F) Growth of 22Rv1, LAPC4 or VCaP cells in CSS media supplemented with recombinant NRG1 (10ng/mL). CellTiter-Glo reading on day 4. Ctrl: serum free media. (G) Representative images showing Trp53-KO mouse organoids in 3D culture supplemented with recombinant NRG1 and were treated with DHT depletion (ADT), Enz (1uM) or Veh (DMSO). Images are taken on day 7 with 4x objective. (H) Growth of Trp53-KO mouse organoids in 3D culture supplemented with recombinant NRG1 (10ng/mL) and were treated with ADT, Enz (1uM) or Veh (DMSO). CellTiter-Glo reading on day 7. ADT or Enz was normalized to DMSO group. Ctrl: EGF-deficient organoid media. (I) Representative images showing Rb1-KO mouse organoids in 3D culture supplemented with recombinant NRG1 and were treated with ADT, Enz (1uM) or Veh (DMSO). Images were taken on day 7 with 4x objective. (J) Growth of Rb1-KO mouse organoids in 3D culture supplemented with recombinant NRG1 (10ng/mL) and were treated with ADT or Enz (1uM) or Veh (DMSO). CellTiter-Glo reading on day 7. ADT or Enz was normalized to DMSO group. Ctrl: EGF-deficient organoid media. (K) Representative images showing *Pten*$^{\Delta/\Delta}$-Rosa26-ERG mouse organoids in 3D culture supplemented with recombinant NRG1 and were treated with ADT, Enz (1uM) or Veh (DMSO). Images were taken on day 7 with 4x objective. (L) Growth of *Pten*$^{\Delta/\Delta}$-Rosa26-ERG mouse organoids in 3D culture supplemented with recombinant NRG1 (10ng/mL) and were treated with ADT or Enz (1uM) or Veh (DMSO). CellTiter-Glo reading on day 7. ADT or Enz was normalized to DMSO group. Ctrl: EGF-deficient organoid media. (****$p<0.0001$, ***$p<0.001$, *$p<0.05$, n.s: not significant, C-F, Student’s t-test, H,J,L: one-way ANOVA compared to Ctrl group, error bar represents ±SD)

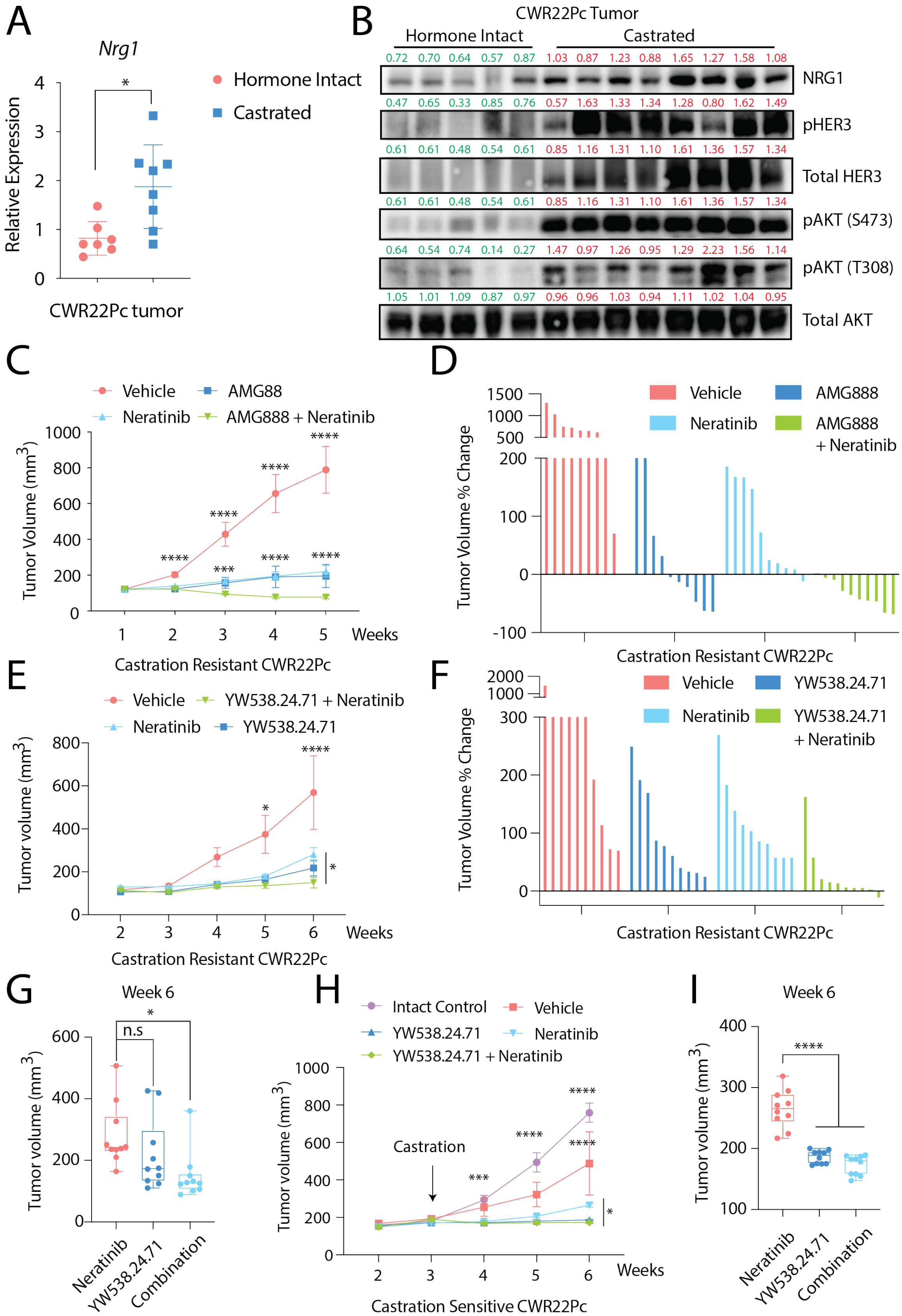

Figure 12 Part 1

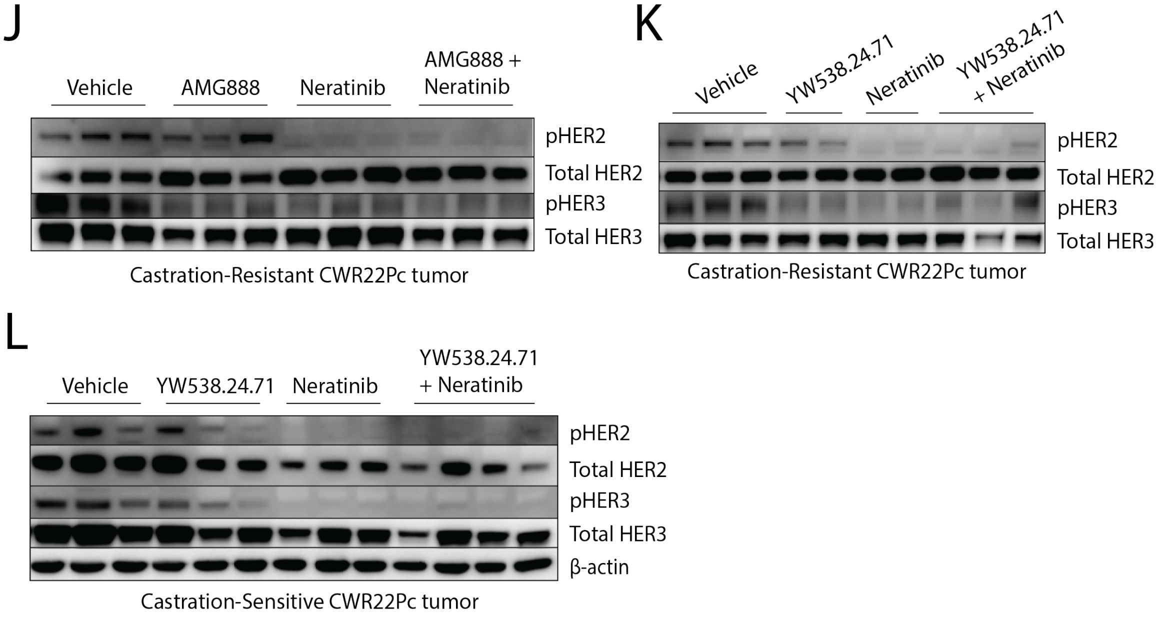

Figure 12 Part 2

**Figure 12. NRG1-HER3 signaling confers antiandrogen resistance in vivo.**
(A) qRT-PCR analysis of Nrg1 mRNA expression in hormone intact or castration - resistant CWR22Pc tumors. (B) Western blot analysis of NRG1 expression and HER3-AKT activation in hormone intact or castration-resistant CWR22Pc tumors. Total AKT serves as loading control. Bands were quantified using ImageJ and normalized to mean of β-actin intensity in each group. Green: Hormone Intact. Red: Castrated. (C) Growth of castration-resistant CWR22Pc tumor xenografts in castrated mice, treated with AMG888 (20mg/kg), neratinib (20mg/kg) or vehicle. Treatment started when tumors reached 150mm3 (n=5 mice per group). (D) Waterfall plot showing growth of individual tumors from 5C. (E) Growth of castration-resistant CWR22Pc tumor xenografts in castrated mice, treated with YW538.24.71 (20mg/kg), neratinib (20mg/kg) or vehicle. Treatment started when tumors reached 150mm3 (n=5 mice per group). (F) Waterfall plot showing growth of individual tumors from 5E. (G) Box plot showing tumor size at week 6 in single agent neratinib or YW538.24.71 versus combination treatment groups from 5E.(H) Growth of castration sensitive CWR22Pc tumor xenografts in intact mice, treated with castration plus either YW538.24.71 (20mg/kg), neratinib (20mg/kg) or vehicle. Treatment started when tumors reached 200mm3 (n=5 mice per group). (I) Box plot showing tumor size at week 6 in single agent neratinib or YW538.24.71 versus combination treatment groups in 12H. (J) Western blot analysis of HER2/HER3 activation in castration-resistant CWR22Pc tumors treated with AMG888 (20mg/kg), neratinib (20mg/kg) or vehicle (DMSO). Total HER3 serves as loading control. (K) Western blot analysis of HER2/HER3 activation in castration-resistant CWR22Pc tumors treated with YW538.24.71 (25mg/kg), neratinib (20mg/kg) or vehicle (DMSO). Total HER3 serves as loading control. (L) Western blot analysis of HER2/HER2 activation in castration sensitive CWR22Pc tumors treated with castration plus AMG888 (20mg/kg), neratinib (20mg/kg) or vehicle (DMSO). β-actin serves as loading control. (****$p<0.0001$, ***$p<0.001$, *$p<0.05$, n.s: not significant, A,G,I: Student's t-test, error bar represents ±SD, C,E,H: multiple t-test, error bar represents ±SEM)

# CHAPTER 3

## *3.1 Introduction*

In the last chapter we have provided both in vitro and in vivo evidence that NRG1 is responsible to mediate resistance to antiandrogens across different pre-clinical models. We have also made some interesting observations. For example, the expression of NRG1 is significantly higher in CRPC tumor xenografts compared to castration sensitive tumors. As we also showed by IHC and RNA-ISH, NRG1/Nrg1 expression is restricted to the stroma, which made us hypothesize that AR inhibition may cause NRG1 up-regulation through an unknown mechanism. Thus, we set out to further investigate how AR activity and NRG1 activity interact. Understanding this molecular mechanism will provide us insights into both AR signaling regulation as well as how we could use this knowledge to modulate AR signaling in a clinically relevant context.

## *3.2 NRG1 is induced by androgen deprivation therapy*

To examine if the up-regulation of NRG1 is induced by hormone therapy, we treated freshly isolated primary CAFs from CWR22Pc tumors or pCAFs with CSS or Enz. CSS and Enz both induced NRG1 mRNA and protein expression after 7 days, with the highest induction seen with the combination of CSS plus Enz (Figure 13A-D) a finding confirmed in pCAF isolates from 15 of 18 additional patients (Figure 13E).

## *3.3 Androgen receptor (AR) inhibition indirectly regulates NRG1*

To investigate the mechanism underlying NRG1 upregulation following AR inhibition, we performed time-course experiments and observed consistent changes in NRG1 levels 7 days after androgen withdrawal but not after 24 hours (Figure 14A). NRG1 levels returned to baseline after replenishing androgen in the culture media but also after 7 days (Figure 14B,C). This delayed response to AR pathway perturbation suggests an indirect mechanism of NRG1 regulation, which is further supported by our failure to detect AR peaks in the NRG1 promoter or enhancer in datasets from prostate cancer-derived CAFs, whereas strong AR peaks are present in the FKBP5 promoter region (Figure 14D). Thus, NRG1 is expressed in tumor-associated stromal cells of primary prostate cancers at increased levels following ADT treatment, and these levels are sufficient to promote resistance to ADT in vitro and in vivo.

### *3.4 NRG1 activates a subset of AR target genes*

Our earlier analysis of five canonical AR target genes suggested that NRG1 preserves tumor cell viability without restoring AR target gene expression (Figure 4G,H). To address this question more comprehensively, we performed a whole transcriptome analysis of 22Pc-EP cells treated with recombinant NRG1, Enz or both (Figure 15A,B) and generated an AR signature, defined as Enz-suppressed genes ($p<0.05$, log2 fold change>2) (Figure 15K). Gene Set Enrichment Analysis (GSEA) using this 22Pc-EP derived AR signature, as well as two independent AR signatures, showed that AR transcriptional activity is not enriched by NRG1 treatment (Figure 15C, L and M). as suggested by our earlier analysis of a limited number of canonical AR target genes. However, comparison of NRG1- versus AR-regulated transcriptomes revealed 1917 co-regulated genes ($p<0.05$) which subdivide into 4 major clusters by unsupervised clustering (Figure 15D-I). Cluster 1 is of particular interest because these genes are suppressed by Enz but restored by NRG1 (Figure 15J). and therefore may play a functional role in maintaining tumor cell viability. Of note, this cluster is enriched for genes involved in amino acid and folate metabolism based on Go Term Pathway Analysis (log2 fold change>0.5, 103 out of 308) (Figure 15N).

### *3.5 Summary*

In this chapter, we have shown that AR signaling suppresses NRG1 expression through an indirect transcriptional mechanism. It is also possible that NRG1-HER3 signaling can regulate AR activity through a post-translational mechanism. For example, in a PTEN-deficient background, activation of HER3-PI3K signaling can stabilize AR protein. Although in the PTEN wild-type 22Pc-EP model, we observed NRG1 does not reactivate most of canonical AR target genes when AR was inhibited by Enz, we do found a handful of genes that are specifically activated by NRG1, many of which are related with folate and amino acid metabolism. Thus, we postulate that when AR signaling was inhibited, the up-regulation of NRG1 from the tumor-stroma may serve as a paracrine mechanism to activate HER3 signaling in the cancer cell and promoting resistance through rewiring the metabolism in the tumor. This warrants further molecular investigations.

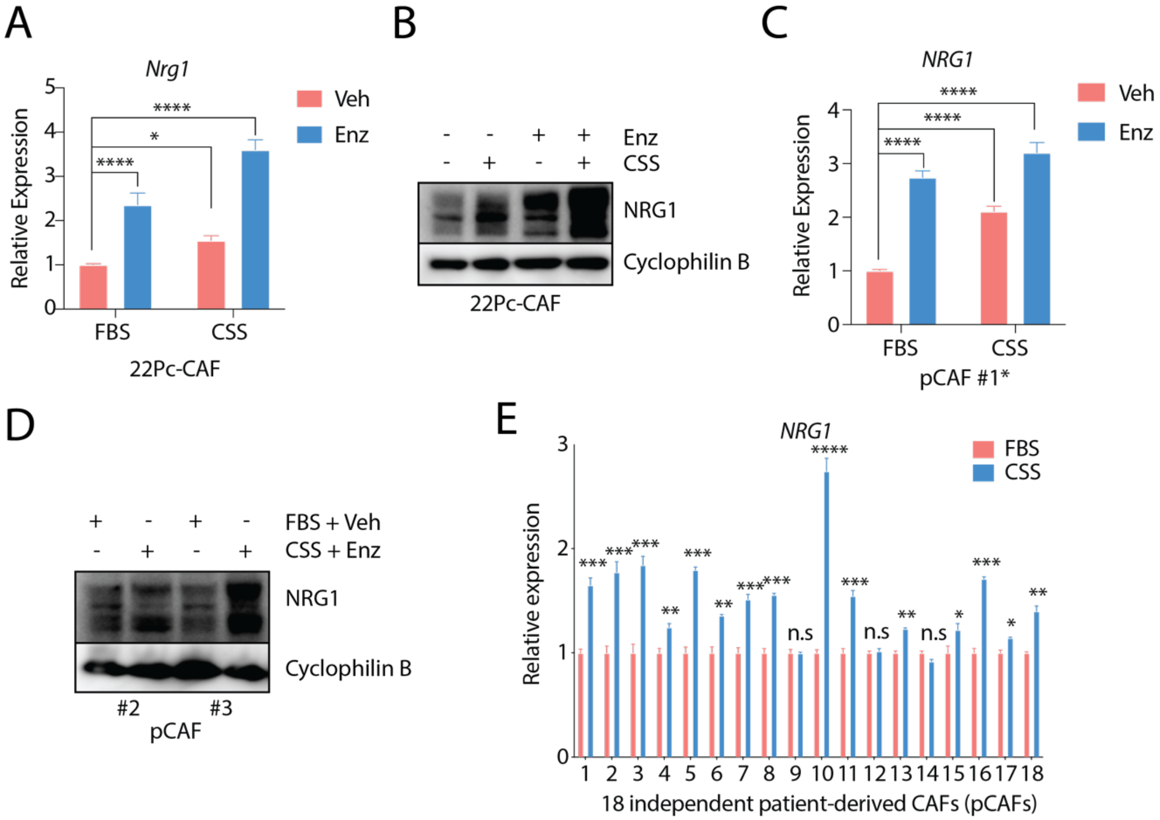

**Figure 13. NRG1 is up-regulated by AR-inhibition.**
(A) qRT-PCR analysis of *Nrg1* mRNA expression in 22Pc-CAF treated with CSS, Enz (10µM) or Veh (DMSO). *Nrg1* expression is normalized to *Actb*. (B) Western blot analysis of NRG1 protein in 22Pc-CAF treated with CSS, Enz (10µM) or Veh (DMSO). Cyclophilin B serves as loading control. (C) qRT-PCR analysis of NRG1 mRNA expression in a patient-derived CAF treated with CSS, Enz (10uM) or Veh (DMSO) on day 7. *NRG1* expression is normalized to *ACTB*. (D) Western blot analysis of NRG1 protein in two additional patient-derived CAFs treated with CSS, Enz (10uM) or Veh (DMSO) on day 7. Cyclophilin B serves as loading control. (E) qRT-PCR analysis of *NRG1* mRNA expression in a collection of patient-derived CAFs grown in FBS or CSS for 7 days (n=18). *NRG1* expression is normalized to *ACTB*. (Gene expression assays were performed with three biological replicates. ****$p<0.0001$, ***$p<0.001$, **$p<0.01$, *$p<0.05$, n.s: not significant, A-C: one-way ANOVA compared to FBS/Veh group, E, Student's t-test, error bar represents mean±SD)

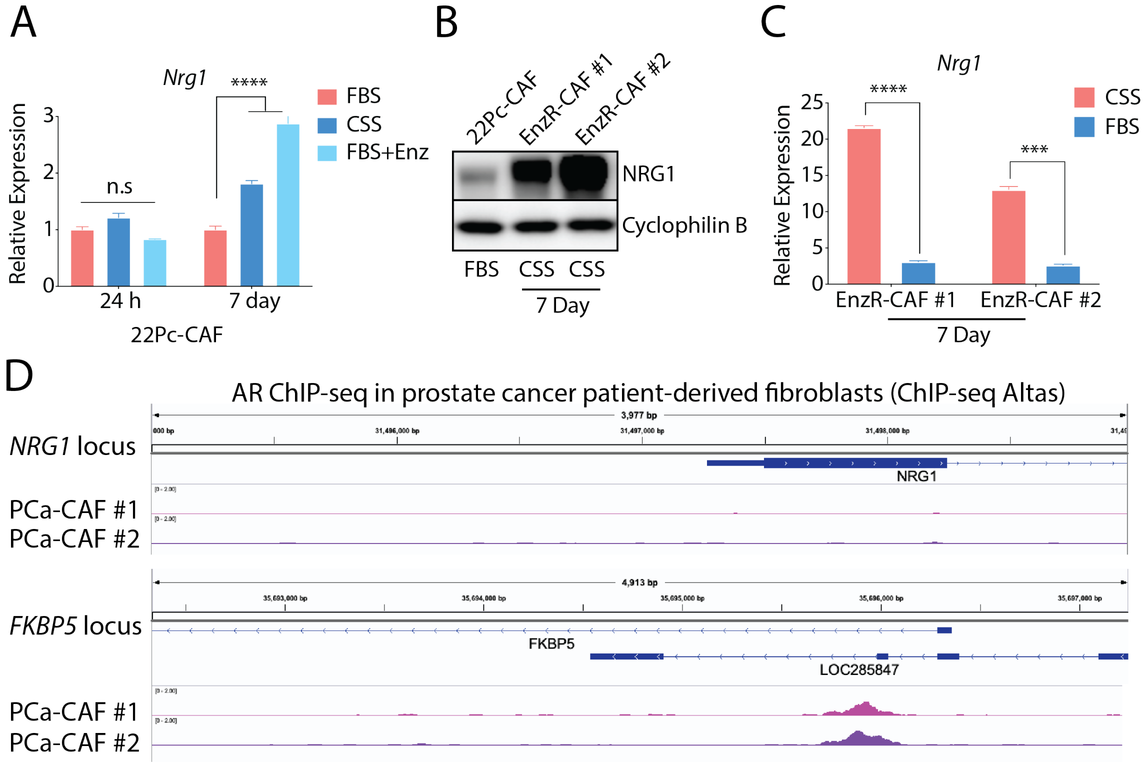

**Figure 14. AR activity regulates NRG1 expression indirectly.**
(A) qRT-PCR analysis of Nrg1 mRNA expression in 22Pc-CAF grown in FBS, CSS or FBS+Enz for 24 h or 7 days. *Nrg1* expression is normalized to *Actb*. (B) Western blot analysis of NRG1 expression in 22Pc-CAF (grown in FBS) and in two enzalutamide resistant CWR22Pc tumor derived CAFs (EnzR-CAF #1 and #2, grown in CSS) for 7 days. Cyclophilin B serves as loading control. (C) qRT-PCR analysis of *Nrg1* mRNA expression in both EnzR-CAFs between CSS and FBS conditions. *Nrg1* expression is normalized to *Actb*. (D) IGV graphs showing AR binding peaks at *NRG1* and *FKBP5* locus in patient-derived prostate cancer CAFs. (Gene expression assays were performed with three biological replicates. ****p<0.0001, ***p<0.001, **p<0.01, *p<0.05, n.s: not significant, A: one-way ANOVA compared to FBS/Veh group, C, Student's t-test, error bar represents mean±SD)

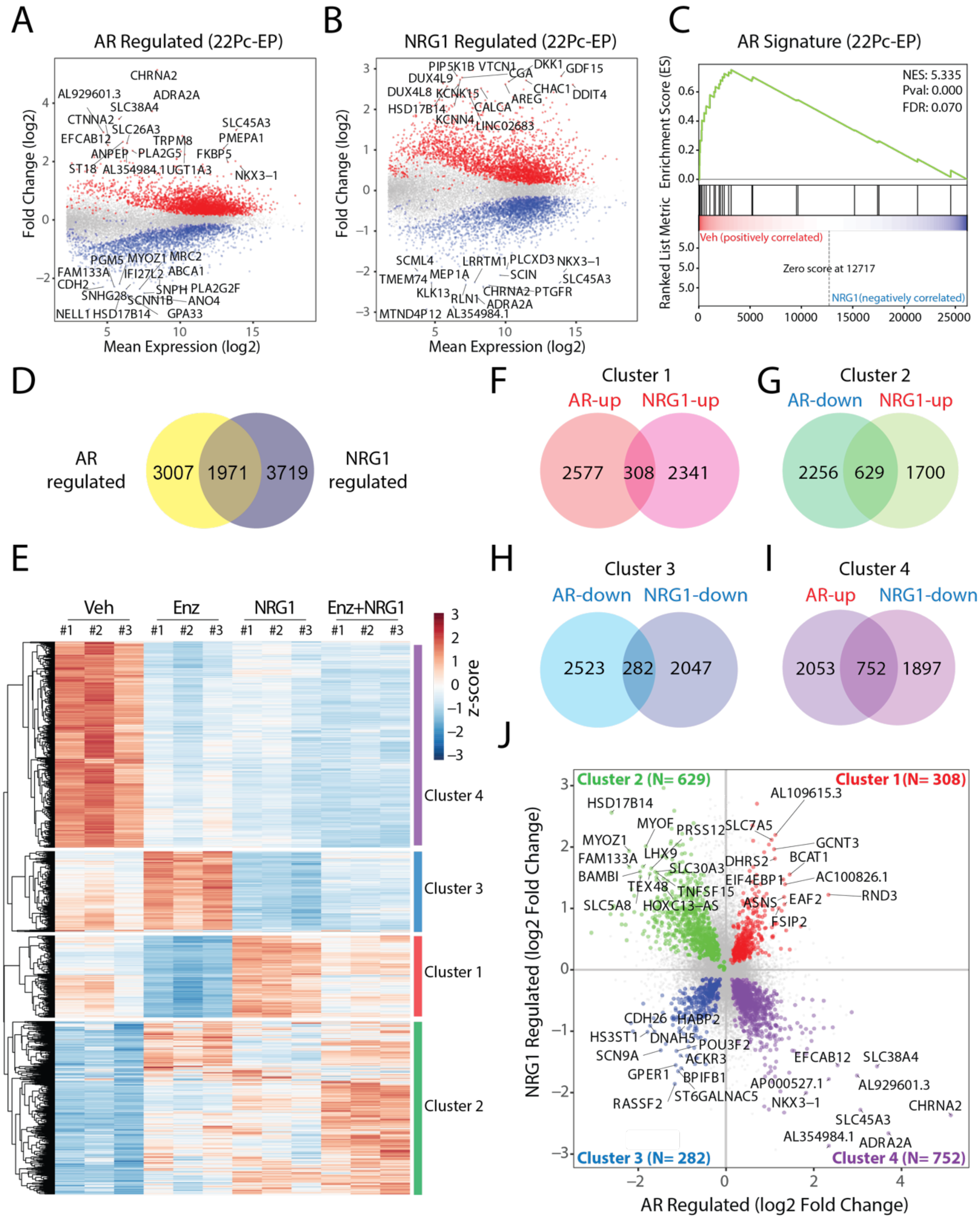

Figure 15 Part 1

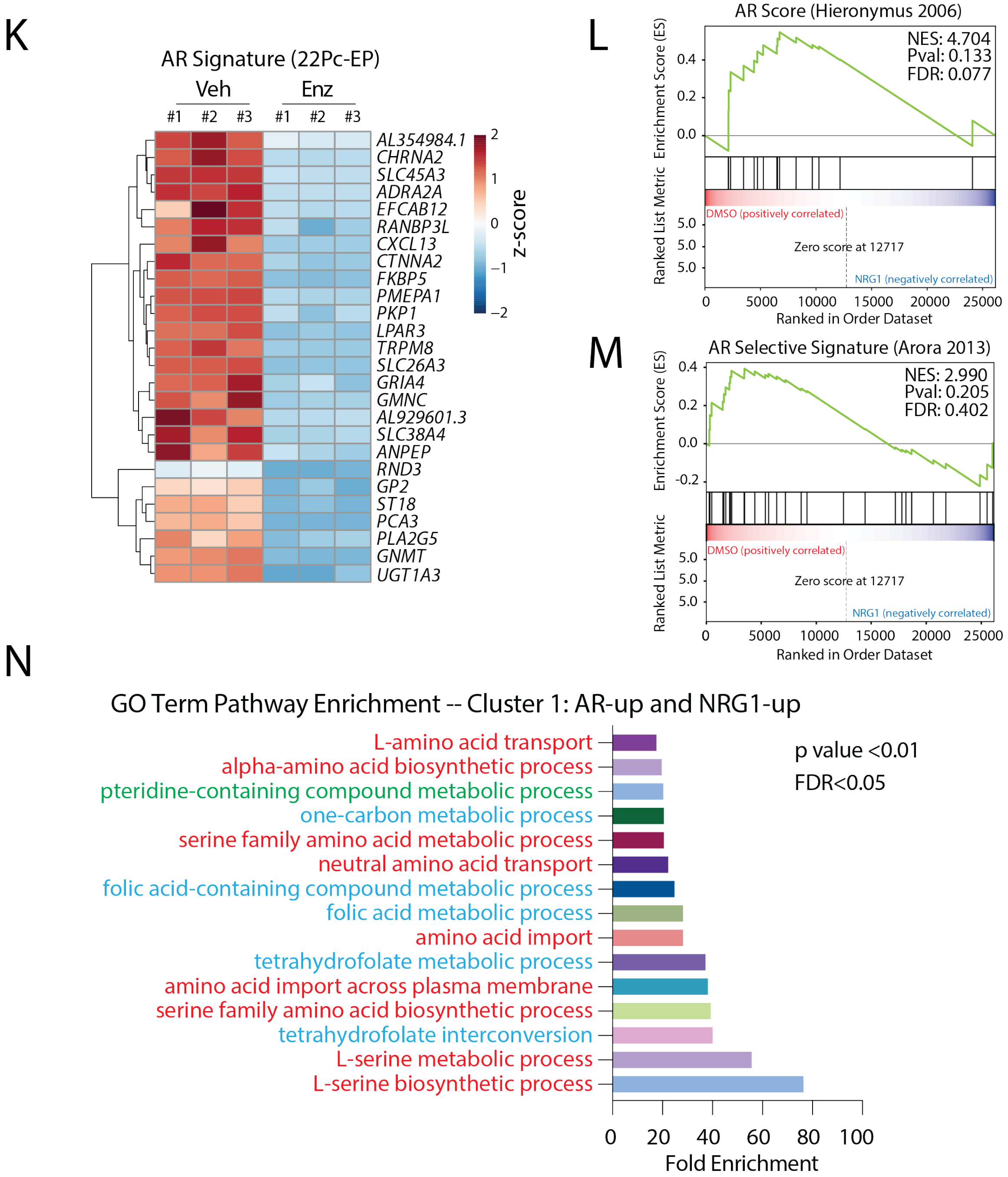

Figure 15 Part 2

**Figure 15. NRG1 activates a subset of AR target genes.**
(A) MA plot showing differential expressed genes (n=4978, adjusted p value<0.05) in 22Pc-EP cells treated with Enz (0.5µM, 48 h) or Veh (DMSO). Top 15 up- or down-regulated genes were labeled. Canonical AR targets FKBP5 and NKX3-1 were also labeled. (B) MA plot showing differential expressed genes (n=5690, adjusted p value<0.05) in 22Pc-EP cells treated with recombinant NRG1 (10ng/mL, 48 h) or Veh (PBS). Top 15 up- or down-regulated genes were labeled. (C) GSEA of AR signature between Veh (DMSO)- versus NRG1-treated group in 22Pc-EP cells. (D) Venn diagram showing the number of overlapping genes that are co-regulated by both AR and NRG1 (n=1971, adjusted p value<0.05). (E) Heatmap showing unsupervised clustering of expression of 1971 genes across 4 conditions (Veh, Enz, NRG1 or Enz+NRG1). Four distinct clusters were identified (clusters 1-4), each representing AR and NRG1 co-regulated genes in the same or opposite directions. (F-I) Venn diagram showing the number of AR and NRG1 co-regulated genes (adjusted p value<0.05 for both conditions) in each direction (clusters 1-4). Cluster 1 (F, n=308), cluster 2 (G, n=629), cluster 3 (H, n=282) and cluster 4 (I, n=752). (J) Dot plot showing fold change values (log2) of genes in each of clusters 1-4. In clusters 1,3, genes with log2 fold change > 1 were labeled. In clusters 2,4, genes with log2 fold change > 1.5 were labeled. (K) Heatmap showing expression of individual genes (n=26) that consists of the AR signature in 22Pc-EP. AR signature genes were identified as Enz suppressed genes by comparing vehicle (Veh) to Enz condition (adjusted p value<0.05, log2 fold change>2). (L) GSEA of AR score (Hieronymus et al., 2006) between DMSO versus NRG1-treated group in 22Pc-EP cells. (M) GSEA of AR selective signature (Arora et al., 2013) between DMSO versus NRG1-treated group in 22Pc-EP cells. (N) GO term analysis of top enriched pathways in cluster 1 (n=103 genes as input list, adjusted p value<0.05, log2 fold change>0.5).

# CHAPTER 4

## *4.1 Introduction*

In chapter 2, we validated NRG1's function across multiple in vitro and in vivo models. In chapter 3 we worked out molecular mechanisms of how NRG1 promotes resistance to cancer cells. In this chapter, we will finally test if NRG1 or its signaling activity has direct clinical relevance to patients receiving hormone therapy. Because in prostate tumor, NRG1 expression is dominantly contributed from the stroma, directly comparing NRG1 expression using public available database is not accurate as so far, most tumor sequencing efforts are tumor-cell centric. Therefore, we take two different approaches to validate the clinical relevance of our findings. We first developed a clinical-grade NRG1 immunohistochemistry assay which enables us to directly assess NRG1 expression in a cohort of patients undergone a neoadjuvant androgen deprivation trial. We second utilized two different NRG1 signature as a surrogate of NRG1 activity and analyze how does NRG1 activity correlate with patient treatment outcomes.

## *4.2 Higher NRG1 positivity rate in androgen deprivation treated patients*

To gain insight into the potential clinical relevance of these findings, we examined NRG1 expression in a cohort of 43 patients with localized prostate cancer who underwent radical prostatectomy surgery, 23 of whom received neoadjuvant androgen deprivation therapy (ADT) (Table 1,2). For this analysis we developed an immunohistochemical (IHC) assay to detect NRG1 expression in formalin-fixed tissue, including tissue microarrays, as described in methods (Figure 16A). Using this assay we detected NRG1 staining in 5 of 23 patients (22%) who received ADT prior to prostatectomy and in 0 of 20 patients who were hormonally intact at the time of surgery ($p = 0.0265$) (Figure 16; Table 3,4). NRG1 staining was observed in stromal cells in 4 of the 5 positive cases. The fifth case had NRG1-positive tumor cells, and one case had evidence of NRG-1 positivity in both tumor and stroma. We suspect the failure to detect NRG1 expression by IHC in the stroma of hormonally intact patients, despite clear evidence of NRG1 expression at the RNA level by RNA-FISH and RNA-PCR is due to reduced sensitivity of the IHC assay (Figure 16C). Direct comparisons of both assays across a larger cohort are warranted.

### *4.3 Patient-derived CAF promotes antiandrogen resistance through NRG1*

To further address the question of stromal-derived NRG1 expression in clinical samples, we generated primary CAFs from five PCa patients with high-risk, localized disease who underwent radical prostatectomy surgery, as described in methods. As expected, these patient-derived CAFs express PDGFRα, FAP (canonical CAF markers), vimentin and α-SMA (stromal lineage). Notably, all five patient-derived CAF cultures (pCAFs) expressed NRG1 protein (Figure 17A). Furthermore, conditioned media from each pCAF culture activated HER3/AKT phosphorylation and promoted resistance to CSS or Enz in 22Pc-EP cells, which was efficiently blocked using NRG1 neutralizing antibody (YW538.24.71) or HER3 blocking antibody (AMG888) (Figure 17B-E). To determine if pCAFs can promote in vivo tumor growth, we co-injected human pCAF isolate #1 (selected based on high NRG1 expression) with human VCaP prostate cancer cells in the xenograft assay. Co-injection of pCAF#1 cells significantly enhanced the growth of VCaP tumors in castrated mice, and this acceleration in growth was completely reversed by treatment with NRG1 blocking antibody (Figure 17F).

### *4.4 NRG1 activity associated with inferior treatment outcome*

To determine whether NRG1 influences response to antiandrogen therapy, we took advantage of a recently published cohort of genomically annotated CRPC patients with associated treatment response data to next-generation antiandrogens. Tissue samples from these patients are not available for in situ measures of NRG1 expression; therefore, we used a previously reported NRG1 activity gene signature derived by ex vivo exposure of breast cancer cells to NRG1 (*93*). First we validated that NRG1 mRNA expression (by RNA-seq) is positively correlated with the NRG1 activity score in two prostate cancer cohorts (TCGA and SU2C, representing localized and metastatic disease respectively) (Figure18A,B). The NRG1 activity score also correlated with a CAF signature score, consistent with stroma as the likely source of NRG1 (Figure18C,D). Using the NRG1 signature score, we then asked whether elevated NRG1 activity in patients is associated with clinical response to next-generation antiandrogen therapy in a cohort of 56 CRPC patients previously treated with enzalutamide or abiraterone on whom tumor RNA-seq data were available within 30 days prior to treatment (2 out of 56 were excluded due to NRG1 signature < 0). Pearson correlation analysis showed that NRG1 signature score is negatively correlated with time on treatment (p=0.005) (Figure 18E). To further dissect this correlation, we plotted the NRG1 activity score of each patient, which revealed a Gaussian-like distribution, then subdivided the cohort into upper and lower halves using the median (Figure18F). Patients in the upper half had a significantly shorter time to progression on either enzalutamide or abiraterone compared to the patients in the lower half (p=0.034) (Figure18G). This result is further supported by Cox hazards ratio analysis showing significantly reduced hazards related to a low NRG1 signature score (Figure18I). This negative correlation was also seen using a second NRG1 activity signature derived by ex vivo treatment of 22Pc-EP prostate cancer cells (p=0.036) (Figure18H). Finally, GSEA of the NRG1 activity-high vs -low patients revealed enrichment of signatures for RTK and PI3K signaling and reduced hormone receptor signaling (Figure18J-L).

### *4.5 Summary*

Through our initial IHC analysis with a limited number of patients, we observed a significant trend that patients have a higher NRG1 positivity rate upon receiving androgen deprivation therapy. In the metastatic cancer cohort, patients with a higher NRG1 activity also tend to have a statistically inferior response whose disease also relapse faster. Further analysis requires a larger cohort of both primary and metastatic patients that received androgen deprivation therapy or second-generation antiandrogens. Analysis in future single-cell RNA-seq data in clinical specimens will also give us a more accurate answer in terms of how spatial and temporal expression patterns of NRG1 will affect patient response to second-generation antiandrogens.

Finally, we proposed our working model (Figure1). In the normal tumor microenvironment, stromal cells such as CAFs express and secreted NRG1 at a low level, which maintains the baseline HER3-PI3K activity in the tumors (top). In a hormone therapy treated tumor microenvironment, secretion of NRG1 by CAFs is up-regulated, which protects tumor cells that are undergone an AR-signaling attack and therefore provides an alternative survival mechanism to them (middle). Therefore, making tumor cells less sensitive to hormone deprivation or antiandrogen attack. Importantly, this mechanism of tumor cell persistence can be reverted by blocking either NRG1 from the CAF side or NRG1 from the tumor side. Thus providing a targetable strategy for those tumors that receive elevated NRG1 signaling in response to hormone therapy. We will discuss its clinical implications in the DISCUSSION session.

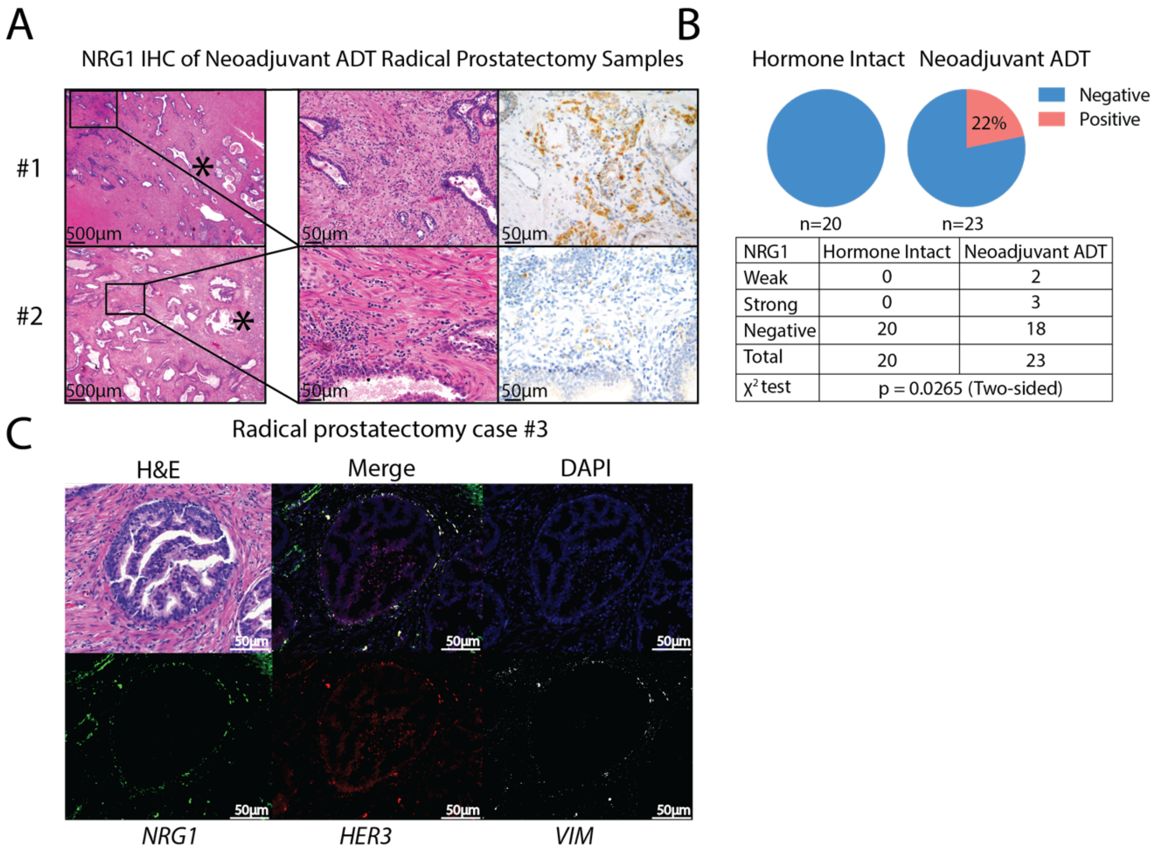

| NRG1 | Hormone Intact | Neoadjuvant ADT |
|---|---|---|
| Weak | 0 | 2 |
| Strong | 0 | 3 |
| Negative | 20 | 18 |
| Total | 20 | 23 |
| $\chi^2$ test | p = 0.0265 (Two-sided) | |

**Figure 16. Androgen deprivation therapy induces NRG1 expression in the stroma of prostate cancer patients.**

(A) Representative images showing H&E and immunohistochemistry analysis of stromal NRG1 staining in radical prostatectomy specimens from high-grade primary PCa patients. Left: 4x H&E images showing both tumor and stroma. Asterisk denotes areas of intraductal carcinoma (#1) or invasive cancer (#2). Middle: 20x H&E images. Right: 20x IHC images showing strong and diffuse NRG1 stromal staining (#1) or weak and patchy NRG1 stromal staining (#2). (B) Top: Pie chart showing percentage of NRG1 positivity in hormone intact or neoadjuvant ADT treated groups. Bottom: Table showing number of patients with NRG1 positive biopsies in hormone intact or neoadjuvant ADT treated group. (C) RNA-FISH analysis of *NRG1* (green), *HER3* (red) and *VIM* (white) expression in a high-grade prostate intraductal carcinoma case (Blue: DAPI).

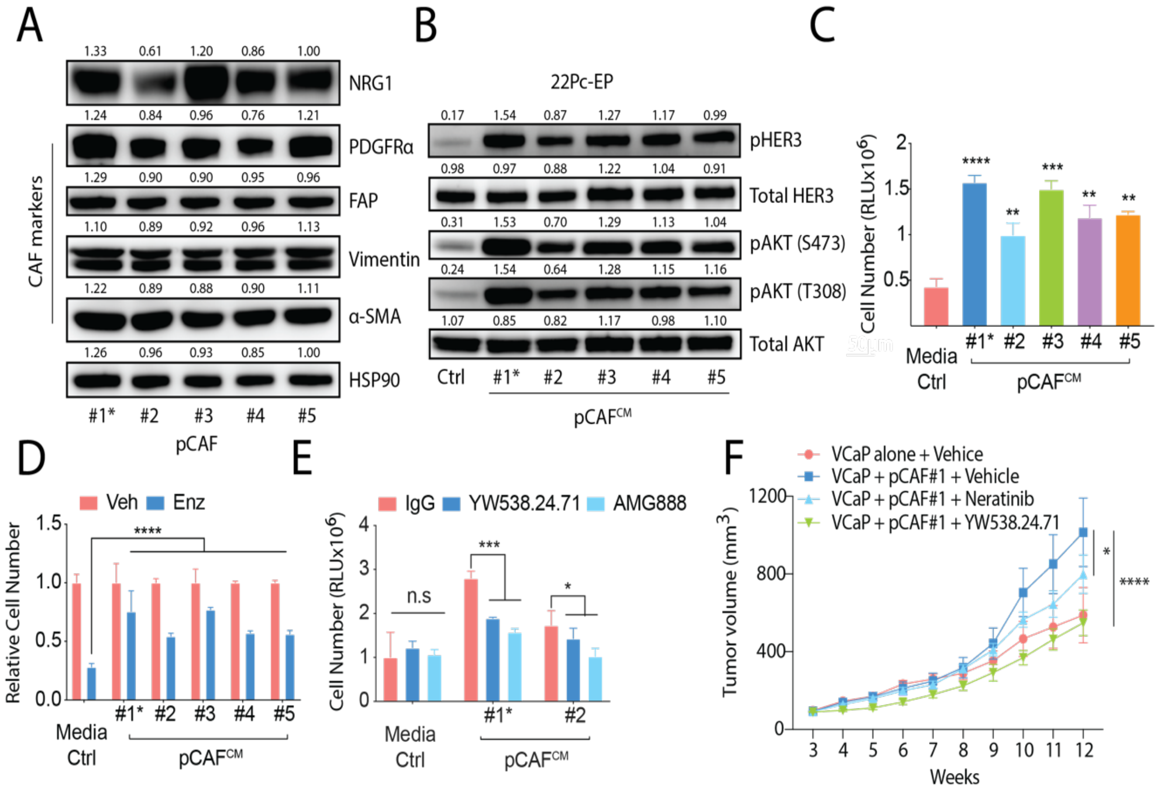

**Figure 17. Patient-derived CAFs (pCAF) promote antiandrogen resistance through NRG1-HER3.**

(A) Western blot analysis of NRG1 and CAF markers (PDGFRα, FAP, vimentin and α-SMA) in 5 independent patient-derived primary PCa CAFs (pCAFs). pCAF #1 is from a neoadjuvant ADT-treated patient and pCAFs #2-5 are from hormone intact patients. HSP90 serves as loading control. Bands were quantified using ImageJ and normalized to mean of HSP90 intensity in each group. (B) Western blot analysis of HER3-AKT activation in 22Pc-EP cells stimulated with conditioned media from patient-derived primary CAFs (pCAF$^{CM}$). Total AKT serves as loading control. Bands were quantified using ImageJ and normalized to mean of total AKT intensity in each group. (C) Growth of 22Pc-EP cells in CSS media supplemented with pCAF$^{CM}$. CellTiter-Glo reading on day 4. Media Ctrl: serum free media. (D) Growth of 22Pc-EP cells in FBS media supplemented with pCAF$^{CM}$ and are treated with Enz (0.1μM). Enz group was normalized to Veh group. CellTiter-Glo reading on day 7. Media Ctrl: serum free media. (E) Growth of 22Pc-EP cells in CSS media supplemented with pCAF$^{CM}$ treated with YW538.24.71 (10μg/mL) or AMG888 (10μg/mL). CellTiter-Glo reading on day 4. Media Ctrl: serum free media. (F) Growth of VCaP or VCaP + pCAF#1 co-injected tumor xenografts in castrated mice treated with YW538.24.71 (25mg/kg), neratinib (20mg/kg) or vehicle. Treatment started when tumors reached 200mm$^3$ (n=5 mice per group). (****p<0.0001, ***p<0.001, *p<0.05, n.s: not significant, D-E: one-way ANOVA compared to Ctrl group, error bar represents ±SD, F: Student's t-test, error bar represents ±SEM)

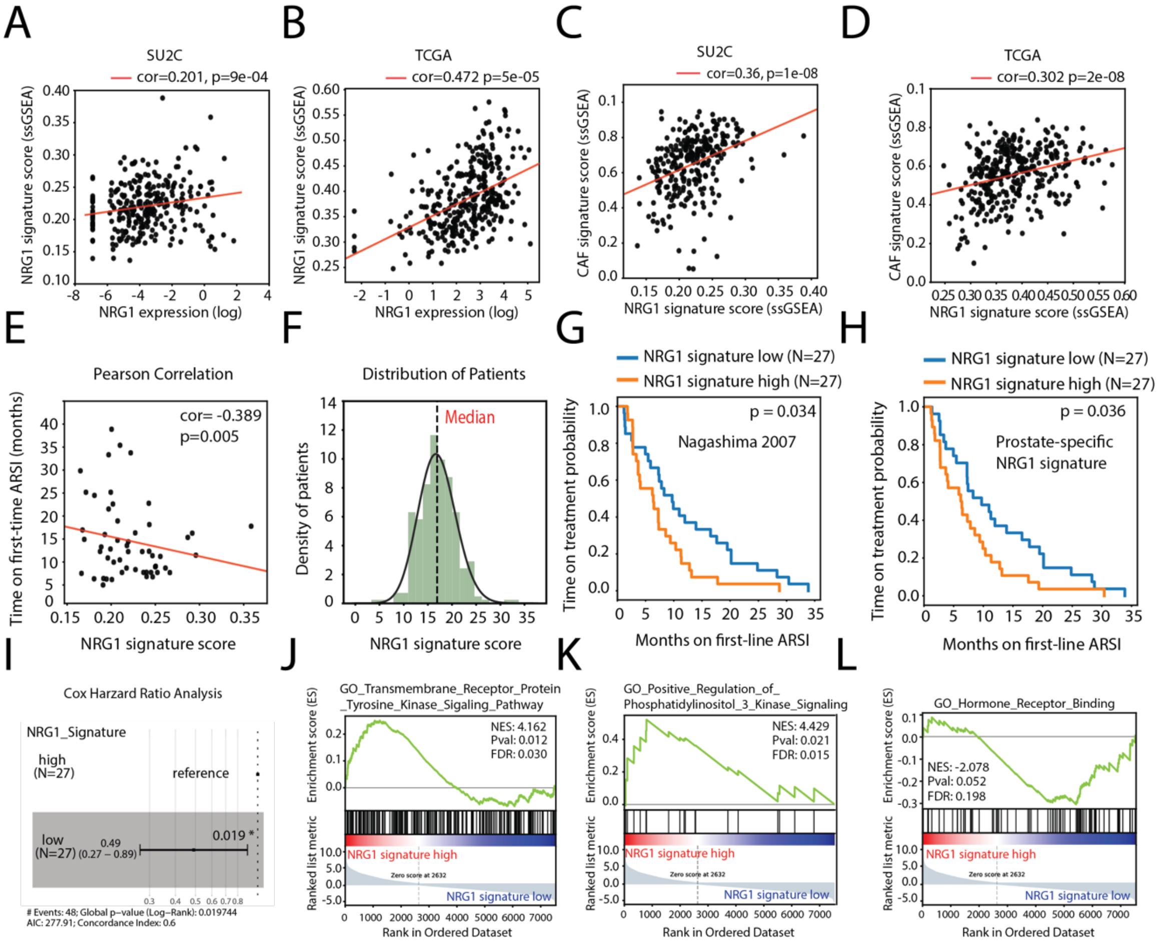

**Figure 18. NRG1 activity is associated with unfavorable treatment outcome in CRPC patients.**

(A) Pearson correlation analysis of NRG1 expression versus NRG1 signature score in SU2C cohort (p value=9x10$^{-4}$). (B) Pearson correlation analysis of NRG1 expression versus NRG1 signature score in TCGA cohort (p value=5x10$^{-5}$). (C) Pearson correlation analysis of NRG1 signature score versus CAF signature score (2) in SU2C cohort (p value=1x10$^{-8}$). (D) Pearson correlation analysis of NRG1 signature score versus CAF signature score (2) in TCGA cohort (p value=2x10$^{-8}$). (E) Pearson correlation analysis of NRG1 signature score versus time on treatment for first line androgen receptor signaling inhibitors (ARSI) of a 54 mCRPC patient cohort (p value =0.005). (F) Histogram showing frequency distribution of NRG1 signature score in the same patient cohort. Dotted line denotes median cutoff. (G) Probability of treatment duration of the high and low (median separation) groups of 54 patients, p value (0.034) was calculated using log-rank test. (H) Probability of treatment duration of the high and low (median separation) groups of 54 patients, p value (0.036) was calculated using log-rank test. (I) Cox hazard ratio analysis of the NRG1 signature score -high and -low groups of 54 patients, p-value (0.019) was calculated using log-rank test. (J) GSEA showing Transmembrane Receptor Protein Tyrosine Signaling signature between NRG1 signature -high versus -low groups (median separation). (K) GSEA showing Positive Regulation of Phosphatidylinostitol-3 Kinase signature between NRG1 signature -high versus -low groups (median separation). (L) GSEA showing Hormone Receptor Binding signature between NRG1 signature -high versus -low groups (median separation).

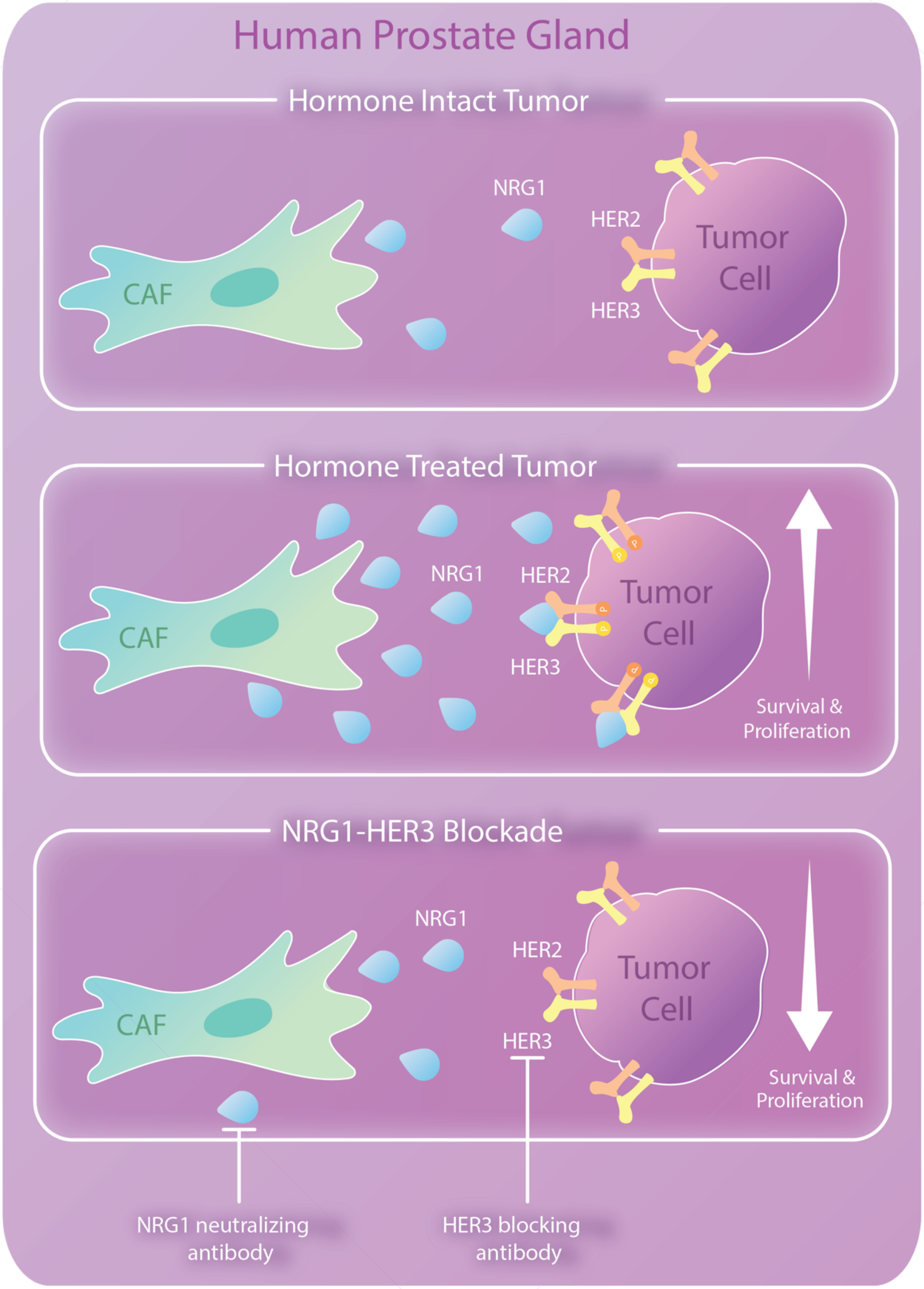

Figure 19. Summary schematic diagram

**Table 1. Baseline characteristics in evaluated patients**

| Characteristic | Neoadjuvant ADT # (n = 23) | Hormone intact (n = 20) |
|---|---|---|
| Age at diagnosis – years | | |
| Median | 58 | 64 |
| Range | 42-70 | 44-78 |
| Gleason score – n (%) | | |
| 7 | 5 (22) | 8 (40) |
| 8 | 4 (17) | 3 (15) |
| 9 | 13 (57) | 7 (35) |
| 10 | 1 (4) | 0 (0) |
| PSA at diagnosis – ng/mL | | |
| Median | 5.8 | 7.0 |
| Range | 1.29-69.9 | 1.5-20.0 |
| Neoadjuvant treatment – n (%) | | |
| ADT-only | 6 (26) | n/a |
| ADT plus bicalutamide | 2 (9) | n/a |
| ADT plus chemotherapy * | 2 (9) | n/a |
| ADT plus ARSI | | n/a |
| Enzalutamide | 4 (17) | n/a |
| Abiraterone | 6 (26) | n/a |
| Abiraterone plus enzalutamide | 3 (13) | n/a |
| Time on neoadjuvant treatment prior to prostatectomy - days | | |
| Median | 166 | n/a |
| Range | 92-1038 | n/a |

# Neoadjuvant ADT includes patients who had ADT mean± Abiraterone mean± Enzalutamide prior to radical prostatectomy; IHC: immunohistochemistry; ADT: androgen-deprivation therapy; * 2 patients had docetaxel plus carboplatin concomitant to ADT; n/a: not applicable

**Table 2. Treatment characteristics and NRG1 expression in patients exposed to neoadjuvant ADT [#]**

| | Neoadjuvant treatment | | IHC for NRG1 | |
|---|---|---|---|---|
| Patient # | Type | Duration (days) | Intensity | Localization |
| 1 | ADT | 1 dose | Negative | N/A |
| 2 | ADT | 1 dose | Negative | N/A |
| 3 | ADT | 1 dose | Negative | N/A |
| 4 | ADT, bicalutamide | 680 | Negative | N/A |
| 5 | ADT, chemotherapy | 120 | Negative | N/A |
| 6 | ADT, bicalutamide | 277 | Negative | N/A |
| 7 | ADT, abiraterone | 313 | Negative | N/A |
| 8 | ADT, enzalutamide | 363 | Negative | N/A |
| 9 | ADT, chemotherapy | 792 | Negative | N/A |
| 10 | ADT, abiraterone | 1038 | Negative | N/A |
| 11 | ADT, abiraterone | 185 | Negative | N/A |
| 12 | ADT | 1 dose | Negative | N/A |
| 13 | ADT | 1 dose | Weak | Stroma, Focal |
| 14 | ADT | 1 dose | Weak | Stroma, Focal |
| 15 | ADT, enzalutamide | 117 | Negative | N/A |
| 16 | ADT, abiraterone | 325 | Negative | N/A |
| 17 | ADT, abiraterone | 111 | Negative | N/A |
| 18 | ADT, abiraterone | 124 | Negative | N/A |
| 19 | ADT, abiraterone, enzalutamide | 171 | Negative | N/A |
| 20 | ADT, abiraterone, enzalutamide | 166 | Negative | N/A |
| 21 | ADT, Enzalutamide | 167 | Positive | Stroma |
| 22 | ADT, Enzalutamide | 225 | Positive | Tumor |
| 23 | ADT, abiraterone, enzalutamide | 113 | Positive | Tumor and Stroma |

[#] Neoadjuvant ADT includes patients who had ADT mean± Abiraterone mean± Enzalutamide prior to radical prostatectomy; ADT: androgen deprivation therapy; IHC: Immunohistochemistry

**Table 3. Characteristics of NRG1 expression in patients exposed to neoadjuvant ADT#**

| Intensity – n (%) | Neoadjuvant ADT # | Hormone intact |
|---|---|---|
| Negative | 17 (74) | 20 (100) |
| Equivocal | 1 (4) | 0 (0) |
| Weakly positive | 2 (9) | 0 (0) |
| Positive | 3 (13) | 0 (0) |
| Localization – n (%) | | |
| Negative | 17 (74) | n/a |
| Tumor only | 1 (4) | n/a |
| Stroma only | 3 (13) | n/a |
| Tumor and stroma | 1 (4) | n/a |

# Neoadjuvant ADT includes patients who had ADT mean± Abiraterone mean± Enzalutamide prior to radical prostatectomy

**Table 4. Comparison of NRG1 expression between neoadjuvant ADT-exposed and hormone intact patients.**

**Two-way Contingency Table**

| | Neoadjuvant ADT # (n = 23) | Hormone intact (n = 20) | *P* * |
|---|---|---|---|
| NRG1 expression | | | 0.0265 |
| Negative | 18 (78) | 20 (100) | |
| Positive | 5 (22) | 0 (0) | |

# Neoadjuvant ADT includes patients who had ADT mean± Abiraterone mean± Enzalutamide prior to radical prostatectomy; * Chi-squared test.
$\chi^2 = 4.920$, df = 1, $\chi^2/df = 4.92$, $P(\chi^2 > 4.920) = 0.0265$

# DISCUSSION

Studies of resistance to antiandrogen therapy in prostate cancer have primarily focused on cell-autonomous mechanisms that collectively point to the central role of sustained AR signaling, even in late-stage CRPC. These include well-documented mechanisms such as AR gene amplification/mutation and AR splice variants (*7*), as well as tandem duplication events involving the AR enhancer (*35, 99, 100*). Collectively these mechanisms may explain up to ~80% of CRPC cases, but there is growing evidence for microenvironmental sources as additional contributors to antiandrogen resistance. Immune cells, specifically myeloid-derived suppressor cells, are one such source and can drive CRPC progression through the production of the cytokine IL-23 (*56*). Stromal-derived growth factors have also been implicated, specifically HGF and FGFs (*101-103*). Here we document a critical role of NRG1, also stromal-derived, together with its receptor HER3, and we provide a clear strategy toward targeted intervention using clinical-grade blocking antibodies.

A unique feature of our work is the discovery of NRG1 through an unbiased biochemical fractionation approach in which we screened for the antiandrogen resistance factor produced by murine CAFs that persist during in vitro culture of the CWR22PC prostate cancer cell line. Specifically, we show that CAF-derived NRG1 is required for CWR22PC tumor cells to develop resistance to enzalutamide or to ADT. Mechanistic studies using multiple cell lines (VCaP, LAPC4, 22Rv1), mouse and human cancer organoids (P53-KO, RB-KO, PTENΔ/Δ -Rosa26-ERG, MSKPCa2) and in vivo xenograft models (CWR22Pc, VCaP) establish the importance of NRG1-HER3 kinase signaling as a critical driver of antiandrogen resistance. Furthermore, we observed significant antitumor activity, including tumor regressions, using clinical-grade neutralizing antibodies against NRG1 and HER3, as well as HER2-specific kinase inhibitors. In primary prostate cancer clinical samples, we show that NRG1 is synthesized by adjacent stromal cells (by RNA-FISH), with evidence (by IHC) that these levels are higher in patients who received neoadjuvant ADT. This finding is consistent with the activation of HER3 observed in a subset of patients who underwent prostatectomy after neoadjuvant ADT (*98*). We also observed elevated NRG1 mRNA expression in both mouse and patient-derived primary cancer-associated fibroblasts when they are given antiandrogen treatments in culture, suggesting AR signaling negatively regulates NRG1 expression through mechanisms that need further investigation. Importantly, in a cohort of genomically profiled CRPC patients with associated treatment response data, we found that patients with higher NRG1 activity develop resistance earlier than those with lower NRG1 activity. The collective evidence suggests that NRG1 expression in prostate stromal cells (which are AR-positive) is upregulated in patients receiving neoadjuvant ADT and, through activation of HER3 signaling in tumor cells, may contribute to their persistence. We also have evidence, through single-cell analysis of normal prostate tissue, that stromal-derived NRG1 can function as a survival factor for luminal cells independent of AR activation (Karthaus et al, in press). Of note, AR has been implicated in CAF biology in another mesenchymal tissue, dermal fibroblasts, where its loss results in CAF activation (*104*).

The fact that NRG1 protects tumor cells from androgen withdrawal without full restoration of downstream AR signaling is intriguing in light of our earlier work documenting links between receptor tyrosine kinases and AR activation (*97*). In that context, impaired AR pathway activation is seen in tumor cells with PTEN loss due to increased PI3K signaling, which results in reduced HER2/HER3 expression through downstream transcriptional effects. The effects of NRG1 activation reported here occur in wild type PTEN models where baseline PI3K activity is low but potently activated by NRG1 through HER2/HER3. We postulate that this hyperactivated PI3K signal contributes to reduced AR activity. However, we also identify a set of genes co-regulated by NRG1 and AR (and not previously recognized as AR targets) implicated in amino acid and folate metabolism that warrant further functional investigation.

In addition to the role of paracrine NRG1 production described here in prostate cancer, there is growing evidence that autocrine NRG1 expression plays a role in other tumor types. NRG1 is specifically implicated as a driver in squamous cancers (e.g., esophageal or squamous lung cancer) through its role as a direct target gene of the basal epithelial lineage defining transcription factor TP63 (*105*). More commonly, autocrine secretion of NRG1 has been observed in various cancers including ovarian, non-small cell lung, melanoma as well as brain metastasis (*53, 71-73, 106*). Among the most compelling are translocations that fuse the NRG1 genomic locus to a transcriptionally active gene partner, as seen in invasive mucinous adenocarcinomas of the lung and other tumor types. Furthermore, dramatic responses have been reported in such patients after receiving afatinib or anti-HER3 blocking antibody therapy (*107-111*).

As to whether the clinical success of anti-HER2/3 therapy in tumors with NRG1 might translate to prostate cancer, it is worth noting that prior clinical trials of HER2 inhibitors in prostate cancer were disappointing (*112-118*). However, these studies lacked current insights into which patient population is most likely to benefit and were not specifically designed to test the hypothesis raised here. Furthermore, the HER2 therapies tested in these trials are not optimal for blocking NRG1-mediated activation of HER3/4, as is now clear from more recent studies (*72, 108*). The insights emerging from our work suggest a different translational strategy. Wild-type PTEN status could be a patient selection biomarker, based on the mutual exclusivity of elevated NRG1 and PTEN mutant tumors (data not shown), which is interesting in light of a similar mutual exclusivity between NRG1 translocations and KRAS mutation in pancreas cancer (*109, 110*). In the neoadjuvant setting, one can envision combination therapy with ADT plus anti-HER3 antibody in patients with elevated NRG1 and/or phospho-HER3 levels after a short trial of ADT alone. Finally, it is worth noting that clinical trials of HER3-targeted antibody drug conjugates such as U3-1402 have shown clinical activity (*119*).

# BIBLIOGRAPHY

1. A. Dagvadorj *et al.*, Androgen-regulated and highly tumorigenic human prostate cancer cell line established from a transplantable primary CWR22 tumor. *Clin Cancer Res* **14**, 6062-6072 (2008).
2. S. Tyekucheva *et al.*, Stromal and epithelial transcriptional map of initiation progression and metastatic potential of human prostate cancer. *Nat Commun* **8**, 420 (2017).
3. R. L. Siegel, K. D. Miller, A. Jemal, Cancer statistics, 2020. *CA Cancer J Clin* **70**, 7-30 (2020).
4. F. W. Huang *et al.*, Exome Sequencing of African-American Prostate Cancer Reveals Loss-of-Function ERF Mutations. *Cancer Discov* **7**, 973-983 (2017).
5. J. Li *et al.*, A genomic and epigenomic atlas of prostate cancer in Asian populations. *Nature* **580**, 93-99 (2020).
6. P. Rawla, Epidemiology of Prostate Cancer. *World J Oncol* **10**, 63-89 (2019).
7. P. A. Watson, V. K. Arora, C. L. Sawyers, Emerging mechanisms of resistance to androgen receptor inhibitors in prostate cancer. *Nat Rev Cancer* **15**, 701-711 (2015).
8. P. Verze, T. Cai, S. Lorenzetti, The role of the prostate in male fertility, health and disease. *Nat Rev Urol* **13**, 379-386 (2016).
9. G. R. Cunha *et al.*, Development of the human prostate. *Differentiation* **103**, 24-45 (2018).
10. G. H. Henry *et al.*, A Cellular Anatomy of the Normal Adult Human Prostate and Prostatic Urethra. *Cell Rep* **25**, 3530-3542 e3535 (2018).
11. R. Bhatia-Gaur *et al.*, Roles for Nkx3.1 in prostate development and cancer. *Genes Dev* **13**, 966-977 (1999).
12. N. Gao *et al.*, Forkhead box A1 regulates prostate ductal morphogenesis and promotes epithelial cell maturation. *Development* **132**, 3431-3443 (2005).
13. G. Wang, D. Zhao, D. J. Spring, R. A. DePinho, Genetics and biology of prostate cancer. *Genes Dev* **32**, 1105-1140 (2018).
14. C. W. Chua *et al.*, Single luminal epithelial progenitors can generate prostate organoids in culture. *Nat Cell Biol* **16**, 951-961, 951-954 (2014).
15. D. Gao *et al.*, Organoid cultures derived from patients with advanced prostate cancer. *Cell* **159**, 176-187 (2014).
16. W. R. Karthaus *et al.*, Identification of multipotent luminal progenitor cells in human prostate organoid cultures. *Cell* **159**, 163-175 (2014).
17. K. Ellwood-Yen *et al.*, Myc-driven murine prostate cancer shares molecular features with human prostate tumors. *Cancer Cell* **4**, 223-238 (2003).
18. S. Y. Ku *et al.*, Rb1 and Trp53 cooperate to suppress prostate cancer lineage plasticity, metastasis, and antiandrogen resistance. *Science* **355**, 78-83 (2017).
19. M. Zou *et al.*, Transdifferentiation as a Mechanism of Treatment Resistance in a Mouse Model of Castration-Resistant Prostate Cancer. *Cancer Discov* **7**, 736-749 (2017).
20. J. Leibold *et al.*, Somatic Tissue Engineering in Mouse Models Reveals an Actionable Role for WNT Pathway Alterations in Prostate Cancer Metastasis. *Cancer Discov* **10**, 1038-1057 (2020).
21. N. Cancer Genome Atlas Research, The Molecular Taxonomy of Primary Prostate Cancer. *Cell* **163**, 1011-1025 (2015).
22. D. Robinson *et al.*, Integrative Clinical Genomics of Advanced Prostate Cancer. *Cell* **162**, 454 (2015).
23. M. Blattner *et al.*, SPOP Mutation Drives Prostate Tumorigenesis In Vivo through Coordinate Regulation of PI3K/mTOR and AR Signaling. *Cancer Cell* **31**, 436-451 (2017).
24. J. Armenia *et al.*, The long tail of oncogenic drivers in prostate cancer. *Nat Genet* **50**, 645-651 (2018).
25. G. Boysen *et al.*, SPOP-Mutated/CHD1-Deleted Lethal Prostate Cancer and Abiraterone Sensitivity. *Clin Cancer Res* **24**, 5585-5593 (2018).
26. D. Zhao *et al.*, Synthetic essentiality of chromatin remodelling factor CHD1 in PTEN-deficient cancer. *Nature* **542**, 484-488 (2017).

27. M. A. Augello *et al.*, CHD1 Loss Alters AR Binding at Lineage-Specific Enhancers and Modulates Distinct Transcriptional Programs to Drive Prostate Tumorigenesis. *Cancer Cell* **35**, 817-819 (2019).
28. D. Zhao *et al.*, Chromatin Regulator, CHD1, Remodels the Immunosuppressive Tumor Microenvironment in PTEN-Deficient Prostate Cancer. *Cancer Discov*, (2020).
29. P. Mu *et al.*, SOX2 promotes lineage plasticity and antiandrogen resistance in TP53- and RB1-deficient prostate cancer. *Science* **355**, 84-88 (2017).
30. W. Abida *et al.*, Genomic correlates of clinical outcome in advanced prostate cancer. *Proc Natl Acad Sci U S A* **116**, 11428-11436 (2019).
31. E. J. Adams *et al.*, FOXA1 mutations alter pioneering activity, differentiation and prostate cancer phenotypes. *Nature* **571**, 408-412 (2019).
32. S. Gao *et al.*, Forkhead domain mutations in FOXA1 drive prostate cancer progression. *Cell Res* **29**, 770-772 (2019).
33. A. Parolia *et al.*, Distinct structural classes of activating FOXA1 alterations in advanced prostate cancer. *Nature* **571**, 413-418 (2019).
34. B. Xu *et al.*, Altered chromatin recruitment by FOXA1 mutations promotes androgen independence and prostate cancer progression. *Cell Res* **29**, 773-775 (2019).
35. S. R. Viswanathan *et al.*, Structural Alterations Driving Castration-Resistant Prostate Cancer Revealed by Linked-Read Genome Sequencing. *Cell* **174**, 433-447 e419 (2018).
36. B. Haley, F. Roudnicky, Functional Genomics for Cancer Drug Target Discovery. *Cancer Cell* **38**, 31-43 (2020).
37. Z. Zhang *et al.*, Loss of CHD1 Promotes Heterogeneous Mechanisms of Resistance to AR-Targeted Therapy via Chromatin Dysregulation. *Cancer Cell* **37**, 584-598 e511 (2020).
38. K. Cotter, B. Konety, M. A. Ordonez, Contemporary Management of Prostate Cancer. *F1000Res* **5**, (2016).
39. I. D. Davis *et al.*, Enzalutamide with Standard First-Line Therapy in Metastatic Prostate Cancer. *N Engl J Med* **381**, 121-131 (2019).
40. J. de Bono *et al.*, Olaparib for Metastatic Castration-Resistant Prostate Cancer. *N Engl J Med* **382**, 2091-2102 (2020).
41. R. L. Siegel, K. D. Miller, A. Jemal, Cancer statistics, 2019. *CA Cancer J Clin* **69**, 7-34 (2019).
42. V. K. Arora *et al.*, Glucocorticoid receptor confers resistance to antiandrogens by bypassing androgen receptor blockade. *Cell* **155**, 1309-1322 (2013).
43. M. D. Balbas *et al.*, Overcoming mutation-based resistance to antiandrogens with rational drug design. *Elife* **2**, e00499 (2013).
44. N. Shah *et al.*, Regulation of the glucocorticoid receptor via a BET-dependent enhancer drives antiandrogen resistance in prostate cancer. *Elife* **6**, (2017).
45. Z. Zhang *et al.*, Loss of CHD1 Promotes Heterogeneous Mechanisms of Resistance to AR-Targeted Therapy via Chromatin Dysregulation. *Cancer Cell*, (2020).
46. S. I. Grivennikov, F. R. Greten, M. Karin, Immunity, inflammation, and cancer. *Cell* **140**, 883-899 (2010).
47. F. Klemm, J. A. Joyce, Microenvironmental regulation of therapeutic response in cancer. *Trends Cell Biol* **25**, 198-213 (2015).
48. X. H. Zhang *et al.*, Selection of bone metastasis seeds by mesenchymal signals in the primary tumor stroma. *Cell* **154**, 1060-1073 (2013).
49. Y. Crawford *et al.*, PDGF-C mediates the angiogenic and tumorigenic properties of fibroblasts associated with tumors refractory to anti-VEGF treatment. *Cancer Cell* **15**, 21-34 (2009).
50. R. Straussman *et al.*, Tumour micro-environment elicits innate resistance to RAF inhibitors through HGF secretion. *Nature* **487**, 500-504 (2012).
51. Y. Sun *et al.*, Treatment-induced damage to the tumor microenvironment promotes prostate cancer therapy resistance through WNT16B. *Nat Med* **18**, 1359-1368 (2012).
52. S. Su *et al.*, CD10(+)GPR77(+) Cancer-Associated Fibroblasts Promote Cancer Formation and Chemoresistance by Sustaining Cancer Stemness. *Cell* **172**, 841-856 e816 (2018).

53. D. P. Kodack *et al.*, The brain microenvironment mediates resistance in luminal breast cancer to PI3K inhibition through HER3 activation. *Sci Transl Med* **9**, (2017).
54. L. A. Gilbert, M. T. Hemann, DNA damage-mediated induction of a chemoresistant niche. *Cell* **143**, 355-366 (2010).
55. M. Ammirante, J. L. Luo, S. Grivennikov, S. Nedospasov, M. Karin, B-cell-derived lymphotoxin promotes castration-resistant prostate cancer. *Nature* **464**, 302-305 (2010).
56. A. Calcinotto *et al.*, IL-23 secreted by myeloid cells drives castration-resistant prostate cancer. *Nature* **559**, 363-369 (2018).
57. E. G. Bluemn *et al.*, Androgen Receptor Pathway-Independent Prostate Cancer Is Sustained through FGF Signaling. *Cancer Cell* **32**, 474-489 e476 (2017).
58. N. Erez, M. Truitt, P. Olson, S. T. Arron, D. Hanahan, Cancer-Associated Fibroblasts Are Activated in Incipient Neoplasia to Orchestrate Tumor-Promoting Inflammation in an NF-kappaB-Dependent Manner. *Cancer Cell* **17**, 135-147 (2010).
59. A. J. Trimboli *et al.*, Pten in stromal fibroblasts suppresses mammary epithelial tumours. *Nature* **461**, 1084-1091 (2009).
60. N. A. Bhowmick *et al.*, TGF-beta signaling in fibroblasts modulates the oncogenic potential of adjacent epithelia. *Science* **303**, 848-851 (2004).
61. O. E. Franco *et al.*, Altered TGF-beta signaling in a subpopulation of human stromal cells promotes prostatic carcinogenesis. *Cancer Res* **71**, 1272-1281 (2011).
62. M. A. Kiskowski *et al.*, Role for stromal heterogeneity in prostate tumorigenesis. *Cancer Res* **71**, 3459-3470 (2011).
63. D. M. Hyman *et al.*, Author Correction: HER kinase inhibition in patients with HER2- and HER3-mutant cancers. *Nature* **566**, E11-E12 (2019).
64. L. Mei, W. C. Xiong, Neuregulin 1 in neural development, synaptic plasticity and schizophrenia. *Nat Rev Neurosci* **9**, 437-452 (2008).
65. L. Mei, K. A. Nave, Neuregulin-ERBB signaling in the nervous system and neuropsychiatric diseases. *Neuron* **83**, 27-49 (2014).
66. K. Bersell, S. Arab, B. Haring, B. Kuhn, Neuregulin1/ErbB4 signaling induces cardiomyocyte proliferation and repair of heart injury. *Cell* **138**, 257-270 (2009).
67. G. D'Uva *et al.*, ERBB2 triggers mammalian heart regeneration by promoting cardiomyocyte dedifferentiation and proliferation. *Nat Cell Biol* **17**, 627-638 (2015).
68. M. Gemberling, R. Karra, A. L. Dickson, K. D. Poss, Nrg1 is an injury-induced cardiomyocyte mitogen for the endogenous heart regeneration program in zebrafish. *Elife* **4**, (2015).
69. X. Liang *et al.*, Activation of NRG1-ERBB4 signaling potentiates mesenchymal stem cell-mediated myocardial repairs following myocardial infarction. *Cell Death Dis* **6**, e1765 (2015).
70. B. D. Polizzotti *et al.*, Neuregulin stimulation of cardiomyocyte regeneration in mice and human myocardium reveals a therapeutic window. *Sci Transl Med* **7**, 281ra245 (2015).
71. Q. Sheng *et al.*, An activated ErbB3/NRG1 autocrine loop supports in vivo proliferation in ovarian cancer cells. *Cancer Cell* **17**, 298-310 (2010).
72. T. R. Wilson, D. Y. Lee, L. Berry, D. S. Shames, J. Settleman, Neuregulin-1-mediated autocrine signaling underlies sensitivity to HER2 kinase inhibitors in a subset of human cancers. *Cancer Cell* **20**, 158-172 (2011).
73. G. V. Hegde *et al.*, Blocking NRG1 and other ligand-mediated Her4 signaling enhances the magnitude and duration of the chemotherapeutic response of non-small cell lung cancer. *Sci Transl Med* **5**, 171ra118 (2013).
74. M. E. Taplin *et al.*, Intense androgen-deprivation therapy with abiraterone acetate plus leuprolide acetate in patients with localized high-risk prostate cancer: results of a randomized phase II neoadjuvant study. *J Clin Oncol* **32**, 3705-3715 (2014).
75. B. Montgomery *et al.*, Neoadjuvant Enzalutamide Prior to Prostatectomy. *Clin Cancer Res* **23**, 2169-2176 (2017).
76. W. C. Zhang *et al.*, miR-147b-mediated TCA cycle dysfunction and pseudohypoxia initiate drug tolerance to EGFR inhibitors in lung adenocarcinoma. *Nat Metab* **1**, 460-474 (2019).

77. M. P. Smith *et al.*, Inhibiting Drivers of Non-mutational Drug Tolerance Is a Salvage Strategy for Targeted Melanoma Therapy. *Cancer Cell* **29**, 270-284 (2016).
78. E. S. Antonarakis *et al.*, AR-V7 and resistance to enzalutamide and abiraterone in prostate cancer. *N Engl J Med* **371**, 1028-1038 (2014).
79. G. R. Cunha, Role of mesenchymal-epithelial interactions in normal and abnormal development of the mammary gland and prostate. *Cancer* **74**, 1030-1044 (1994).
80. G. R. Cunha, L. W. Chung, Stromal-epithelial interactions--I. Induction of prostatic phenotype in urothelium of testicular feminized (Tfm/y) mice. *J Steroid Biochem* **14**, 1317-1324 (1981).
81. A. Calon *et al.*, Stromal gene expression defines poor-prognosis subtypes in colorectal cancer. *Nat Genet* **47**, 320-329 (2015).
82. G. Finak *et al.*, Stromal gene expression predicts clinical outcome in breast cancer. *Nat Med* **14**, 518-527 (2008).
83. C. Isella *et al.*, Stromal contribution to the colorectal cancer transcriptome. *Nat Genet* **47**, 312-319 (2015).
84. C. Fellmann *et al.*, An optimized microRNA backbone for effective single-copy RNAi. *Cell Rep* **5**, 1704-1713 (2013).
85. K. A. Klein *et al.*, Progression of metastatic human prostate cancer to androgen independence in immunodeficient SCID mice. *Nat Med* **3**, 402-408 (1997).
86. Y. Chen *et al.*, ETS factors reprogram the androgen receptor cistrome and prime prostate tumorigenesis in response to PTEN loss. *Nat Med* **19**, 1023-1029 (2013).
87. A. Seluanov, A. Vaidya, V. Gorbunova, Establishing primary adult fibroblast cultures from rodents. *J Vis Exp*, (2010).
88. Y. Sharon, L. Alon, S. Glanz, C. Servais, N. Erez, Isolation of normal and cancer-associated fibroblasts from fresh tissues by Fluorescence Activated Cell Sorting (FACS). *J Vis Exp*, e4425 (2013).
89. P. LoRusso *et al.*, Phase I study of U3-1287, a fully human anti-HER3 monoclonal antibody, in patients with advanced solid tumors. *Clin Cancer Res* **19**, 3078-3087 (2013).
90. H. Hieronymus *et al.*, Gene expression signature-based chemical genomic prediction identifies a novel class of HSP90 pathway modulators. *Cancer Cell* **10**, 321-330 (2006).
91. O. Dakhova *et al.*, Global gene expression analysis of reactive stroma in prostate cancer. *Clin Cancer Res* **15**, 3979-3989 (2009).
92. S. L. Carter *et al.*, Absolute quantification of somatic DNA alterations in human cancer. *Nat Biotechnol* **30**, 413-421 (2012).
93. T. Nagashima *et al.*, Quantitative transcriptional control of ErbB receptor signaling undergoes graded to biphasic response for cell differentiation. *J Biol Chem* **282**, 4045-4056 (2007).
94. J. A. Tuxhorn *et al.*, Reactive stroma in human prostate cancer: induction of myofibroblast phenotype and extracellular matrix remodeling. *Clin Cancer Res* **8**, 2912-2923 (2002).
95. G. Ayala *et al.*, Reactive stroma as a predictor of biochemical-free recurrence in prostate cancer. *Clin Cancer Res* **9**, 4792-4801 (2003).
96. I. K. Mellinghoff *et al.*, HER2/neu kinase-dependent modulation of androgen receptor function through effects on DNA binding and stability. *Cancer Cell* **6**, 517-527 (2004).
97. B. S. Carver *et al.*, Reciprocal feedback regulation of PI3K and androgen receptor signaling in PTEN-deficient prostate cancer. *Cancer Cell* **19**, 575-586 (2011).
98. S. Gao *et al.*, ErbB2 Signaling Increases Androgen Receptor Expression in Abiraterone-Resistant Prostate Cancer. *Clin Cancer Res* **22**, 3672-3682 (2016).
99. D. Y. Takeda *et al.*, A Somatically Acquired Enhancer of the Androgen Receptor Is a Noncoding Driver in Advanced Prostate Cancer. *Cell* **174**, 422-432 e413 (2018).
100. D. A. Quigley *et al.*, Genomic Hallmarks and Structural Variation in Metastatic Prostate Cancer. *Cell* **174**, 758-769 e759 (2018).
101. P. A. Humphrey *et al.*, Hepatocyte growth factor and its receptor (c-MET) in prostatic carcinoma. *Am J Pathol* **147**, 386-396 (1995).

102. C. I. Hwang *et al.*, MET-dependent cancer invasion may be preprogrammed by early alterations of p53-regulated feedforward loop and triggered by stromal cell-derived HGF. *Cell Cycle* **10**, 3834-3840 (2011).
103. B. Kwabi-Addo, M. Ozen, M. Ittmann, The role of fibroblast growth factors and their receptors in prostate cancer. *Endocr Relat Cancer* **11**, 709-724 (2004).
104. A. Clocchiatti *et al.*, Androgen receptor functions as transcriptional repressor of cancer-associated fibroblast activation. *J Clin Invest* **128**, 5531-5548 (2018).
105. G. V. Hegde *et al.*, NRG1 is a critical regulator of differentiation in TP63-driven squamous cell carcinoma. *Elife* **8**, (2019).
106. C. Capparelli *et al.*, ErbB3 Targeting Enhances the Effects of MEK Inhibitor in Wild-Type BRAF/NRAS Melanoma. *Cancer Res* **78**, 5680-5693 (2018).
107. S. M. Dhanasekaran *et al.*, Transcriptome meta-analysis of lung cancer reveals recurrent aberrations in NRG1 and Hippo pathway genes. *Nat Commun* **5**, 5893 (2014).
108. A. Drilon *et al.*, Response to ERBB3-Directed Targeted Therapy in NRG1-Rearranged Cancers. *Cancer Discov* **8**, 686-695 (2018).
109. C. Heining *et al.*, NRG1 Fusions in KRAS Wild-Type Pancreatic Cancer. *Cancer Discov* **8**, 1087-1095 (2018).
110. M. R. Jones *et al.*, NRG1 Gene Fusions Are Recurrent, Clinically Actionable Gene Rearrangements in KRAS Wild-Type Pancreatic Ductal Adenocarcinoma. *Clin Cancer Res*, (2019).
111. S. Jonna *et al.*, Detection of NRG1 Gene Fusions in Solid Tumors. *Clin Cancer Res*, (2019).
112. M. J. Morris *et al.*, HER-2 profiling and targeting in prostate carcinoma. *Cancer* **94**, 980-986 (2002).
113. P. N. Lara, Jr. *et al.*, Trastuzumab plus docetaxel in HER-2/neu-positive prostate carcinoma: final results from the California Cancer Consortium Screening and Phase II Trial. *Cancer* **100**, 2125-2131 (2004).
114. A. Ziada *et al.*, The use of trastuzumab in the treatment of hormone refractory prostate cancer; phase II trial. *Prostate* **60**, 332-337 (2004).
115. D. B. Agus *et al.*, Efficacy and safety of single-agent pertuzumab (rhuMAb 2C4), a human epidermal growth factor receptor dimerization inhibitor, in castration-resistant prostate cancer after progression from taxane-based therapy. *J Clin Oncol* **25**, 675-681 (2007).
116. J. S. de Bono *et al.*, Open-label phase II study evaluating the efficacy and safety of two doses of pertuzumab in castrate chemotherapy-naive patients with hormone-refractory prostate cancer. *J Clin Oncol* **25**, 257-262 (2007).
117. S. S. Sridhar *et al.*, A multicenter phase II clinical trial of lapatinib (GW572016) in hormonally untreated advanced prostate cancer. *Am J Clin Oncol* **33**, 609-613 (2010).
118. Y. E. Whang *et al.*, A phase II study of lapatinib, a dual EGFR and HER-2 tyrosine kinase inhibitor, in patients with castration-resistant prostate cancer. *Urol Oncol* **31**, 82-86 (2013).
119. P. A. Janne *et al.*, Safety and preliminary antitumor activity of U3-1402: A HER3-targeted antibody drug conjugate in EGFR TKI-resistant, EGFRm NSCLC. *Journal of Clinical Oncology* **37**, 9010-9010 (2019).

# Appendix

Article

Cancer Cell

# Loss of *CHD1* Promotes Heterogeneous Mechanisms of Resistance to AR-Targeted Therapy via Chromatin Dysregulation

## Graphical Abstract

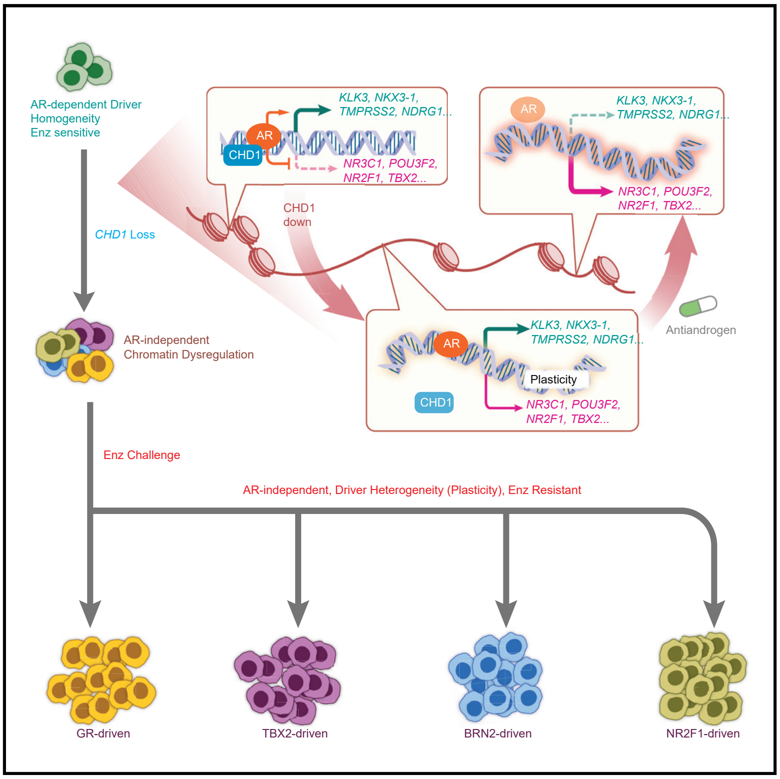

## Authors

Zeda Zhang, Chuanli Zhou,
Xiaoling Li, ..., Venkat S. Malladi,
Charles L. Sawyers, Ping Mu

## Correspondence

sawyersc@mskcc.org (C.L.S.),
ping.mu@utsouthwestern.edu (P.M.)

## In Brief

Performing an *in vivo* shRNA screen, Zhang et al. identify that *CHD1* loss confers antiandrogen resistance. Low *CHD1* levels correlate with shorter clinical responses to enzalutamide. *CHD1* loss induces global chromatin changes, increasing expression of transcription factors that contribute to antiandrogen resistance.

## Highlights

- *In vivo* screen identifies drivers of antiandrogen resistance in prostate cancer
- *CHD1* loss establishes a state of chromatin dysregulation and lineage plasticity
- Heterogeneous mechanisms were enabled to escape from luminal lineage and therapy
- Patients with reduced tumor *CHD1* levels have a shorter response to antiandrogen

Zhang et al., 2020, Cancer Cell *37*, 1–15
April 13, 2020 © 2020 Elsevier Inc.
https://doi.org/10.1016/j.ccell.2020.03.001

Please cite this article in press as: Zhang et al., Loss of *CHD1* Promotes Heterogeneous Mechanisms of Resistance to AR-Targeted Therapy via Chromatin Dysregulation, Cancer Cell (2020), https://doi.org/10.1016/j.ccell.2020.03.001

Cancer Cell
Article
CellPress

# Loss of *CHD1* Promotes Heterogeneous Mechanisms of Resistance to AR-Targeted Therapy via Chromatin Dysregulation

Zeda Zhang,[1,3,19] Chuanli Zhou,[2,19] Xiaoling Li,[2,19] Spencer D. Barnes,[4] Su Deng,[2] Elizabeth Hoover,[1] Chi-Chao Chen,[5,6] Young Sun Lee,[1] Yanxiao Zhang,[7] Choushi Wang,[2] Lauren A. Metang,[2] Chao Wu,[1] Carla Rodriguez Tirado,[2] Nickolas A. Johnson,[2] John Wongvipat,[1] Kristina Navrazhina,[6] Zhen Cao,[1,6] Danielle Choi,[1] Chun-Hao Huang,[5,6] Eliot Linton,[1] Xiaoping Chen,[8] Yupu Liang,[9] Christopher E. Mason,[10,11,12] Elisa de Stanchina,[8] Wassim Abida,[13] Amaia Lujambio,[14] Sheng Li,[15] Scott W. Lowe,[5,16] Joshua T. Mendell,[2,16] Venkat S. Malladi,[4] Charles L. Sawyers,[1,16,*] and Ping Mu[2,17,18,20,*]

[1]Human Oncology and Pathogenesis Program, Memorial Sloan Kettering Cancer Center, New York, NY 10065, USA
[2]Department of Molecular Biology, UT Southwestern Medical Center, Dallas, TX 75390, USA
[3]Louis V. Gerstner, Jr. Graduate School of Biomedical Sciences, Memorial Sloan Kettering Cancer Center, New York, NY 10065, USA
[4]Bioinformatics Core Facility of the Lyda Hill Department of Bioinformatics, UT Southwestern Medical Center, Dallas, TX 75390, USA
[5]Cancer Biology and Genetics Program, Memorial Sloan Kettering Cancer Center, New York, NY 10065, USA
[6]Weill Cornell Graduate School of Medical Sciences, New York, NY 10021, USA
[7]Ludwig Institute for Cancer Research, La Jolla, CA, USA
[8]Department of Molecular Pharmacology, Memorial Sloan Kettering Cancer Center, New York, NY 10065, USA
[9]Center for Clinical and Translational Science, Rockefeller University, New York, NY 10065, USA
[10]Department of Physiology and Biophysics, Weill Cornell Medicine, New York, NY, USA
[11]The HRH Prince Alwaleed Bin Talal Bin Abdulaziz Alsaud Institute for Computational Biomedicine, Weill Cornell Medicine, New York, NY, USA
[12]The WorldQuant Initiative for Quantitative Prediction, Weill Cornell Medicine, New York, NY, USA
[13]Department of Medicine, Memorial Sloan Kettering Cancer Center, New York, NY 10065, USA
[14]Department of Oncological Sciences, Icahn School of Medicine at Mount Sinai, New York, NY 10029, USA
[15]The Jackson Laboratory for Genomic Medicine, Farmington, CT 06032, USA
[16]Howard Hughes Medical Institute, Chevy Chase, MD 20815, USA
[17]Hamon Center for Regenerative Science and Medicine, UT Southwestern Medical Center, Dallas, TX 75390, USA
[18]Harold C. Simmons Comprehensive Cancer Center, UT Southwestern Medical Center, Dallas, TX 75390, USA
[19]These authors contributed equally
[20]Lead Contact
*Correspondence: sawyersc@mskcc.org (C.L.S.), ping.mu@utsouthwestern.edu (P.M.)
https://doi.org/10.1016/j.ccell.2020.03.001

## SUMMARY

Metastatic prostate cancer is characterized by recurrent genomic copy number alterations that are presumed to contribute to resistance to hormone therapy. We identified *CHD1* loss as a cause of antiandrogen resistance in an *in vivo* small hairpin RNA (shRNA) screen of 730 genes deleted in prostate cancer. ATAC-seq and RNA-seq analyses showed that *CHD1* loss resulted in global changes in open and closed chromatin with associated transcriptomic changes. Integrative analysis of this data, together with CRISPR-based functional screening, identified four transcription factors (NR3C1, POU3F2, NR2F1, and TBX2) that contribute to antiandrogen resistance, with associated activation of non-luminal lineage programs. Thus, *CHD1* loss results in chromatin dysregulation, thereby establishing a state of transcriptional plasticity that enables the emergence of antiandrogen resistance through heterogeneous mechanisms.

## Significance

We describe a strategy to comprehensively identify genomic loss-of-function alterations in metastatic prostate cancer through an *in vivo* shRNA library screening approach. We find that loss of *CHD1*, a commonly deleted prostate cancer gene, confers resistance to the next-generation antiandrogen enzalutamide by establishing a state of chromatin dysregulation. This altered chromatin landscape facilitates the emergence of lineage plasticity by upregulation of transcription factors that promote differentiation away from the luminal lineage. Furthermore, we find that clinical response to enzalutamide is shorter in patients whose tumors have reduced *CHD1* levels.

Please cite this article in press as: Zhang et al., Loss of *CHD1* Promotes Heterogeneous Mechanisms of Resistance to AR-Targeted Therapy via Chromatin Dysregulation, Cancer Cell (2020), https://doi.org/10.1016/j.ccell.2020.03.001

## INTRODUCTION

Targeted therapies for driver oncogenes have transformed the clinical management of many cancers but the magnitude and duration of response remains variable, even among patients with the same driver mutation and tumor histology. One potential explanation for this heterogeneity is the presence of additional genomic alterations that modify the degree of dependence on the targeted driver mutation. Metastatic prostate cancer serves as a relevant example, where the molecular target is the androgen receptor (AR) which functions as a lineage survival factor of luminal prostate epithelial cells. Next-generation AR therapies, such as abiraterone, enzalutamide, and apalutamide have significantly improved survival of men with castration-resistant prostate cancer, but resistance remains an issue (Beer et al., 2014; Ryan et al., 2013; Smith et al., 2018). Some patients fail to respond despite robust AR expression, whereas others relapse quickly.

Mechanisms of resistance to AR therapy fall into three general categories: (1) restoration of AR signaling; (2) bypass of AR signaling via other transcription factors (TFs), e.g., glucocorticoid receptor (Arora et al., 2013; Isikbay et al., 2014); and (3) AR-independent signaling (reviewed in Watson et al., 2015). One example of the latter category is combined loss of function of the *TP53* and *RB1* tumor suppressors, which confers resistance by promoting lineage transition to a state that is no longer dependent on AR and its downstream signaling pathway (Ku et al., 2017; Mu et al., 2017). Similar cases of lineage plasticity in the context of drug resistance have been documented in epidermal growth factor receptor-mutant lung adenocarcinoma and in BRAF-mutant melanoma, including transition to neuroendocrine or mesenchymal phenotypes (Garraway et al., 2005; Park et al., 2018; Sequist et al., 2011). These examples provide clear precedent for how co-occurring genomic alterations can affect response to targeted therapies. Due to the heterogeneous number of copy number alterations (Abida et al., 2017; Barbieri et al., 2012; Beltran et al., 2011, 2016; Grasso et al., 2012; Holcomb et al., 2009; Kim et al., 2007; Robinson et al., 2015; Taylor et al., 2010), we surveyed the genomic landscape of metastatic castration-resistant prostate cancer (mCRPC) for modifiers of sensitivity to AR therapy.

## RESULTS

### Enrichment of shRNAs Targeting *CHD1* in an *In Vivo* Enzalutamide Resistance Screen

To identify genomic modifiers of sensitivity to AR therapy, we constructed a pooled small hairpin RNA (shRNA) library targeting genes most frequently deleted in primary or metastatic prostate cancer, then screened for resistance to enzalutamide in a well-credentialed enzalutamide-sensitive xenograft model (Arora et al., 2013; Tran et al., 2009). The decision to conduct the screen *in vivo* was based on the fact that *in vivo* models provide a more physiologic context for studying castration-resistant growth than *in vitro* models, which rely on the use of charcoal-stripped serum to emulate castrate level of androgens. Indeed, in our hands findings from *in vivo* screens have often been confirmed in clinical datasets (Arora et al., 2013; Balbas et al., 2013).

We generated a list of 730 genes deleted in human prostate cancer (Table S1) through bioinformatic mining of 6 independent genomic datasets as described in the STAR Methods (Barbieri et al., 2012; Grasso et al., 2012; Holcomb et al., 2009; Kim et al., 2007; Network, 2015; Taylor et al., 2010). We then constructed an shRNA library targeting these genes (5–6 hairpins per gene × 730 genes = 4,234 hairpins total) using the miR-E-derived system, which has significantly improved knockdown efficiency and target specificity compared with traditional shRNA approaches (Fellmann et al., 2013) (Figure 1A; Table S2). We conducted our screen *in vivo*, using the enzalutamide-sensitive LNCaP/AR xenograft model, with the goal of identifying shRNAs enriched during enzalutamide therapy (Figure 1B). One challenge of *in vivo* screens is assurance of adequate library representation, since not all cells injected *in vivo* will contribute to the established tumors. This can be managed by limiting the number of shRNAs per injection and by dividing the library into distinct pools (Zuber et al., 2010, 2011). In a pilot experiment using the enzalutamide-resistant AR mutant (F877L) as a positive control (Balbas et al., 2013), we found that dilution of one F877L-positive cell in 100 parental LNCaP/AR cells consistently gave rise to tumors in enzalutamide-treated mice after ~6 weeks, compared with ~19 weeks for cells infected with the non-targeting control vector (shNT) (Figure S1A). Based on this result, we concluded that a pool size of 100 shRNAs should give adequate representation and therefore subdivided the library into 43 pools with ~100 shRNAs per pool. Enzalutamide functions as an agonist on the F877L mutant and may be more potent in this assay than the shRNAs to be screened; therefore, we selected 16 weeks as an optimal time to harvest tumors, before the appearance of background tumors. Each pool was screened using 10 independent injections to ensure that we could identify those shRNAs that were reproducibly enriched and eliminate those that were enriched due to stochastic clonal expansion (bystander shRNAs).

Multiple tumors emerged by 16 weeks from 40 of 43 pools screened (Figure S1B). Genomic DNA was extracted from these tumors and analyzed by next-generation sequencing to determine the enrichment of specific shRNAs compared with the starting material (Figure 1B). As expected, the abundance of most hairpins was reduced due to dilution by more rapidly expanding clones. This is apparent from comparing the normalized read counts of the starting plasmid library and pregraft populations (tightly distributed) to the tumors (broad distribution) (Figures 1C and 1D). Then we utilized a classic algorithm RIGER-E (RNAi Gene Enrichment Ranking) to rank the 730 genes based on the normalized read counts of all hairpins in both starting plasmid library/pregraft and resistant tumor populations, as described in the STAR Methods section. A p value of <0.0001 resulted in 172 genes as potential candidates (Figure 2A; Table S3). *TBC1D4* serves as a useful negative control because this gene is already deleted in an LNCaP/AR model and is ranked near the bottom, as expected (Taylor et al., 2010). Considering the potential for stochastic enrichment of biologically inert hairpins *in vivo*, we applied 2 additional filters to this list of 172 genes to enhance the probability of selecting true positives (1) enrichment in >8% of total tumors xenografted (cutoff selected based on stochastic enrichment rate of 8% for the negative control gene *TBC1D4*) (Figure 2B) and (2) enrichment of >4 independent hairpins targeting a specific gene (to avoid off-target effects) (Figure 2C). Application of these filters yielded eight candidate

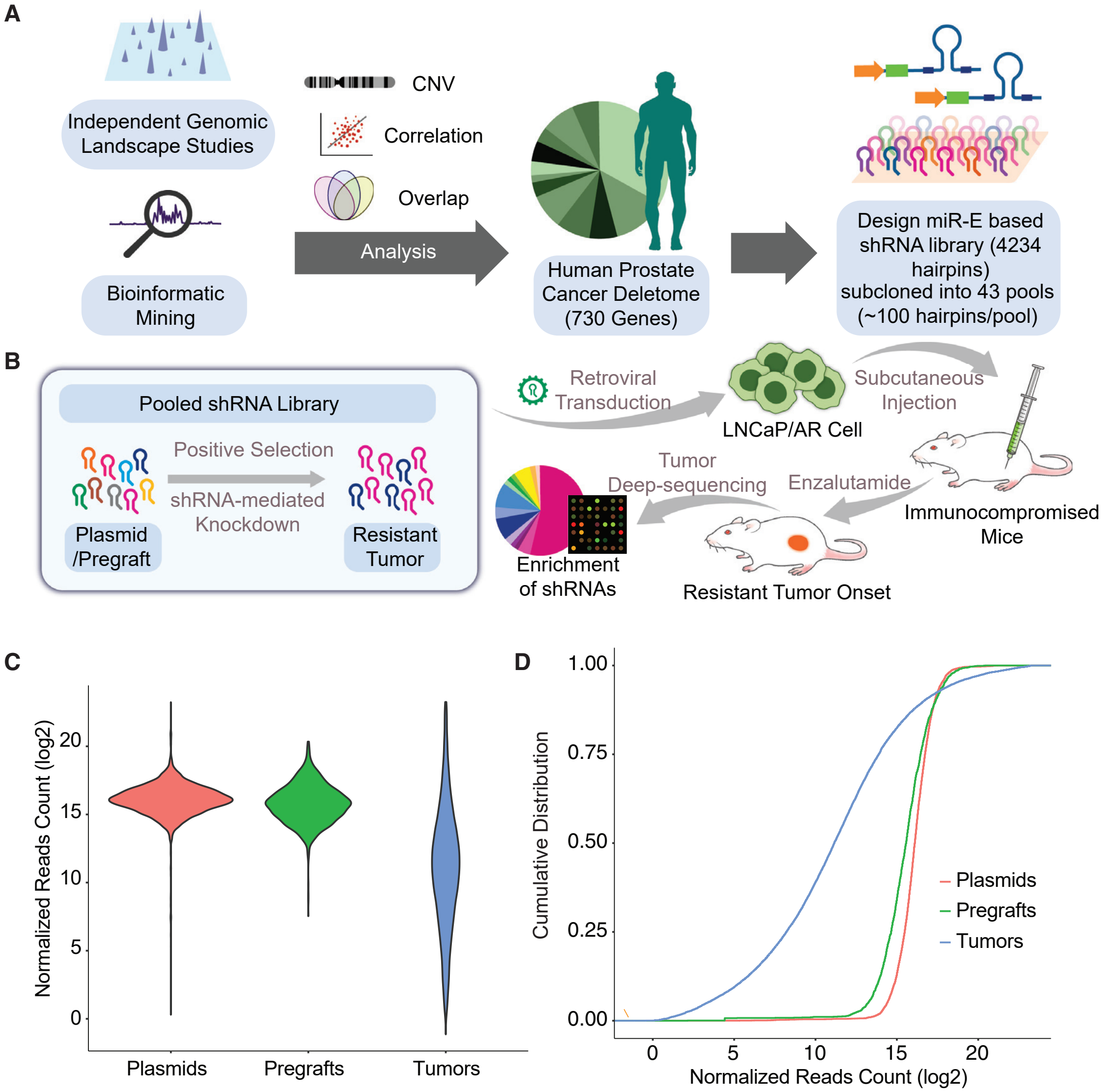

**Figure 1. An *In Vivo* shRNA Library Screen of the Human Prostate Cancer Deletome**

(A) Schematic representation of a miR-E shRNA library targeting the human prostate cancer deletome.

(B) Schematic representation of enzalutamide resistance screen using the miR-E shRNA library.

(C) Violin plot of the shRNA normalized read counts in the combined plasmid pools (n = 43), pregrafts (n = 21), and enzalutamide-resistant tumors (n = 344).

(D) Cumulative distribution of library shRNAs in the combined plasmid pools (n = 43), pregrafts (n = 21), and enzalutamide-resistant tumors (n = 344).

See also Figure S1 and Tables S1 and S2.

genes (Figure 2A; Table S3). Chromodomain helicase DNA-binding protein 1 (*CHD1*) was selected for further analysis based on its high frequency of deletion in prostate cancer (Augello et al., 2019; Grasso et al., 2012; Ren et al., 2018; Robinson et al., 2015; Rodrigues et al., 2015; Shenoy et al., 2017; Zhao et al., 2017). A representative example of *CHD1* shRNA enrichment from one of the pools is shown in Figure 2D.

## *CHD1* Loss Confers Enzalutamide Resistance *In Vitro* and *In Vivo*

In normal tissues, *CHD1* functions as a chromatin remodeler and is required to maintain the open chromatin state of pluripotent embryonic stem cells and for somatic cell reprogramming (Gaspar-Maia et al., 2009). Numerous lines of evidence from cell lines and genetically engineered mice implicate *CHD1* as a tumor suppressor, including in primary prostate cancer (Augello et al., 2019; Huang et al., 2011; Liu et al., 2012; Rodrigues et al., 2015; Shenoy et al., 2017; Zhao et al., 2017). To determine the link between *CHD1* loss and enzalutamide resistance, we performed validation experiments using five different stable shRNAs and two different CRISPR guides. *CHD1*-depleted cells consistently grew faster in enzalutamide-containing medium than *CHD1* wild-type cells, as measured in proliferation assays, dose-response assays and a fluorescence-activated cell sorting-based competition assay (Figures 3A–3D and S2A–S2D). Similar results were observed with two other next-

Please cite this article in press as: Zhang et al., Loss of *CHD1* Promotes Heterogeneous Mechanisms of Resistance to AR-Targeted Therapy via Chromatin Dysregulation, Cancer Cell (2020), https://doi.org/10.1016/j.ccell.2020.03.001

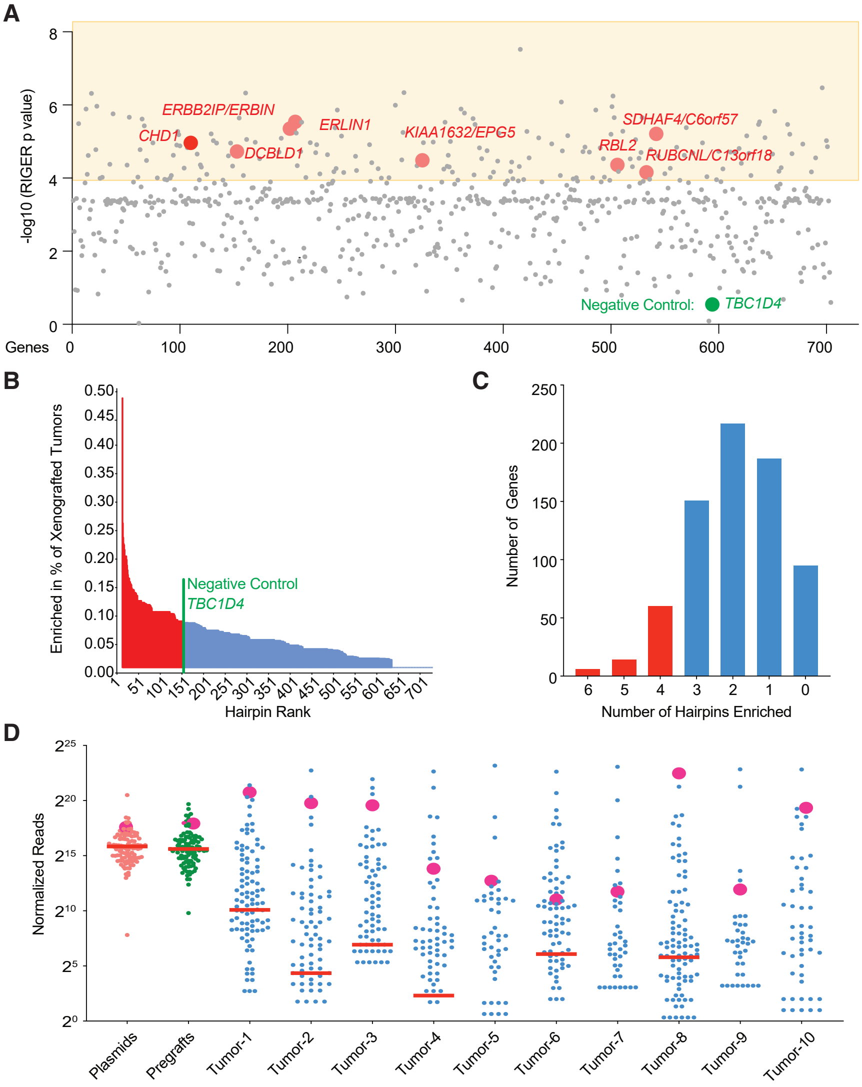

**Figure 2. *In Vivo* Screen Identifies *CHD1* as Top Candidate Responsible for Resistance to Antiandrogen**

(A) Graphical representation of analyzed results of the library screen, using RIGER-E method. –Log10 of p value is presented and the area of $p < 0.0001$ is highlighted. The top eight candidate genes are presented as large red dots with gene symbol. Negative control gene *TBC1D4* is presented as a large green dot.

(B) Graphical representation of the percentage of tumors which have shRNAs targeting a specific gene and are enriched in resistant tumors.

(C) Graphical representation of the number of genes which have multiple independent shRNAs enriched in resistant tumors.

(D) Bee swarm plot of the normalized shRNA read counts of a representative pool in the plasmid, pregraft, and resistant tumors, median is presented as a red line (medians below 1 are not presented on log2 scale). shCHD1s are presented as large red dots.

See also Table S3.

generation AR inhibitors, apalutamide and darolutamide (Figure S2D). These findings were confirmed *in vivo* in castrated mice treated with enzalutamide (Figures 3E and S2E). In addition to *CHD1*, we confirmed that knockdown of two other candidate genes (*RUBCNL* and *RBL2*) also confers enzalutamide resistance in LNCaP/AR cells cultured *in vitro* (Figure S2F). Analysis of the other five candidates will be reported separately.

Importantly, enzalutamide resistance conferred by *CHD1* knockdown was fully rescued by introducing the full-length *CHD1* cDNA (Figure S2C). Using a doxycycline-inducible shRNA knockdown model, we also confirmed that enzalutamide resistance conferred by *CHD1* knockdown is rapid and reversible (Figures S2G–S2I). *CHD1* knockdown also conferred *in vitro* resistance to enzalutamide in the human prostate cancer cell lines CWR22Pc, LAPC4, and E006AA (but only in the context of *PTEN* loss) and in a genetically defined mouse organoid model ($Pten^{-/-}$) cultured in 3D, as well as *in vivo* resistance in the CWR22Pc xenograft model (Figures S3A–S3G).

## Low *CHD1* mRNA Level Is Associated with Shorter Treatment Response in CRPC Patients

A recent mCRPC genomic landscape study with linked longitudinal clinical outcome data provided an opportunity to address whether *CHD1* loss in patients is associated with poor clinical response to next-generation antiandrogen therapy (Abida et al., 2019). Within this landscape study we identified 56 CRPC patients treated with either abiraterone or enzalutamide on whom tumor whole-exome and RNA sequencing (RNA-seq) data were available within 30 days before treatment. We initially asked if genomic *CHD1* loss was associated with treatment response but there were too few cases to run the analysis (only two with homozygous *CHD1* deletion). We therefore asked if *CHD1* mRNA expression is correlated with outcome. A Cox proportional hazards regression model was fitted on log2 (*CHD1* mRNA level) as a continuous predictor, which showed a regression coefficient of −0.39 and p value of 0.11. Although this analysis did not meet the threshold for statistical significance, it raised the possibility that lower *CHD1* mRNA levels may have higher relative hazards or, in other words, confer a higher risk to the patients. Indeed, a Pearson correlation analysis showed that *CHD1* mRNA level is significantly correlated with progression-free survival time ($p = 0.021$) (Figure 4A). To further dissect this correlation, we divided the cohort into quartiles based on the *CHD1* mRNA levels, which revealed a Gaussian-like distribution (Figure 4B). We excluded 4 of the 56 patients who had *SPOP* mutations (who were distributed evenly across the quartiles) because these patients have increased sensitivity to abiraterone (Boysen et al., 2018). Patients in the lowest quartile of tumor *CHD1* expression had a significantly shorter time to progression on either enzalutamide

Please cite this article in press as: Zhang et al., Loss of *CHD1* Promotes Heterogeneous Mechanisms of Resistance to AR-Targeted Therapy via Chromatin Dysregulation, Cancer Cell (2020), https://doi.org/10.1016/j.ccell.2020.03.001

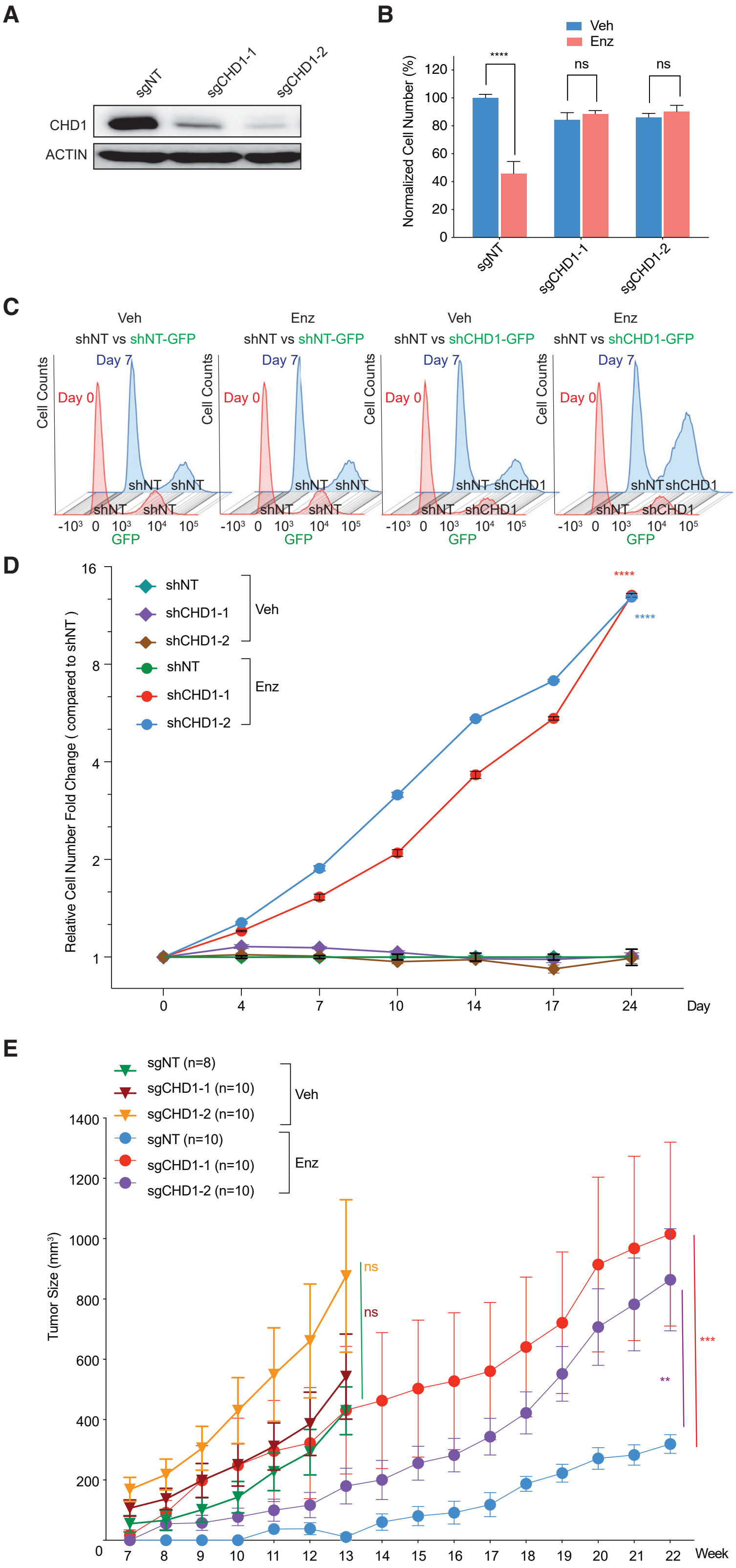

**Figure 3. *CHD1* Loss Confers Significant Resistance to Antiandrogen *In Vitro* and *In Vivo***

(A) Western blot of CHD1 in LNCaP/AR cells transduced with annotated guide RNAs.

(B) Relative cell number of LNCaP/AR cells transduced with annotated guide RNAs, normalized to sgNT + Veh group. Cells were treated with 10 μM enzalutamide (Enz) or DMSO (Veh) for 7 days and cell numbers were counted. p values were calculated using multiple t tests, three biological replicates in each group.

(C) Histograms of representative fluorescence-activated cell sorting-based competition assay showing the distribution of shNT LNCaP/AR cells (GFP-negative) compared with cells transduced with *cis*-linked shCHD1-GFP or shNT-GFP shRNAs (GFP positive). The distribution on day 0 is shown in red and day 7 is shown in blue.

(D) Relative cell number fold change compared with shNT group, based on the results of (C). Enz denotes enzalutamide of 10 μM and Veh denotes DMSO. p values were calculated using two-way ANOVA, three biological replicates in each group.

(E) Tumor growth curve of xenografted LNCaP/AR cells transduced with annotated guide RNAs. Enz denotes enzalutamide treatment at 10 mg/kg from day 1 of grafting. Veh denotes 0.5% CMC + 0.1% Tween 80.

p values were calculated using two-way ANOVA. For all panels, mean ± SEM is presented. ****$p < 0.0001$, ***$p < 0.001$, **$p < 0.01$, *$p < 0.05$. See also Figures S2 and S3.

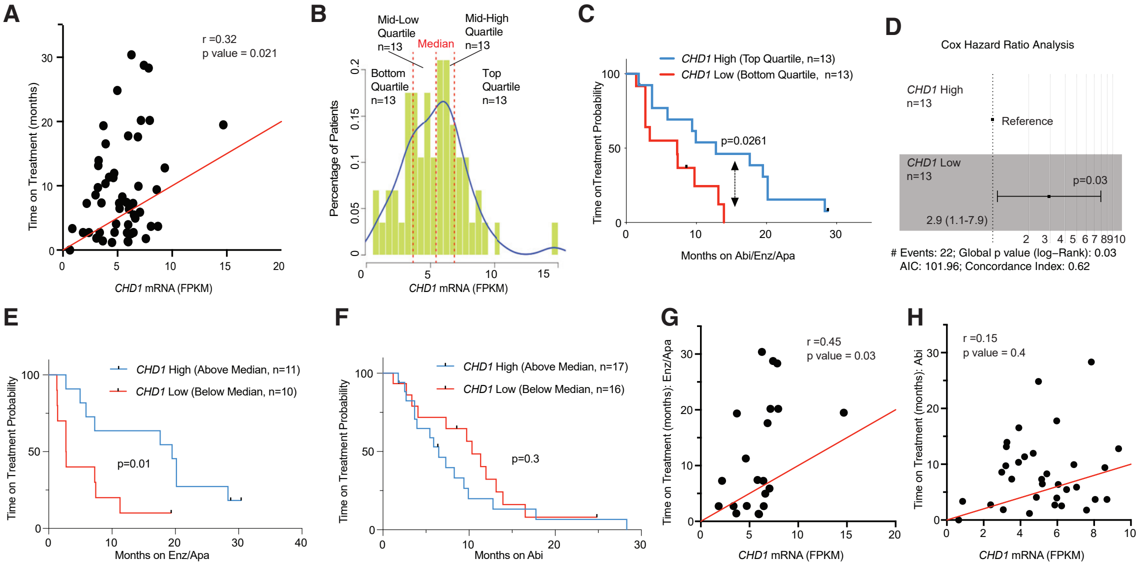

**Figure 4. *CHD1* mRNA Level Is Correlated with Clinical Outcome of Antiandrogen Treatment**

(A) Pearson correlation analysis of *CHD1* mRNA and time of treatment on abiraterone (Abi)/enzalutamide (Enz)/apalutamide (Apa) of a 52 mCRPC patient cohort.

(B) *CHD1* expression distribution in all patients of the cohort in (A).

(C) Probability of treatment duration of the top quartile compared with bottom quartile of all patients treated with abiraterone (Abi)/enzalutamide (Enz)/apalutamide (Apa); p value was calculated using Mantel-Cox test.

(D) Cox hazard ratio analysis of the top and bottom quartile of all patients, p value was calculated using log rank test.

(E) Probability of treatment duration of the above median compared with below median of patients who received enzalutamide (Enz)/apalutamide (Apa), p value was calculated using Mantel-Cox test.

(F) Probability of treatment duration of the above median compared with below median of patients who received abiraterone (Abi), p value was calculated using Mantel-Cox test.

(G) Pearson correlation analysis of *CHD1* mRNA and time of treatment on patients who received enzalutamide (Enz)/apalutamide (Apa), n = 21 (2 patients received both apalutamide and abiraterone).

(H) Pearson correlation analysis of *CHD1* mRNA and time of treatment on patients who received abiraterone (Abi), n = 33.

or abiraterone compared with the patients in the highest quartile (p = 0.0261) (Figure 4C), supporting the predictions from the preclinical findings. This finding is further supported by Cox hazards ratio analysis showing significant increased hazards related to low *CHD1* mRNA levels (Figure 4D). Interestingly, we find that the poor clinical outcome seen in patients with low *CHD1* expression is primarily seen in those treated with enzalutamide/apalutamide (Figure 4E) but not abiraterone (Figure 4F), which is confirmed by Pearson correlation analysis (Figures 4G and 4H). This distinction is consistent with our experimental data showing that *CHD1* deletion confers resistance to enzalutamide but not to androgen withdrawal in the LNCaP/AR model (as seen in charcoal-stripped serum treated with vehicle; Figures 3B, 3E, S2C, and S2D), raising the intriguing possibility of mechanistic differences in resistance to AR antagonists versus androgen-lowering agents.

## Integrated Analysis of RNA-Seq and ATAC-Seq Reveals Candidate TF Drivers of Enzalutamide Resistance

To investigate the mechanism by which *CHD1* loss promotes antiandrogen resistance, we first asked if AR signaling activity was restored in these enzalutamide-resistant tumors. To our surprise, we observed sustained inhibition of the AR target genes *KLK3*, *NKX3-1*, *TMPRSS2*, *NDRG1*, *PMEPA1*, and *STEAP1*, indicating that canonical AR signaling is not restored (Figures 5A and 5B). This suggested that *CHD1* loss might activate transcriptional programs that relieve prostate tumor cells from their dependence on AR by reprogramming away from their luminal lineage, as we have reported previously in the setting of combined loss of *RB1* and *TP53* (Ku et al., 2017; Mu et al., 2017).

Because CHD1 plays a role in chromatin remodeling, we postulated that such lineage transitions (and their underlying transcriptional programs) could be identified by integrative analysis of global transcriptional and chromatin landscape changes induced by *CHD1* loss, as measured by RNA-seq and assay for transposase-accessible chromatin sequencing (ATAC-seq). To distinguish between transcriptional changes induced by *CHD1* loss alone versus enzalutamide treatment, we profiled LNCaP/AR cells that were not exposed to enzalutamide after stable *CHD1* knockdown (shCHD1-1 and shCHD1-2; two different shRNAs) as well as enzalutamide-resistant sublines of shCHD1-1 and shCHD1-2 derived after passage as xenografts in enzalutamide-treated mice (shCHD1-XE-1 and shCHD1-XE-2). ATAC-seq revealed substantial changes in open and closed chromatin after *CHD1* loss, consistent with the function of CHD1 in chromatin remodeling. Globally, we observed more than 10,000 new open and closed peaks, mainly in the intronic and intergenic regions (Figures 5C and 5D). *CHD1* loss also led to global changes in transcriptome profiling (Figure 5E) which were associated with changes in open chromatin (Figures S4A–S4D). The transcriptome changes were relatively similar in both shCHD1 sublines but were quite divergent in the

Please cite this article in press as: Zhang et al., Loss of *CHD1* Promotes Heterogeneous Mechanisms of Resistance to AR-Targeted Therapy via Chromatin Dysregulation, Cancer Cell (2020), https://doi.org/10.1016/j.ccell.2020.03.001

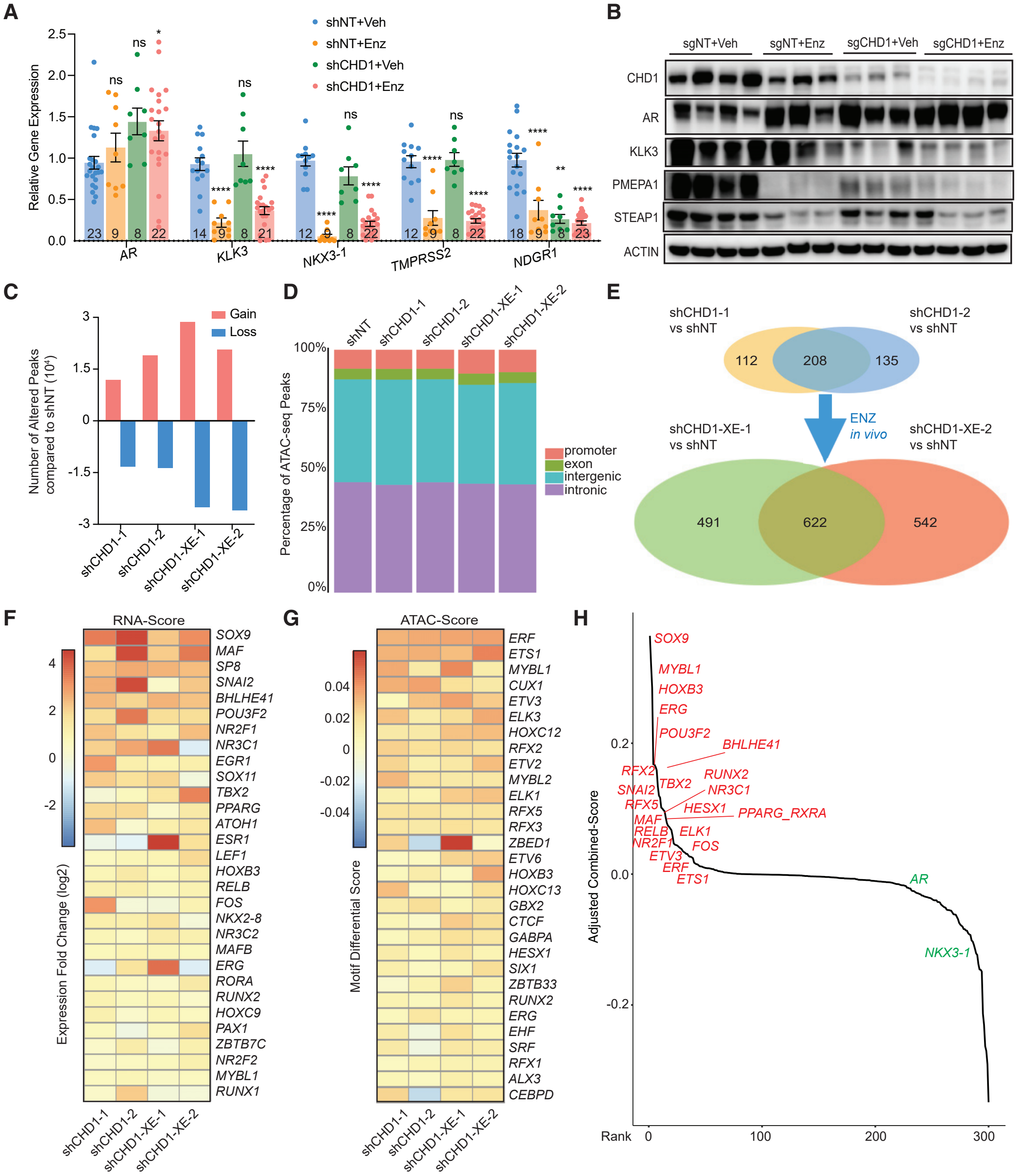

**Figure 5. Integrated Analysis of RNA-seq and ATAC-Seq Reveals Candidate Transcription Factor Drivers of Enzalutamide Resistance**

(A) Relative gene expression of AR and AR target genes in tumors collected from LNCaP/AR xenografts, all normalized and compared with shNT + Veh group. Mean ± SEM is presented. p values were calculated using two-way ANOVA and numbers of biological replicates are presented. ****$p < 0.0001$, ***$p < 0.001$, **$p < 0.01$, *$p < 0.05$.

(B) Western blot showing AR and AR targets in tumors collected from LNCaP/AR xenografts. For both (A) and (B), Enz denotes enzalutamide treatment at 10 mg/kg from day 1 of grafting. Veh denotes 0.5% CMC + 0.1% Tween 80.

(C) Graphical representation of the ATAC-seq peaks changes (gain or loss) in cell lines compared with shNT.

(D) The distribution of ATAC-seq peak locations in different genetic regions. For both (C) and (D), reads from three biological replicates were pooled to calculate the consensus peaks.

(E) Venn diagram represents the overlap of the most differentially expressed genes in four groups compared with shNT. Cutoff values of fold change greater than 2 and false discovery rate $\leq$ 0. 1 were used. Reads from three biological replicates in each group were used for analysis.

(F) Heatmap represents the expression fold changes (comparing to shNT) of the top 30 genes ranked by RNA-Score, three biological replicates in each group.

*(legend continued on next page)*

shCHD1-XE-1 and shCHD1-XE-2 sublines (Figures S5A and 5B), suggesting that enzalutamide exerts selective pressure that can result in distinct transcriptional outcomes. Interestingly, gene set enrichment analysis and pathway analysis revealed significant downregulation of AR-selective signature genes and enrichment of several neuron differentiation related pathways in shCHD1-XE tumor cell lines (Figures S5C and S5D; Table S4).

Because activation of downstream target genes is dependent on both the abundance of a TF as well as the accessibility of its cognate binding sites within chromatin, we integrated changes in TF expression with the presence of their associated binding motifs in areas of open chromatin. We first calculated an overall RNA-Score of TFs using the sum of weighted log fold change to identify those with significant changes in RNA level across all four *CHD1* loss conditions (Figure 5F). We then used motif analysis within the open peaks identified by ATAC-seq to calculate an overall ATAC-Score by summing the weighted motif differential scores derived from the DAStk tool (Figure 5G). Twenty-two TFs emerged after integration of upregulated TFs with the enriched motifs of each TF (by multiplying the overall RNA-Score and ATAC-Score), which we then evaluated as candidate drivers of enzalutamide resistance in context of *CHD1* loss (Figure 5H and Table S5).

## Functional Screen Implicates Four TFs in Mediating Enzalutamide Resistance

To explore the functional role of these 22 TFs in antiandrogen resistance, we asked if CRISPR deletion of each TF alone would restore enzalutamide sensitivity in LNCaP/AR cells with *CHD1* knockdown. Four independent guide RNAs for each of the 22 genes were individually cloned into a viral vector with a *cis*-linked RFP gene, pooled and introduced into shCHD1 cells in a manner that resulted in a mixture of RFP-positive (range ~50%–90%) and RFP-negative cells. For cells expressing guides targeting TFs required for enzalutamide resistance, we reasoned that the percentage of RFP-positive cells would decline over 7 days when cultured with enzalutamide (Figure 6A). In control cells infected with a non-targeting guide (sgNT) and in cells expressing guides targeting 18 of the 22 TFs, the fraction of RFP-positive cells did not change significantly (Figure 6B). However, RFP-positive cells were significantly depleted in cells expressing guides selectively targeting genes encoding each of four TFs: *NR3C1* (encoding GR), *POU3F2* (encoding BRN2), *TBX2*, and *NR2F1* (Figure 6B). Independent experiments confirmed that CRISPR deletion of each of these four TFs re-sensitized shCHD1 cells to enzalutamide *in vitro* (Figure 6C). Furthermore, their upregulation in the context of *CHD1* loss was reversible, as revealed by doxycycline-regulated *CHD1* shRNA knockdown (Figure 6D) and was evident in three other AR-positive human prostate cancer cell lines (Figures S6A–S6C).

Interestingly, all four TFs have been previously implicated in resistance to hormone therapy and prostate cancer progression, often in the context of aberrant lineage specification away from canonical luminal adenocarcinoma (Arora et al., 2013; Bishop et al., 2017; Du et al., 2017; Ku et al., 2017; Mu et al., 2017; Nandana et al., 2017; Shi et al., 2019; Sosa et al., 2015). To further interrogate their roles, we extended our analysis to a panel of ~20 enzalutamide-resistant xenografts, each derived independently from LNCaP/AR after *CHD1* depletion by either shRNA or CRISPR deletion. Each of the four TFs had elevated expression in some but not all xenografts across this panel, supporting a heterogeneous profile across this isogenic series of sublines (Figure 7A). *NR3C1* was most frequently and substantially upregulated, but multiple sublines also had upregulation of *NR2F1*, *TBX2*, or *POU3F2*, sometimes without concurrent *NR3C1* upregulation. Immunofluorescence and immunohistochemical staining revealed heterogeneity within the shCHD1-XE-1 cell lines and in shCHD1 tumors resistant to enzalutamide, as seen by increased levels of NR2F1 in some cells and both NR2F1 and GR in other cells (Figures S7A–S7D). Collectively, this pattern and the results from an inducible shCHD1 model suggest a state of chromatin plasticity and enhanced heterogeneity, initiated by *CHD1* loss, which enables upregulation of distinct sets of genes in response to selective pressure.

This concept is further supported by *in vitro* studies where we examined the effect of brief exposure to enzalutamide on expression of each of the four TFs in *CHD1* wild-type cells or in those with *CHD1* depletion (by shRNA or CRISPR) (Figure 7B). Either *CHD1* loss or enzalutamide exposure was sufficient to modestly upregulate each of the four TFs, but transcriptional changes were more substantial under both conditions, particularly in the *CHD1*-deleted, enzalutamide-resistant xenograft-derived cell lines (Figures 7A and 7B). This hypothesis is also supported by RNA-seq data from the previously mentioned cohort of mCRPC patients (Abida et al., 2019), in which we examined the co-association of *CHD1* levels with each of these four TFs across 212 tumors. Unsupervised clustering analysis of just these five genes identified five distinct clusters (Figure 7C). Cluster 5 (*CHD1* high) is noteworthy because the relative expression of each of the four TFs is low; whereas clusters 2, 3, and 4 (*CHD1* low) each displays relatively higher expression of *NR2F1* and *POU3F2* (cluster 3), *TBX2* (cluster 2), or *NR3C1* (cluster 4). Cluster 1 (also *CHD1* low) is an outlier to this pattern because all four TFs are also low, which could be an indication of even greater heterogeneity beyond that elicited from the LNCaP/AR model. The identity of additional plasticity drivers could emerge through characterization of transcriptional and chromatin landscape changes across other models (Alizadeh et al., 2015).

An underlying assumption of our chromatin plasticity model is that the observed changes in TF activity promote enzalutamide resistance through loss of luminal lineage identity. Indeed, we observed altered expression of many canonical lineage-specific genes in the same panel of *CHD1*-deleted, enzalutamide-resistant xenografts that displayed heterogeneous upregulation of the four TFs (Figure 7D). For example, all tumors showed consistent downregulation of luminal marker genes (*AR*, *KRT8*, and *KRT18*), some had increased levels of basal marker genes

(G) Heatmap represents the motif differential changes (compared with shNT) of the top 30 genes ranked by ATAC-Score, three biological replicates in each group.
(H) Rank of candidate transcription factors (TFs) are shown based on the adjusted Combined-Score. Top candidate TFs selected for functional CRISPR library screen are presented in red.
See also Figures S4 and S5 and Table S4.

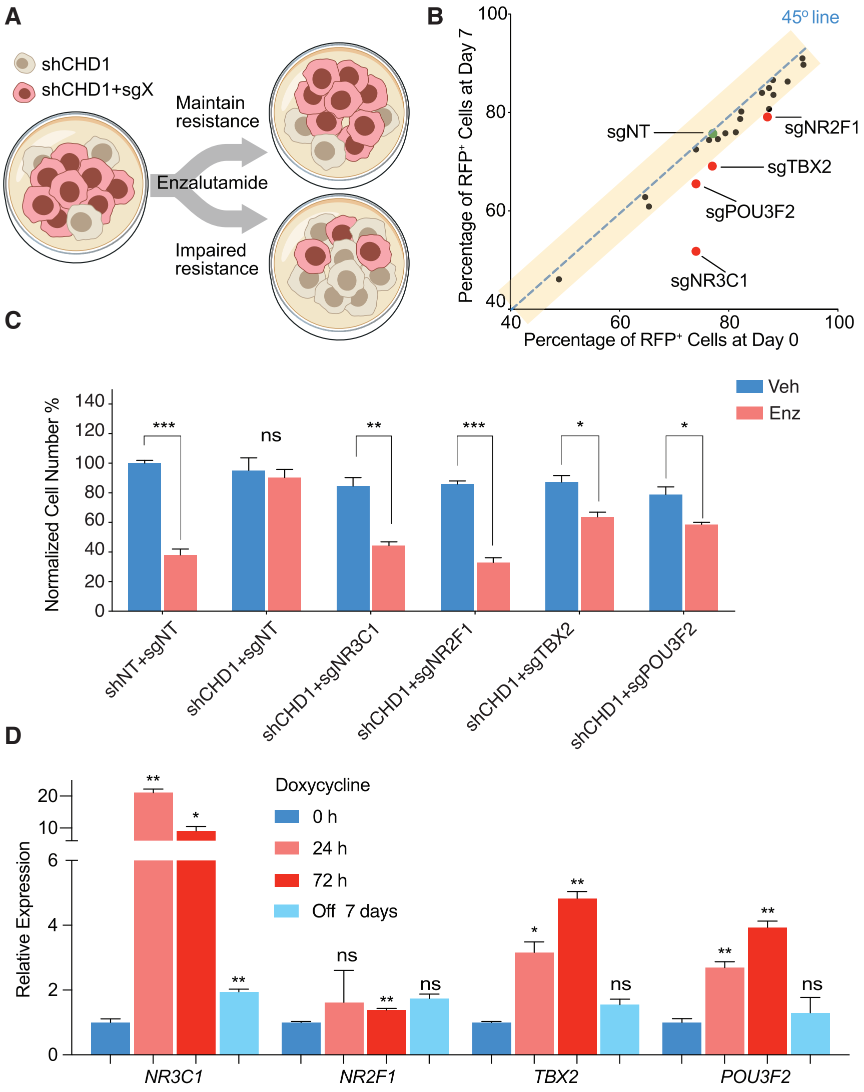

**Figure 6. Functional CRISPR Screen Identifies Four Alternative TFs as Drivers of Antiandrogen Resistance**

(A) Schematic representation of the functional CRISPR library screen in shCHD1 LNCaP/AR cells. shCHD1 cells were transduced with Cas9 and pooled single guide RNAs targeting individual TFs and achieved cell mixtures of 50%–90% RFP-positive cells (shCHD1 + sgTF) versus RFP-negative cells (shCHD1 only).

(B) Scatterplot summarizing the results of the screen. Each dot represents pooled guide RNAs targeting a specific gene. The x axis is the percentage of RFP cells at day 0 and the y axis is the percentage at day 7. The green dot identifies the sgNT control. Genes that scored positive in the screen are highlighted in red.

(C) Relative cell number of LNCaP/AR cells transduced with annotated guide RNAs, normalized to shNT + sgNT + Veh group. Cells were treated with 10 $\mu$M enzalutamide (Enz) or DMSO (Veh) for 7 days and cell numbers were counted. Mean ± SEM is presented, and p values were calculated by multiple t tests, with three biological replicates in each group.

(D) Relative gene expression level of the four TF genes in LNCaP/AR cells transduced with annotated inducible shRNAs at various time points. Mean ± SEM is presented, p values were calculated by two-way ANOVA, all compared with 0 h, with three technical replicates in each group. $^{****}p < 0.0001$, $^{***}p < 0.001$, $^{**}p < 0.01$, $^{*}p < 0.05$.

See also Figure S6 and Table S5.

(*KRT5* and *TP63*), and nearly all showed upregulation of genes, such as *SNAI2*, *TWIST1*, *SNAI1*, and *ZEB1* that specify epithelial to mesenchymal transition (EMT). Intriguingly, these changes in lineage gene expression were rapid (evident within only 48 h after doxycycline-inducible *CHD1* knockdown) and reversible (Figures S7E and S7F). Collectively, we propose that *CHD1* loss establishes an altered and plastic chromatin landscape which, in the face of stresses, such as antiandrogen therapy, enables resistant subclones to emerge through activation of alternative, non-luminal lineage programs that reduce dependence on AR.

## GR Inhibition Restores Enzalutamide Sensitivity in *CHD1*-Deficient Tumors with Increased GR Expression

Identification of GR as one of the four critical TFs upregulated by *CHD1* loss was of particular interest based on previous reports implicating GR in enzalutamide resistance (Arora et al., 2013; Isikbay et al., 2014, Li et al., 2017) and led us to reexamine the molecular basis of GR upregulation in LREX cells, a previously reported enzalutamide-resistant subline of LNCaP/AR cells (Arora et al., 2013). Remarkably, *CHD1* mRNA and protein levels were significantly lower in LREX compared with LNCaP/AR cells (Figures S8A and S8B). We also found robust upregulation of GR mRNA (*NR3C1*) and protein (Figures 8A and 8B), as well as downstream GR target genes (*SGK1* and *NPC1*), across a panel of enzalutamide-resistant xenografts after *CHD1* deletion (by shRNA or CRISPR) (Figure 8A). These findings are notable because *CHD1* loss resulted in increased GR expression without enzalutamide challenge, in contrast to previous work in *CHD1* intact models (Arora et al., 2013; Shah et al., 2017) (Figures 8A, 8B, and S8C).

To determine if sustained GR expression is required to maintain enzalutamide resistance in *CHD1*-deleted tumors with increased GR expression, we pursued both genetic and pharmacologic strategies. First, we knocked down GR in shCHD1-XE-1, the subline with the highest GR level, using two independent GR hairpins and observed substantial growth inhibition *in vitro* (Figures 8C, 8D, and S8D). For pharmacologic inhibition of GR, we turned to inhibitors of BET bromodomain proteins, which we previously reported can re-sensitize *CHD1* intact CRPC tumors with increased GR levels to enzalutamide by inhibiting GR expression (Shah et al., 2017). *In vitro* experiments using two different BET inhibitors (JQ1 and CPI-0610) confirmed that GR expression in *CHD1*-deficient cells is BET dependent (Figure S8E), similar to data in the LREX model (Arora et al., 2013; Shah et al., 2017). Interestingly, the degree of BET-dependent GR expression

Please cite this article in press as: Zhang et al., Loss of *CHD1* Promotes Heterogeneous Mechanisms of Resistance to AR-Targeted Therapy via Chromatin Dysregulation, Cancer Cell (2020), https://doi.org/10.1016/j.ccell.2020.03.001

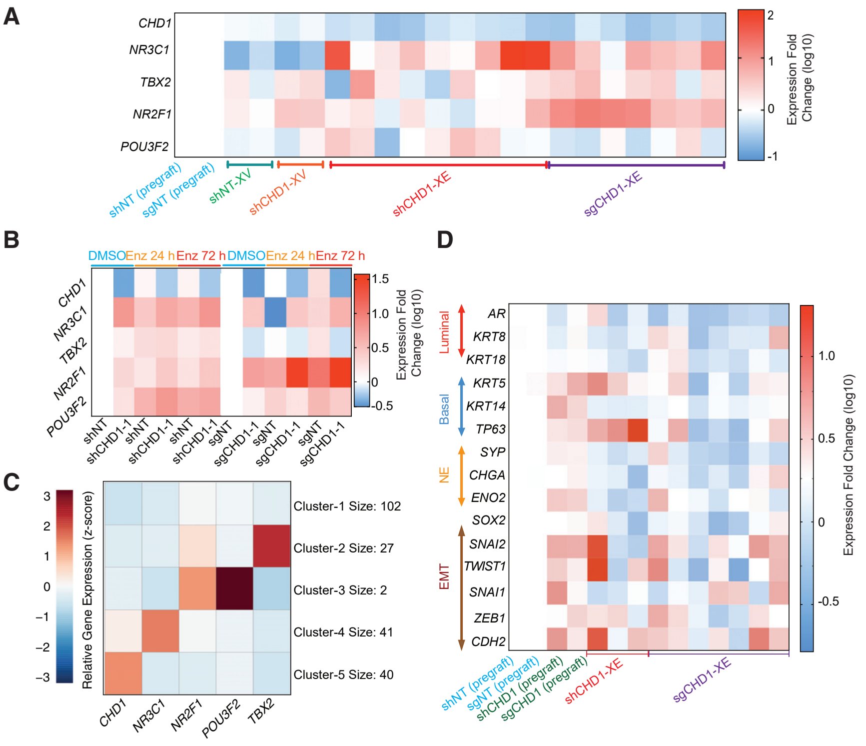

**Figure 7. *CHD1* Loss Enhanced Prostate Cancer Cell Heterogeneity and Lineage Plasticity**

(A) Heatmap represents the expression fold changes (qPCR) of the top four resistance driver genes and *CHD1* in different xenografts derived cell lines, three technical replicates for each line.

(B) Heatmap represents the expression fold changes of the top four resistant driver genes (qPCR) in shCHD1 cell line treated with 10 μM enzalutamide (Enz) in charcoal-stripped serum medium, three biological replicates for each line.

(C) Unsupervised clustering of 212 patients based on the gene expression level (*Z* score) of *CHD1* and the 4 TFs.

(D) Relative gene expression level (qPCR) of lineage-specific markers and EMT genes in selective shCHD1-XE and sgCHD1-XE cell lines, three technical replicates for each line.

See also Figure S7.

was substantially greater in *CHD1*-deficient cells that had not been previously exposed to enzalutamide (Figure S8E). For *in vivo* experiments, we used CPI-0610 due to its more favorable pharmacologic properties and observed more tumor regressions in mice treated with enzalutamide + CPI-0610 versus either drug alone (Figures S8F and S8G) (Albrecht et al., 2016).

## DISCUSSION

It is widely appreciated that the efficacy of targeted cancer therapies can be negatively affected by tumor heterogeneity, particularly in the context of concurrent genomic alterations that can mitigate dependence on the primary oncogenic driver. Cataloging these concurrent alterations in a comprehensive way could better inform patient selection for targeted therapies and provide insight into how to maximize treatment response (Alizadeh et al., 2015; Li et al., 2016). The *in vivo* shRNA library screening strategy reported here, using the next-generation antiandrogen enzalutamide in metastatic CRPC as an example, illustrates the feasibility of this approach as well as the challenges. Two critical learnings were: (1) the use of relatively small shRNA pools (~100 different hairpins) to ensure adequate representation of each hairpin and (2) the decision to perform multiple independent tumor inoculations (10 per pool). The latter decision allowed us to eliminate bystander shRNAs that are enriched solely on the basis of the stochastic growth of individual cells that can contribute disproportionately to the final composition of the tumor (sometimes called jackpot clones). The wisdom of this decision is apparent in the fact that at least three of the eight hits were validated in secondary screens. This approach mandates use of a larger number of animals, but this can be balanced by using smaller, focused libraries (such as the prostate deletome described here) instead of whole genome libraries.

A major insight from our characterization of how *CHD1* loss promotes enzalutamide resistance is the role of an altered chromatin landscape in establishing a cell state that enables more rapid adaptation to environmental stresses, such as antiandrogen therapy than can occur in *CHD1*-intact tumor cells. One consequence of this “cell state model” is the opportunity for multiple different mechanisms of resistance to arise, as illustrated by the four different TFs identified here (Figure 8E). This mechanism has parallels with work in small-cell lung cancer showing altered chromatin landscapes in primary versus metastatic tumors due to genomic amplification of the *NFIB*, which encodes a TF that promotes neuroendocrine differentiation through chromatin pioneering activity (Denny et al., 2016; Yang et al., 2018). Such epigenetic reorganization can also be observed in hematological malignancies (Hassan et al., 2017).

Although this study was focused solely on identifying enzalutamide resistance mechanisms linked to *CHD1* loss, it is remarkable that all four of the TFs identified have been previously implicated in advanced prostate cancer progression. GR is intriguing in light of previous work showing that GR upregulation is an adaptive resistance mechanism (Arora et al., 2013). Indeed, reexamination of those data, in light of these findings, suggests that loss of *CHD1* may be the mechanism of GR upregulation in these earlier models. BRN2 is similarly intriguing based on recent evidence that this neural TF drives neuroendocrine differentiation of tumor cells and thereby promotes enzalutamide resistance through loss of luminal lineage features (Bishop et al., 2017). TBX2, a T-box family TF, has been shown to induce EMT (reduced E-cadherin, increased N-cadherin) and WNT signaling, resulting in enhanced metastasis in prostate cancer models (Du et al., 2017; Nandana et al., 2017). Finally, the orphan nuclear receptor NR2F1 has been linked to tumor cell dormancy in prostate cancer through induction of pluripotency genes, such as *SOX2* and *NANOG* (Sosa et al., 2015).

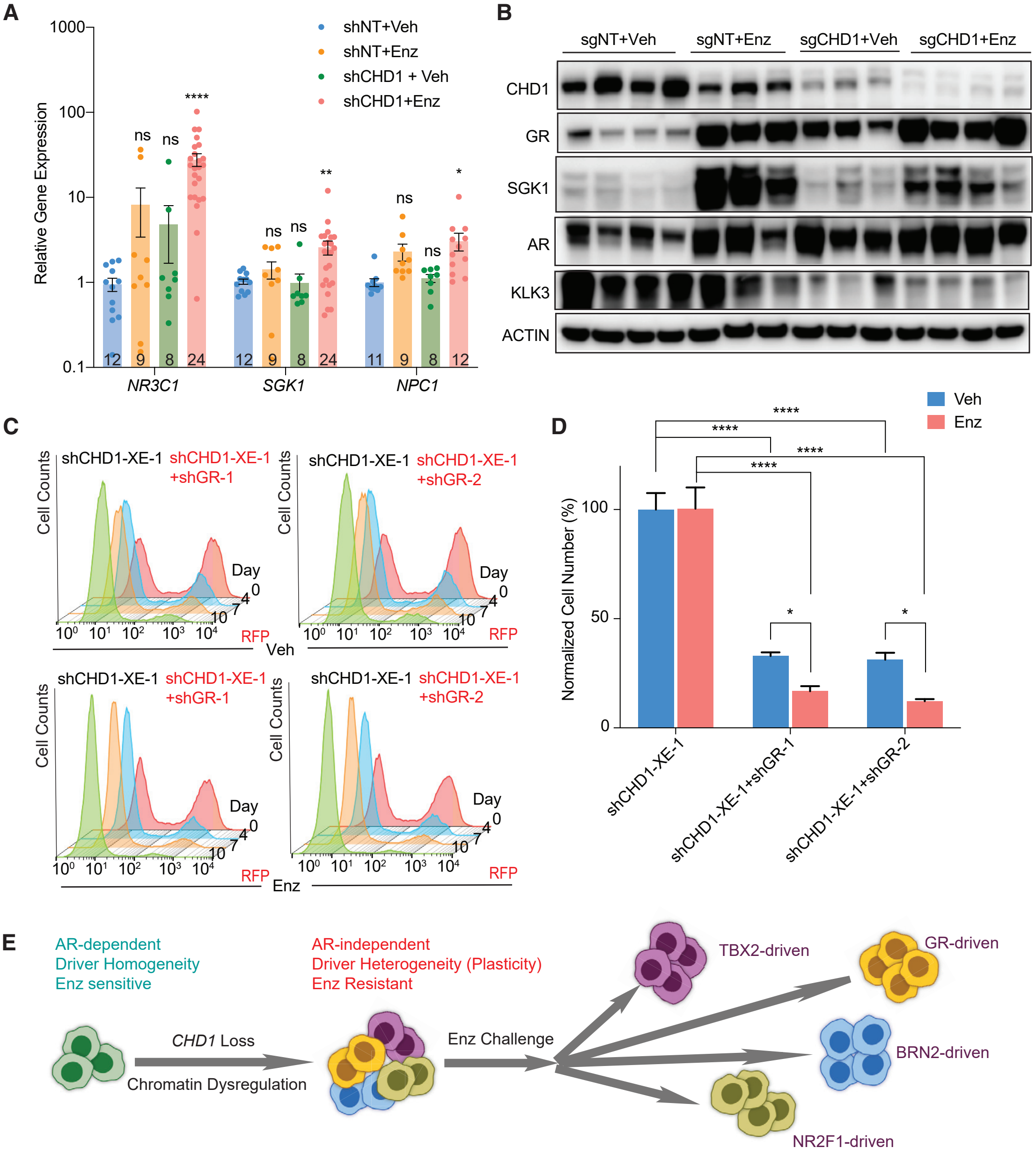

**Figure 8. GR Inhibition Has Significant Antitumor Effect on Antiandrogen-Resistant Tumors with *CHD1* Loss**

(A) Relative gene expression of *NR3C1* and GR target genes in tumors collected from LNCaP/AR xenografts, all normalized and compared with shNT + Veh group. Mean ± SEM is presented. p values were calculated using two-way ANOVA, and numbers of biological replicates are presented.

(B) Western blot showing AR, GR, and their downstream target genes in xenografted LNCaP/AR tumors. For (A) and (B), Enz denotes enzalutamide at 10 mg/kg from day 1 of grafting. Veh denotes 0.5% CMC + 0.1% Tween 80.

(C) Histograms of representative FACS-based competition assay showing the distribution of shCHD1-XE-1 cells (RFP-negative) versus shCHD1-XE-1 cells transduced with shGR (RFP-positive). The distributions on different days are presented in different colors.

(D) Relative cell number of shCHD1-XE-1 cells transduced with annotated inducible shRNAs, normalized to shCHD1-XE-1 + Veh. Cells were treated with 250 ng/mL doxycycline for 48 h, and then 7 days of 10 μM enzalutamide (Enz) or DMSO (Veh) before cell numbers were counted. Mean ± SEM is presented, and p values were calculated by two-way ANOVA, with three biological replicates in each group.

(E) Model depicting the chromatin dysregulation (plasticity) and antiandrogen resistance in mCRPC due to *CHD1* loss.

For all panels, $^{****}p < 0.0001$, $^{***}p < 0.001$, $^{**}p < 0.01$, $^{*}p < 0.05$. See also Figure S8.

Our data demonstrate that *CHD1* loss in CRPC promotes a state of intratumoral heterogeneity, but further work is needed to determine whether these heterogeneous mechanisms function independently or collaboratively. It is worth noting that pluripotency genes, such as *SOX2* have been implicated in several examples of lineage plasticity, including those mediated by

BRN2 and NR2F1, as well as in other examples, such as *RB1* and *TP53* loss (Ku et al., 2017; Mu et al., 2017; Park et al., 2018). Single-cell analysis should bring greater clarity to this heterogeneity, including the possibility that these TFs function in collaborative, hierarchical signaling networks (Goldman et al., 2019).

It is important to place our model of how *CHD1* loss promotes antiandrogen resistance mechanisms in the context of previous work on *CHD1* in prostate cancer. First, it is clear that *Chd1* deletion alone in the mouse prostate is not sufficient to induce cancer (Augello et al., 2019; Shenoy et al., 2017); however, cancers do emerge after co-deletion of *Map3k7* (Rodrigues et al., 2015) or *Pten* (Augello et al., 2019). Conversely, *CHD1* is reported to have a synthetic lethal interaction with *PTEN* in some breast and PCa models (Zhao et al., 2017), presumably due to context-specific effects. Intriguingly, *Chd1*$^{-/-}$;*Map3k7*$^{-/-}$ prostate cancers have neuroendocrine features, consistent with our observation that *CHD1* loss can promote expression of aberrant lineage programs. Chromatin immunoprecipitation sequencing studies of the *CHD1* and AR cistromes suggest a regulatory role for CHD1, which directs (or restricts) AR to canonical target genes in normal prostate tissue (Augello et al., 2019). This pattern is disrupted in the setting of *CHD1* loss, where aberrant AR cistromes are observed that more closely resemble those seen in prostate cancers (Augello et al., 2019). Collectively, the phenotypes of neuroendocrine gene expression and altered AR cistromes are consistent with our data showing that *CHD1* loss establishes an altered chromatin landscape, which enables activation of aberrant lineage programs as a mechanism to escape antiandrogen therapy.

In closing, it is worth considering the clinical implications of *CHD1* loss in prostate cancer. Our analysis of a limited cohort suggests that CRPC patients with low *CHD1* expression respond poorly to next-generation antiandrogen therapies. It will be important to validate this finding with a larger cohort, with inclusion of patients with genomic *CHD1* deletion as these were underrepresented in our study.

## STAR★METHODS

Detailed methods are provided in the online version of this paper and include the following:

- KEY RESOURCES TABLE
- LEAD CONTACT AND MATERIALS AVAILABILITY
- EXPERIMENTAL MODEL AND SUBJECT DETAIL
    - ○ SCID Mouse *In Vivo* Xenografts
    - ○ Human Prostate Cancer Cell Lines and Mouse Organoids
    - ○ shRNA and CRISPR Model Generation
- METHOD DETAILS
    - ○ Generation of the Human PCa Deletome and Construction of the miR-E shRNA Library
    - ○ *In Vivo* shRNA Mediated Screen and HiSeq
    - ○ Individual Plasmid Construction and Virus Production
    - ○ FACS-Based Growth Competition Assay
    - ○ Cell Growth Assay, Cell Viability Assays and Dose Response Curve
    - ○ Gene Expression Assay by qPCR
    - ○ Western Blot
    - ○ Immunofluorescence (IF)
    - ○ Immunohistochemistry (IHC)
    - ○ FACS-based Functional Screen Mediated by CRISPR/Cas9
- QUANTIFICATION AND STATISTICAL ANALYSIS
    - ○ Statistics Methods
    - ○ Analysis of Human Prostate Cancer Dataset
    - ○ Sample and library preparation for RNA-seq and ATAC-seq
    - ○ Analysis of RNA-seq Data
    - ○ GO Analysis
    - ○ GSEA Analysis
    - ○ Analysis of ATAC-seq Data
    - ○ Differential Binding Analysis
    - ○ ATAC-seq Differential Peak and RNA-Seq Fold Change CDF Plots
    - ○ Annotation and Differential Motif Detection
    - ○ Predicting Driver TFs Using RNA-seq and ATAC-seq Data
    - ○ Generating Density Heatmaps and Profiles
- DATA AND CODE AVAILABILITY

## SUPPLEMENTAL INFORMATION

Supplemental Information can be found online at https://doi.org/10.1016/j.ccell.2020.03.001.

## ACKNOWLEDGMENTS

We thank the cBioPortal, SU2C, and TCGA for providing genomic and transcriptomic data. We thank A.Viale, N. Socci, D. Nabors, and the MSKCC Integrated Genomics Operation for assistance with the library HiSeq. We thank A. Heguy and the NYU Genome Technology Center for assistance with the RNA-seq and ATAC-seq. We thank J. Zuber for providing retroviral- and lentiviral miR-E-based expression vectors, P. Chi and E. Wong for providing *CHD1*-expressing vectors, E. Lee, D.P. Yun, and H.A. Chen for providing constructs, W. Wu for all the artwork. We thank G. Hannon for critical discussion and feedback. This work was supported or partially supported by: the National Cancer Institute (NCI) and National Institutes of Health (NIH), USA (R00CA218885-04 to P.M., R01CA155169–04 and R01CA19387-01 to C.L.S., F99CA223063 to Z.Z., P30CA008748 to E.d.S., U54OD020355 to S.W.L. and E.d.S., P30CA034196 to S.L., R35CA197311 to J.T.M., and 1R01MH117406 to C.E.M.), Department of Defense, USA (PC170900 to P.M.), Cancer Prevention Research Institute (CPRIT), USA (RR170050 to P.M., RP160249 to J.T.M., and RP150596 to S.B. and V.M.), Prostate Cancer Foundation, USA (17YOUN12 to P.M.), Welch Foundation, USA (I-2005-20190330 to P.M. and I-1961-20180324 to J.T.M.), UTSW Deborah and W.A. Tex Moncrief, Jr. Scholar in Medical Research Award, USA (to P.M.), UTSW Harold C. Simmons Cancer Center Pilot Award, USA (to P.M.), Howard Hughes Medical Institute, USA (DT0712 to C.L.S., J.T.M., and S.L.W.), NIH/NCI/MSKCC Spore in Prostate Cancer, USA (P50 CA092629-14 to C.L.S.), NCI/MSKCC Support Grant/Core Grant, USA (P30CA008748-49 and P3CA008748-49-S2 to C.L.S.), the Starr Cancer Consortium, USA (I9-A9-071 to C.E.M.), the Vallee Foundation, USA (to C.E.M.), the WorldQuant Foundation, USA (to C.E.M.), the Pershing Square Sohn Cancer Research Alliance, USA (to C.E.M.), the Leukemia and Lymphoma Society, USA (LLS 9238-16 and LLS-MCL-982 to C.E.M.), the Jackson Laboratory New Investigator Award, USA (to S.L.), the Director's Innovation Fund, USA (to S.L.), and the NCATS (UL1 TR001866 to Y.L.).

## AUTHOR CONTRIBUTIONS

C.L.S. and P.M. conceived the project. Z.Z., C.Z., X.L., P.M., and C.L.S. oversaw the project, designed experiments, and interpreted data. P.M. and C.L.S. co-wrote the manuscript. K.N. and L.M. edited the manuscript. P.M., S.L., Y.L., and C.E.M. established the deletome. A.L. designed the shRNA library.

E.H., Z.C., and C.-H.H. constructed the shRNA library. Z.Z., C.Z., X.L., E.H., S.D., K.N., Y.S.L., C.W., and N.J. cloned all other plasmid constructs. Z.Z., X.L., N.J., J.W., D.C., X.C., and E.d.S. performed *in vivo* experiments. C.-C.C., S.B., V.M., J.T.M., and P.M. analyzed the library results. S.B., V.M., C.-C.C., and P.M. performed bioinformatic analysis. Z.Z., C.Z., X.L., S.D., C.R.T., and L.M. performed competition assays. Z.Z., C.Z., X.L., and S.D. established the tumor-derived cell lines. X.L. and S.D. performed inducible shCHD1 and *CHD1* rescue experiments. X.L. performed immunofluorescence and immunohistochemistry. X.L., S.D., C.W., and C.R.T. performed dose-response experiments. S.D. performed proliferation assays. C.Z., X.L., and C.W. performed the CRISPR library screen. Z.Z., C.Z., X.L., S.D., E.H., and C.W. performed western blots and qPCR. W.A., Y.Z., Z.Z., E.L., and P.M. performed clinical data analysis. Y.Z. examined all the statistic tests. S.W.L. supervised the construction of the library and offered critical feedback. C.L.S. and P.M. are the corresponding authors of this manuscript.

## DECLARATION OF INTERESTS

C.L.S. and J.W. are co-inventors of enzalutamide and apalutamide and may be entitled to royalties. C.L.S. serves on the Board of Directors of Novartis and is a co-founder of ORIC Pharm. He is a science advisor to Agios, Beigene, Blueprint, Column Group, Foghorn, Housey Pharma, Nextech, KSQ, Petra, and PMV. He was a co-founder of Seragon, purchased by Genentech/Roche in 2014. S.W.L. is a founder and member of the scientific advisory board of ORIC Pharmaceuticals, Blueprint Medicines, and Mirimus, Inc.; he is also on the scientific advisory board of PMV Pharmaceuticals, Constellation Pharmaceuticals, and Petra Pharmaceuticals. W.A. reports consulting for Clovis Oncology, Janssen, MORE Health, and ORIC Pharmaceuticals. He received honoraria from CARET and travel accommodations from GlaxoSmith Kline, Clovis Oncology, and ORIC Pharmaceuticals. C.E.M is a co-founder and board member for Biotia and Onegevity Health, as well as an advisor for Genpro and Karius.

Received: April 16, 2019
Revised: November 4, 2019
Accepted: February 28, 2020
Published: March 26, 2020

## REFERENCES

Abida, W., Armenia, J., Gopalan, A., Brennan, R., Walsh, M., Barron, D., Danila, D., Rathkopf, D., Morris, M., Slovin, S., et al. (2017). Prospective genomic profiling of prostate cancer across disease states reveals germline and somatic alterations that may affect clinical decision making. JCO Precis Oncol. *2017*, https://doi.org/10.1200/PO.17.00029.

Abida, W., Cyrta, J., Heller, G., Prandi, D., Armenia, J., Coleman, I., Cieslik, M., Benelli, M., Robinson, D., Allen, E.M., et al. (2019). Genomic correlates of clinical outcome in advanced prostate cancer. Proc. Natl. Acad Sci U S A *116*, 11428–11436.

Albrecht, B.K., Gehling, V.S., Hewitt, M.C., Vaswani, R.G., Côtô, A., Leblanc, Y., Nasveschuk, C.G., Bellon, S., Bergeron, L., Campbell, R., et al. (2016). Identification of a benzoisoxazoloazepine inhibitor (CPI-0610) of the bromodomain and extra-terminal (BET) family as a candidate for human clinical trials. J. Med. Chem. *59*, 1330–1339.

Alizadeh, A.A., Aranda, V., Bardelli, A., Blanpain, C., Bock, C., Borowski, C., Caldas, C., Califano, A., Doherty, M., Elsner, M., et al. (2015). Toward understanding and exploiting tumor heterogeneity. Nat. Med. *21*, 846–853.

Arora, V.K., Schenkein, E., Murali, R., Subudhi, S.K., Wongvipat, J., Balbas, M.D., Shah, N., Cai, L., Efstathiou, E., Logothetis, C., et al. (2013). Glucocorticoid receptor confers resistance to antiandrogens by bypassing androgen receptor blockade. Cell *155*, 1309–1322.

Augello, M.A., Liu, D., Deonarine, L.D., Robinson, B.D., Huang, D., Stelloo, S., Blattner, M., Doane, A.S., Wong, E., Chen, Y., et al. (2019). CHD1 loss alters AR binding at lineage-specific enhancers and modulates distinct transcriptional programs to drive prostate tumorigenesis. Cancer Cell *35*, 817–819.

Bailey, T.L., Boden, M., Buske, F.A., Frith, M., Grant, C.E., Clementi, L., Ren, J., Li, W.W., and Noble, W.S. (2009). MEME SUITE: tools for motif discovery and searching. Nucleic Acids Res *37*, W202–W208.

Bailey, T.L., Johnson, J., Grant, C.E., and Noble, W.S. (2015). The MEME suite. Nucleic Acids Res. *43*, W39–W49.

Balbas, M.D., Evans, M.J., Hosfield, D.J., Wongvipat, J., Arora, V.K., Watson, P.A., Chen, Y., Greene, G.L., Shen, Y., and Sawyers, C.L. (2013). Overcoming mutation-based resistance to antiandrogens with rational drug design. eLife *2*, e00499.

Barbieri, C.E., Baca, S.C., Lawrence, M.S., Demichelis, F., Blattner, M., Theurillat, J.-P., White, T.A., Stojanov, P., Allen, E., Stransky, N., et al. (2012). Exome sequencing identifies recurrent SPOP, FOXA1 and MED12 mutations in prostate cancer. Nat. Genet. *44*, 685–689.

Barnes S.D., Ruess H., and Malladi V.S. (2019). BICF ATAC-seq Analysis Workflow (Version publish_1.0.0). Zenodo. http://doi.org/10.5281/zenodo.3526149.

Beer, T.M., Armstrong, A.J., Rathkopf, D.E., Loriot, Y., Sternberg, C.N., Higano, C.S., Iversen, P., Bhattacharya, S., Carles, J., Chowdhury, S., et al. (2014). Enzalutamide in metastatic prostate cancer before chemotherapy. N. Engl. J. Med. *371*, 424–433.

Beltran, H., Prandi, D., Mosquera, J.-M., Benelli, M., Puca, L., Cyrta, J., Marotz, C., Giannopoulou, E., Chakravarthi, B.V., Varambally, S., et al. (2016). Divergent clonal evolution of castration-resistant neuroendocrine prostate cancer. Nat. Med. *22*, 298–305.

Beltran, H., Rickman, D., Park, K., Chae, S., Sboner, A., MacDonald, T., Wang, Y., Sheikh, K., Terry, S., Tagawa, S., et al. (2011). Molecular characterization of neuroendocrine prostate cancer and identification of new drug targets. Cancer Discov. *1*, 487–495.

Bishop, J.L., Thaper, D., Vahid, S., Davies, A., Ketola, K., Kuruma, H., Jama, R., Nip, K., Angeles, A., Johnson, F., et al. (2017). The master neural transcription factor BRN2 is an androgen receptor-suppressed driver of neuroendocrine differentiation in prostate cancer. Cancer Discov. *7*, 54–71.

Boysen, G., Rodrigues, D., Rescigno, P., Seed, G., Dolling, D.I., Riisnaes, R., Crespo, M., Zafeiriou, Z., Sumanasuriya, S., Bianchini, D., et al. (2018). SPOP mutated/CHD1 deleted lethal prostate cancer and abiraterone sensitivity. Clin. Cancer Res. *24*, 5585–5593.

Chen, Y., Chi, P., Rockowitz, S., Iaquinta, P.J., Shamu, T., Shukla, S., Gao, D., Sirota, I., Carver, B.S., Wongvipat, J., et al. (2013). ETS factors reprogram the androgen receptor cistrome and prime prostate tumorigenesis in response to PTEN loss. Nat Med *19*, 1023–1029.

Chen, C.D., Welsbie, D.S., Tran, C., Baek, S., Chen, R., Vessella, R., Rosenfeld, M.G., and Sawyers, C.L. (2003). Molecular determinants of resistance to antiandrogen therapy. Nat. Med. *10*, 33–39.

Denny, S.K., Yang, D., Chuang, C.-H., Brady, J.J., Lim, J., Grüner, B.M., Chiou, S.-H., Schep, A.N., Baral, J., Hamard, C., et al. (2016). Nfib promotes metastasis through a widespread increase in chromatin accessibility. Cell *166*, 328–342.

Du, W.-L., Fang, Q., Chen, Y., Teng, J.-W., Xiao, Y.-S., Xie, P., Jin, B., and Wang, J.-Q. (2017). Effect of silencing the T-Box transcription factor TBX2 in prostate cancer PC3 and LNCaP cells. Mol. Med. Rep. *16*, 6050–6058.

Fellmann, C., Hoffmann, T., dhar, V., Hopfgartner, B., Muhar, M., Roth, M., Lai, D., Barbosa, I.A., Kwon, J., Guan, Y., et al. (2013). An optimized microRNA backbone for effective single-copy RNAi. Cell Rep. *5*, 1704–1713.

Feng, J., Liu, T., Qin, B., Zhang, Y., and Liu, X. (2012). Identifying ChIP-seq enrichment using MACS. Nat. Protoc. *7*, 1728.

Franco, H.L., Nagari, A., Malladi, V.S., Li, W., Xi, Y., Richardson, D., Allton, K.L., Tanaka, K., Li, J., Murakami, S., et al. (2018). Enhancer transcription reveals subtype-specific gene expression programs controlling breast cancer pathogenesis. Genome Res. *28*, 159–170.

Gao, D., Vela, I., Sboner, A., Iaquinta, P.J., Karthaus, W.R., Gopalan, A., Dowling, C., Wanjala, J.N., Undvall, E.A., Arora, V.K., et al. (2014). Organoid cultures derived from patients with advanced prostate cancer. Cell *159*, 176–187.

Garraway, L.A., Widlund, H.R., Rubin, M.A., Getz, G., Berger, A.J., Ramaswamy, dhar, Beroukhim, R., Milner, D.A., Granter, S.R., Du, J., et al. (2005). Integrative genomic analyses identify MITF as a lineage survival oncogene amplified in malignant melanoma. Nature *436*, 117.

Gaspar-Maia, A., Alajem, A., Polesso, F., dharan, R., Mason, M.J., Heidersbach, A., Ramalho-Santos, J., McManus, M.T., Plath, K., Meshorer, E., et al. (2009). Chd1 regulates open chromatin and pluripotency of embryonic stem cells. Nature *460*, 863–868.

Golden, R.J., Chen, B., Li, T., Braun, J., Manjunath, H., Chen, X., Wu, J., Schmid, V., Chang, T.-C., Kopp, F., et al. (2017). An Argonaute phosphorylation cycle promotes microRNA-mediated silencing. Nature *542*, 197–202.

Goldman, S.L., MacKay, M., Afshinnekoo, E., Melnick, A.M., Wu, S., and Mason, C.E. (2019). The impact of heterogeneity on single-cell sequencing. Front. Genet. *10*, 8.

Grasso, C.S., Wu, Y.-M., Robinson, D.R., Cao, X., anasekaran, S., Khan, A.P., Quist, M.J., Jing, X., Lonigro, R.J., Brenner, C.J., et al. (2012). The mutational landscape of lethal castration-resistant prostate cancer. Nature *487*, 239–243.

Hassan, C., Afshinnekoo, E., Li, S., Wu, S., and Mason, C.E. (2017). Genetic and epigenetic heterogeneity and the impact on cancer relapse. Exp. Hematol. *54*, 26–30.

Heinz, S., Benner, C., Spann, N., Bertolino, E., Lin, Y.C., Laslo, P., Cheng, J.X., Murre, C., Singh, H., and Glass, C.K. (2010). Simple combinations of lineage-determining transcription factors prime *cis*-regulatory elements required for macrophage and B cell identities. Mol. Cell *38*, 576–589.

Holcomb, I.N., Young, J.M., Coleman, I.M., Salari, K., Grove, D.I., Hsu, L., True, L.D., Roudier, M.P., Morrissey, C.M., Higano, C.S., et al. (2009). Comparative analyses of chromosome alterations in soft-tissue metastases within and across patients with castration-resistant prostate cancer. Cancer Res. *69*, 7793–7802.

Huang, S., Gulzar, Z., Salari, K., Lapointe, J., Brooks, J., and Pollack, J. (2011). Recurrent deletion of CHD1 in prostate cancer with relevance to cell invasiveness. Oncogene *31*, 4164–4170.

Isikbay, M., Otto, K., Kregel, S., Kach, J., Cai, Y., Griend, D.J., Conzen, S.D., and Szmulewitz, R.Z. (2014). Glucocorticoid receptor activity contributes to resistance to androgen-targeted therapy in prostate cancer. Horm. Cancer *5*, 72–89.

Karthaus, W.R., Iaquinta, P.J., Drost, J., Gracanin, A., van Boxtel, R., Wongvipat, J., wling, C., Gao, D., Begthel, H., Sachs, N., et al. (2014). Identification of multipotent luminal progenitor cells in human prostate organoid cultures. Cell *159*, 163–175.

Khan, A., Fornes, O., Stigliani, A., Gheorghe, M., Castro-Mondragon, J.A., van der Lee, R., Bessy, A., Cheneby, J., Kulkarni, S.R., and Tan, G. (2017). Jaspar 2018: update of the open-access database of transcription factor binding profiles and its web framework. Nucleic Acids Res. *46*, D1284.

Kim, J.H., anasekaran, S., Mehra, R., Tomlins, S.A., Gu, W., Yu, J., Kumar-Sinha, C., Cao, X., Dash, A., Wang, L., et al. (2007). Integrative analysis of genomic aberrations associated with prostate cancer progression. Cancer Res. *67*, 8229–8239.

Klein, K.A., Reiter, R.E., Redula, J., Moradi, H., Zhu, X., Brothman, A.R., Lamb, D.J., Marcelli, M., Belldegrun, A., Witte, O.N., et al. (1997). Progression of metastatic human prostate cancer to androgen independence in immunodeficient SCID mice. Nat. Med. *3*, 402–408.

Ku, S., Rosario, S., Wang, Y., Mu, P., Seshadri, M., Goodrich, Z.W., Goodrich, M.M., Labbé, D.P., Gomez, E., Wang, J., et al. (2017). Rb1 and Trp53 cooperate to suppress prostate cancer lineage plasticity, metastasis, and antiandrogen resistance. Science *355*, 78–83.

Landt, S.G., Marinov, G.K., Kundaje, A., Kheradpour, P., Pauli, F., Batzoglou, S., Bernstein, B.E., Bickel, P., Brown, J.B., Cayting, P., et al. (2012). ChIP-seq guidelines and practices of the ENCODE and modENCODE consortia. Genome Res *22*, 1813–1831.

Li, J., Alyamani, M., Zhang, A., Chang, K.-H., Berk, M., Li, Z., Zhu, Z., Petro, M., Magi-Galluzzi, C., Taplin, M.-E., et al. (2017). Aberrant corticosteroid metabolism in tumor cells enables GR takeover in enzalutamide resistant prostate cancer. eLife *6*, e20183.

Li, H., and Durbin, R. (2009). Fast and accurate short read alignment with Burrows-Wheeler transform. Bioinformatics *25*, 1754–1760.

Li, S., Garrett-Bakelman, F.E., Chung, S.S., Sanders, M.A., Hricik, T., Rapaport, F., Patel, J., Dillon, R., Vijay, P., Brown, A.L., et al. (2016). Distinct evolution and dynamics of epigenetic and genetic heterogeneity in acute myeloid leukemia. Nat. Med. *22*, 792–799.

Li, H., Handsaker, B., Wysoker, A., Fennell, T., Ruan, J., Homer, N., Marth, G., Abecasis, G., and Durbin, R. (2009). The sequence alignment/map format and SAMtools. Bioinformatics *25*, 2078–2079.

Liao, Y., Smyth, G.K., and Shi, W. (2014). featureCounts: an efficient general purpose program for assigning sequence reads to genomic features. Bioinformatics *30*, 923–930.

Liu, W., Lindberg, J., Sui, G., Luo, J., Egevad, L., Li, T., Xie, C., Wan, M., Kim, S.-T., Wang, Z., et al. (2012). Identification of novel CHD1-associated collaborative alterations of genomic structure and functional assessment of CHD1 in prostate cancer. Oncogene *31*, 3939.

Love, M.I., Huber, W., and Anders, S. (2014). Moderated estimation of fold change and dispersion for RNA-seq data with DESeq2. Genome Biol. *15*, 550.

Martin, M. (2011). Cutadapt removes adapter sequences from high-throughput sequencing reads. Embnet.journa. *17*, https://doi.org/10.14806/ej.17.1.200.

Mi, H., Muruganujan, A., Ebert, D., Huang, X., and Thomas, P.D. (2018). PANTHER version 14: more genomes, a new PANTHER GO-slim and improvements in enrichment analysis tools. Nucleic Acids Res *47*, D419–D426.

Müllner, D. (2013). Fast Hierarchical Clustering Routines for R and Python. R Package Fastcluster Version 1.

Mu, P., Zhang, Z., Benelli, M., Karthaus, W.R., Hoover, E., Chen, C.-C., Wongvipat, J., Ku, S., Gao, D., Cao, Z., et al. (2017). SOX2 promotes lineage plasticity and antiandrogen resistance in TP53- and RB1-deficient prostate cancer. Science *355*, 84–88.

Mudge, J.M., and Harrow, J. (2015). Creating reference gene annotation for the mouse C57BL6/J genome assembly. Mamm. Genome *26*, 366–378.

Nandana, S., Tripathi, M., Duan, P., Chu, C.-Y., Mishra, R., Liu, C., Jin, R., Yamashita, H., Zayzafoon, M., Bhowmick, N.A., et al. (2017). Bone metastasis of prostate cancer can be therapeutically targeted at the TBX2-WNT signaling axis. Cancer Res. *77*, 1331–1344.

Network, C. (2015). The molecular taxonomy of primary prostate cancer. Cell *163*, 1011–1025.

Park, J., Lee, J.K., Sheu, K.M., Wang, L., Balanis, N.G., Nguyen, K., Smith, B.A., Cheng, C., Tsai, B.L., Cheng, D., et al. (2018). Reprogramming normal human epithelial tissues to a common, lethal neuroendocrine cancer lineage. Science *362*, 91–95.

Pelossof, R., Fairchild, L., Huang, C.-H., Widmer, C., edharan, V.T., Sinha, N., Lai, D., Guan, Y., Premsrirut, P.K., Tschaharganeh, D.F., et al. (2017). Prediction of potent shRNAs with a sequential classification algorithm. Nat. Biotechnol. *35*, 350–353.

Pertea, M., Kim, D., Pertea, G.M., Leek, J.T., and Salzberg, S.L. (2016). Transcript-level expression analysis of RNA-seq experiments with HISAT, StringTie and Ballgown. Nat. Protoc. *11*, 1650.

Quinlan, A.R., and Hall, I.M. (2010). BEDTools: a flexible suite of utilities for comparing genomic features. Bioinformatics *26*, 841–842.

R Core Team (2016). R: A Language and Environment for Statistical Computing (R Foundation for Statistical Computing). https://www.R-project.org/.

Ramírez, F., Ryan, D.P., Grüning, B., Bhardwaj, V., Kilpert, F., Richter, A.S., Heyne, S., Dündar, F., and Manke, T. (2016). deepTools2: a next generation web server for deep-sequencing data analysis. Nucleic Acids Res. *44*, W160–W165.

Ren, S., Wei, G.-H., Liu, D., Wang, L., Hou, Y., Zhu, S., Peng, L., Zhang, Q., Cheng, Y., Su, H., et al. (2018). Whole-genome and transcriptome sequencing of prostate cancer identify new genetic alterations driving disease progression. Eur. Urol. *73*, 322–339.

Robinson, D., Allen, E.M., Wu, Y.-M., Schultz, N., Lonigro, R.J., Mosquera, J.-M., Montgomery, B., Taplin, M.-E., Pritchard, C.C., Attard, G., et al.

Please cite this article in press as: Zhang et al., Loss of *CHD1* Promotes Heterogeneous Mechanisms of Resistance to AR-Targeted Therapy via Chromatin Dysregulation, Cancer Cell (2020), https://doi.org/10.1016/j.ccell.2020.03.001

(2015). Integrative clinical genomics of advanced prostate cancer. Cell *161*, 1215–1228.

Rodrigues, L., Rider, L., Nieto, C., Romero, L., Karimpour-Fard, A., Loda, M., Luciai, M.S., Wu, M., Shi, L., Cimic, A., et al. (2015). Coordinate loss of MAP3K7 and CHD1 promotes aggressive prostate cancer. Cancer Res. *75*, 1021–1034.

Ryan, C.J., Smith, M.R., de Bono, J.S., Molina, A., Logothetis, C.J., de Souza, P., Fizazi, K., Mainwaring, P., Piulats, J.M., Ng, S., et al. (2013). Abiraterone in metastatic prostate cancer without previous chemotherapy. N. Engl. J. Med. *368*, 138–148.

Sequist, L.V., Waltman, B.A., Dias-Santagata, D., Digumarthy, S., Turke, A.B., Fidias, P., Bergethon, K., Shaw, A.T., Gettinger, S., Cosper, A.K., et al. (2011). Genotypic and histological evolution of lung cancers acquiring resistance to EGFR inhibitors. Sci. Transl Med. *3*, 75ra26.

Shah, N., Wang, P., Wongvipat, J., Karthaus, W.R., Abida, W., Armenia, J., Rockowitz, S., Drier, Y., Bernstein, B.E., Long, H.W., et al. (2017). Regulation of the glucocorticoid receptor via a BET-dependent enhancer drives antiandrogen resistance in prostate cancer. eLife *6*, e27861.

Shenoy, T., Boysen, G., Wang, M., Xu, Q., Guo, W., Koh, F., Wang, C., Zhang, L., Wang, Y., Gil, V., et al. (2017). CHD1 loss sensitizes prostate cancer to DNA damaging therapy by promoting error-prone double-strand break repair. Ann. Oncol. *28*, 1495–1507.

Shi, W., Wang, D., Yuan, X., Liu, Y., Guo, X., Li, J., and Song, J. (2019). Glucocorticoid receptor-IRS-1 axis controls EMT and the metastasis of breast cancers. J. Mol. Cell Biol. *11*, 1042–1055.

Smith, M.R., Saad, F., Chowdhury, S., Oudard, S., Hadaschik, B.A., Graff, J.N., Olmos, D., Mainwaring, P.N., Lee, J., Uemura, H., et al. (2018). Apalutamide treatment and metastasis-free survival in prostate cancer. N. Engl. J. Med. *378*, 1408–1418.

Sosa, M., Parikh, F., Maia, A., Estrada, Y., Bosch, A., Bragado, P., Ekpin, E., George, A., Zheng, Y., Lam, H.-M., et al. (2015). NR2F1 controls tumour cell dormancy via SOX9- and RARβ-driven quiescence programmes. Nat. Commun. *6*, 6170.

Stark, R., and Brown, G. (2011). DiffBind: Differential Binding Analysis of ChIP-Seq Peak Data. R Package Version 100. http://bioconductor.org/packages/release/bioc/vignettes/DiffBind/inst/doc/DiffBind.pdf

Tarasov, A., Vilella, A.J., Cuppen, E., Nijman, I.J., and Prins, P. (2015). Sambamba: fast processing of NGS alignment formats. Bioinformatics *31*, 2032–2034.

Taylor, B.S., Barretina, J., Socci, N.D., Decarolis, P., Ladanyi, M., Meyerson, M., Singer, S., and Sander, C. (2008). Functional copy-number alterations in cancer. PLos One *3*, e3179.

Taylor, B.S., Schultz, N., Hieronymus, H., Gopalan, A., Xiao, Y., Carver, B.S., Arora, V.K., Kaushik, P., Cerami, E., Reva, B., et al. (2010). Integrative genomic profiling of human prostate cancer. Cancer Cell *18*, 11–22.

Tran, C., Ouk, S., Clegg, N., Chen, Y., Watson, P., Arora, V., Wongvipat, J., ith-Jones, P., Yoo, D., Kwon, A., et al. (2009). Development of a second-generation antiandrogen for treatment of advanced prostate cancer. Science *324*, 787–790.

Tripodi, I.J., Allen, M.A., and Dowell, R.D. (2018). Detecting differential transcription factor Activity from ATAC-seq data. Molecules *23*, 1136.

Varghese, F., Bukhari, A.B., Malhotra, R., and De, A. (2014). IHC profiler: an open source plugin for the quantitative evaluation and automated scoring of immunohistochemistry images of human tissue samples. PLoS One *9*, e96801.

Watson, P.A., Arora, V.K., and Sawyers, C.L. (2015). Emerging mechanisms of resistance to androgen receptor inhibitors in prostate cancer. Nat. Rev. Cancer *15*, 701–711.

Wheeler, D.B., Zoncu, R., Root, D.E., batini, D., and Sawyers, C.L. (2015). Identification of an oncogenic RAB protein. Science *350*, 211–217.

Yang, D., Denny, S.K., Greenside, P.G., Chaikovsky, A.C., Brady, J.J., Ouadah, Y., Granja, J.M., Jahchan, N.S., Lim, J., Kwok, S., et al. (2018). Intertumoral heterogeneity in SCLC is influenced by the cell type of origin. Cancer Discov. *8*, 1316–1331.

Zack, G., Rogers, W., and Latt, S. (1977). Automatic measurement of sister chromatid exchange frequency. J. Histochem. Cytochem. Official J. Histochem. Soc. *25*, 741–753.

Zhao, D., Lu, X., Wang, G., Lan, Z., Liao, W., Li, J., Liang, X., Chen, J., Shah, S., Shang, X., et al. (2017). Synthetic essentiality of chromatin remodelling factor CHD1 in PTEN-deficient cancer. Nature *542*, 484.

Zuber, J., McJunkin, K., Fellmann, C., Dow, L.E., Taylor, M.J., Hannon, G.J., and Lowe, S.W. (2010). Toolkit for evaluating genes required for proliferation and survival using tetracycline-regulated RNAi. Nat. Biotechnol. *29*, 79–83.

Zuber, J., Shi, J., Wang, E., Rappaport, A.R., Herrmann, H., Sison, E.A., Magoon, D., Qi, J., Blatt, K., Wunderlich, M., et al. (2011). RNAi screen identifies Brd4 as a therapeutic target in acute myeloid leukaemia. Nature *478*, 524–528.

Please cite this article in press as: Zhang et al., Loss of *CHD1* Promotes Heterogeneous Mechanisms of Resistance to AR-Targeted Therapy via Chromatin Dysregulation, Cancer Cell (2020), https://doi.org/10.1016/j.ccell.2020.03.001

## STAR★METHODS

### KEY RESOURCES TABLE

| REAGENT or RESOURCE | SOURCE | IDENTIFIER |
|---|---|---|
| Antibodies | | |
| CHD1 (D8C2) Rabbit mAb | Cell Signaling | Cat #4351;<br>RRID: AB_11179073 |
| AR Antibody (N-20) | Santa Cruz | sc-816;<br>RRID: AB_1563391 |
| PSA/KLK3 (D6B1) XP® Rabbit mAb | Cell Signaling | Cat # 5365; RRID: AB_2797609 |
| PMEPA1 Antibody (P-15) | Santa Cruz | Cat # sc-85829;<br>RRID: AB_2252615 |
| STEAP Antibody (B-4) | Santa Cruz | Cat # sc-271872;<br>RRID: AB_10707830 |
| β-Actin (13E5) Rabbit mAb | Cell Signaling | Cat # 4970;<br>RRID: AB_10694076 |
| Glucocorticoid Receptor (D6H2L) XP® Rabbit mAb | Cell Signaling | Cat #12041;<br>RRID: AB_2631286 |
| SGK1 (D27C11) Rabbit mAb | Cell Signaling | Cat #12103;<br>RRID: AB_2687476 |
| c-Myc (D84C12) Rabbit mAb | Cell Signaling | Cat #5605;<br>RRID: AB_1903938 |
| NR2F1 (H8132) mouse mAb | R&D Systems, Inc. | Cat PP-H8132-00; RRID: AB_2155494 |
| Alexa Fluor® 488 AffiniPure Goat Anti-Mouse IgG (H+L) | Jackson Immunoresearch | Cat: 115-545-003;<br>RRID: AB_2338840 |
| Alexa Fluor® 594 AffiniPure Goat Anti-Rabbit IgG (H+L) | Jackson Immunoresearch | Cat: 111-585-003;<br>RRID: AB_2338059 |
| VECTASTAIN® ABC HRP Kit- Rabbit IgG | Peroxidase | Cat:PK-6101;<br>RRID: AB_2336815 |
| Chemicals, Peptides, and Recombinant Proteins | | |
| Enzalutamide | Selleck Chemicals | S1250 |
| CPI-0610 | Selleck Chemicals | S7853 |
| JQ-1 | Selleck Chemicals | S7110 |
| GlutaMAXTM Supplement | Gibco | 35050061 |
| 1M HEPES Solution | Gibco | 15630080 |
| 100mM Sodium Pyruvate | Gibco | 11360-070 |
| Penicillin-streptomycin | Sigma Aldrich | P0781-100ML |
| Puromycin | Gibco | A1113803 |
| Blasticidin | Gibco | A1113903 |
| Doxycycline | Sigma Aldrich | D3072-1ML |
| Trizol | Ambion | 15596018 |
| 20X NuPAGE MES SDS buffer | Novex | NP0002 |
| 1X Bolt Transfer buffer | Novex | BT00061 |
| 100% methanol | Thermo Fisher | A412-20 |
| Fetal Bovine Serum, charcoal stripped | Gibco | 12-676-029 |
| TrypLE Express | Gibco | 12605-010 |
| Transposase enzyme | Illumina Nextera | 15028252 |
| Critical Commercial Assays | | |
| SuperScript™ IV VILO™ Master Mix with ezDNase™ Enzyme | Thermo Fisher | 11766500 |
| 2X PowerUp™ SYBR™ Green Master Mix | Thermo Fisher | A25778 |
| Pierce BCA Protein Assay Kit | Thermo Fisher | 23225 |

(*Continued on next page*)

Please cite this article in press as: Zhang et al., Loss of *CHD1* Promotes Heterogeneous Mechanisms of Resistance to AR-Targeted Therapy via Chromatin Dysregulation, Cancer Cell (2020), https://doi.org/10.1016/j.ccell.2020.03.001

***Continued***

| REAGENT or RESOURCE | SOURCE | IDENTIFIER |
|---|---|---|
| MycoAlertTM PLUS Mycoplasma Detection kit | Lonza | LT07-710 |
| Lipofectamine 2000 Transfection Reagent | Thermo Fisher | 11668500 |
| Qiagen MinElute PCR purification kit | Qiagen | 28004 |
| ImmPACT™ DAB Peroxidase (HRP) Substrate | LSBio | LS-J1075-120 |
| CellTiter-Glo luminescent cell viability assay | Promega | cat #7570 |
| Deposited Data | | |
| Library Hi-seq | GEO | GSE127957 |
| RNA-seq | GEO | GSE126917 |
| ATAC-seq | GEO | GSE127241 |
| Experimental Models: Cell Lines | | |
| LNCaP/AR | Chen et al., 2003 | N/A |
| LREX | Arora et al., 2013 | N/A |
| CWR22Pc | Mu et al., 2017 | N/A |
| LAPC4 | ATCC | N/A |
| *Pten*$^{-/-}$ mouse organoid | Chen et al., 2013 | N/A |
| E006AA | ATCC | N/A |
| shCHD1-XE-1 | This paper | N/A |
| shCHD1-XE-2 | This paper | N/A |
| shCHD1-XE-3 | This paper | N/A |
| shCHD1-XE-4 | This paper | N/A |
| shCHD1-XE-5 | This paper | N/A |
| shCHD1-XE-6 | This paper | N/A |
| shCHD1-XE-7 | This paper | N/A |
| shCHD1-XE-8 | This paper | N/A |
| shCHD1-XE-9 | This paper | N/A |
| sgCHD1-XE-1 | This paper | N/A |
| sgCHD1-XE-2 | This paper | N/A |
| sgCHD1-XE-3 | This paper | N/A |
| sgCHD1-XE-4 | This paper | N/A |
| sgCHD1-XE-5 | This paper | N/A |
| sgCHD1-XE-6 | This paper | N/A |
| sgCHD1-XE-7 | This paper | N/A |
| shNT-XV-1 | This paper | N/A |
| shNT-XV-2 | This paper | N/A |
| shCHD1-XV-1 | This paper | N/A |
| shCHD1-XV-2 | This paper | N/A |
| Experimental Models: Organisms/Strains | | |
| C.B-*Igh*-1$^{b}$/IcrTac-*Prkdc*$^{scid}$ mouse | Taconic | CB17SC-M |
| Oligonucleotides | | |
| LEPG-shNT:TGCTGTTGACAGTGAGCGCAGGAATTATAATGCTTATCTATAGTGAAGCCACAGATGTATAGATAAGCATTATAATTCCTATGCCTACTGCCTCGGA | This paper | N/A |
| LEPG-shCHD1-1: TGCTGTTGACAGTGAGCGACAGGTTAACATTTTAGATAAATAGTGAAGCCACAGATGTATTTATCTAAAATGTTAACCTGGTGCCTACTGCCTCGGACTTCAAGGGGCTAGAATTC | This paper | N/A |
| LEPG-shCHD1-2: TGCTGTTGACAGTGAGCGACAGGAAATGGATATAGATGAATAGTGAAGCCACAGATGTATTCATCTATATCCATTTCCTGGTGCCTACTGCCTCGGACTTCAAGGGGCTAGAATTC | This paper | N/A |

(*Continued on next page*)

***Continued***

| REAGENT or RESOURCE | SOURCE | IDENTIFIER |
|---|---|---|
| LEPG-shCHD1-3:<br>TGCTGTTGACAGTGAGCGCAACGTTATATATGACAAATTATAGTGAAGCCACAGATGTATAATTTGTCATATATAACGTTTTGCCTACTGCCTCGGACTTCAAGGGGCTAGAATTC | This paper | N/A |
| LEPG-shCHD1-4:<br>TGCTGTTGACAGTGAGCGACAGGAGAGATTCAGTATTTAATAGTGAAGCCACAGATGTATTAAATACTGAATCTCTCCTGGTGCCTACTGCCTCGGACTTCAAGGGGCTAGAATTC | This paper | N/A |
| LEPG-shCHD1-5:<br>TGCTGTTGACAGTGAGCGCTAGGCGGTTTATCAAGAGCTATAGTGAAGCCACAGATGTATAGCTCTTGATAAACCGCCTAATGCCTACTGCCTCGGACTTCAAGGGGCTAGAATTC | This paper | N/A |
| LT3CEPIR-shGR-1:<br>TGCTGTTGACAGTGAGCGCCCAAAGCAGTTTCACTCTCAATAGTGAAGCCACAGATGTATTGAGAGTGAAACTGCTTTGGATGCCTACTGCCTCGGA | This paper | N/A |
| LT3CEPIR-shGR-2:<br>TGCTGTTGACAGTGAGCGAAAGCTGTAAAGTTTTCTTCAATAGTGAAGCCACAGATGTATTGAAGAAAACTTTACAGCTTCTGCCTACTGCCTCGGA | This paper | N/A |
| lentiCRISPRv2-sgCHD1-1-F: CACCGTCAGCTCCATCAACTTTCGG<br>lentiCRISPRv2-sgCHD1-1-R: AAACCCGAAAGTTGATGGAGCTGAC | This paper | N/A |
| lentiCRISPRv2-sgCHD1-2-F: CACCGGATTTATGGATTGTCGGATT<br>lentiCRISPRv2-sgCHD1-2-R: AAACAATCCGACAATCCATAAATCC | This paper | N/A |
| Additional sgRNA sequences, see Tables S5 and S6 | N/A | N/A |
| Primers, see Table S6 | N/A | N/A |
| Recombinant DNA | | |
| pMSCV-miRE-PGK-PuroR-IRES-GFP | Fellmann et al.,2013 | LEPG |
| pRRL-GFP-miRE-PGK-PuroR | Fellmann et al.,2013 | SGEP |
| pRRL-TRE3G-GFP-miRE-PGK-PuroR-IRES-rtTA3 | Fellmann et al.,2013 | LT3GEPIR |
| pMSCV-miRE-PGK-PuroR-IRES-mCherry | Mu et al., 2017 | LEPC |
| pRRL-mCherry-miRE-PGK-PuroR | Mu et al., 2017 | SCEP |
| pRRL-TRE3G-mCherry-miRE-PGK-PuroR-IRES-rtTA3 | Mu et al., 2017 | LT3CEPIR |
| lentiCRISPR v2 | Addgene | Cat #52961 |
| pLKO5.sgRNA.EFS.tRFP | Addgene | Cat #57823 |
| lentiCas9-Blast | Addgene | Cat #52962 |
| Software and Algorithms | | |
| HISAT (v 2.0.1) | Pertea et al., 2016 | http://ccb.jhu.edu/software/hisat2/index.shtml |
| Sambamba (v0.6.6) | Tarasov et al., 2015 | http://lomereiter.github.io/sambamba/ |
| Featurecount (v1.4.6) | Liao et al., 2014 | http://bioinf.wehi.edu.au/featureCounts/ |
| DEseq2 (v1.6.3) | Love et al., 2014 | https://bioconductor.org/packages/release/bioc/html/DESeq2.html |
| PANTHER | Mi et al., 2018 | http://www.pantherdb.org |
| Trimgalore (v0.4.1) | Martin, 2011 | https://www.bioinformatics.babraham.ac.uk/projects/trim_galore |
| BWA (v0.7.12) | Li and Durbin, 2009 | http://bio-bwa.sourceforge.net |
| Samtools (v1.3) | Li et al., 2009 | http://samtools.sourceforge.net |
| BEDTools (v2.26.0) | Quinlan and Hall, 2010 | https://bedtools.readthedocs.io/en/latest |
| MACS (v2.1.0) | Feng et al., 2012 | https://github.com/taoliu/MACS |
| R (v3.3.2) package DiffBind (v2.2.12) | R Core Team, 2016;<br>Stark and Brown, 2011 | https://bioconductor.org/packages/release/bioc/html/DiffBind.html |

(*Continued on next page*)

***Continued***

| REAGENT or RESOURCE | SOURCE | IDENTIFIER |
|---|---|---|
| MEME suite (v4.11.1) | Bailey et al., 2009<br>Bailey et al., 2015 | http://meme-suite.org |
| DAStk (v0.1.5) | Tripodi et al., 2018 | https://pypi.org/project/DAStk |
| HOMER (v4.9) | Heinz et al., 2010 | http://homer.ucsd.edu/homer/ngs/annotation.html |
| deepTools (v2.5.0) | Ramirez et al., 2016 | http://homer.ucsd.edu/homer/ngs/annotation.html |
| hclust | Müllner, 2013 | http://danifold.net/fastcluster.html |
| pheatmap | R Core Team, 2016 | https://cran.r-project.org/web/packages/pheatmap/index.html |

## LEAD CONTACT AND MATERIALS AVAILABILITY

Further information and requests for resources and reagents should be directed to and will be fulfilled by the Lead Contact, Dr. Ping Mu (ping.mu@utsouthwestern.edu). All cell lines, plasmids and other reagents generated in this study are available from the Lead Contact with a completed Materials Transfer Agreement if there is potential for commercial application.

## EXPERIMENTAL MODEL AND SUBJECT DETAIL

### SCID Mouse *In Vivo* Xenografts

All animal experiments were performed in compliance with the guidelines of the Animal Resource Center of UT Southwestern and Research Animal Resource Center of the MSKCC. LNCaP/AR *in vivo* xenograft experiments were conducted by subcutaneous injection of 2 × $10^6$ LNCaP/AR cells (100 μl in 50% Matrigel, BD Biosciences, and 50% growth media) into the flanks of castrated male SCID mice on both sides. Daily gavage treatment with 10 mg/kg enzalutamide or vehicle (1% carboxymethyl cellulose, 0.1% Tween 80, 5% DMSO) was initiated one day after the injection. Once tumors were noticeable, tumor size was measured weekly by tumor measuring system Peira TM900 (Peira bvba, Belgium). For CWR22Pc *in vivo* experiments (Figures S3E and S3F), 2 × $10^6$ CWR22Pc cells were injected subcutaneously into the flanks of intact male SCID mice and both castration and enzalutamide treatment (10 mg/kg) was initiated on day 27 of xenografting. For *in vivo* experiment in Figures S8F and S8G, 10 mg/kg enzalutamide and/or 60 mg/kg CPI-0610 were given after 5 weeks of enzalutamide alone administration, when tumors were around 200 $mm^3$ size in average. CPI-0610 and JQ1 are commercially available from Selleck Chemicals, details listed in Key Resources Table.

### Human Prostate Cancer Cell Lines and Mouse Organoids

LNCaP/AR, CWR22Pc and LAPC4 prostate cancer cell lines were generated and maintained as previously described(Chen et al., 2003; Klein et al., 1997; Mu et al., 2017). E006AA cells were purchased from Millipore (Sigma-Aldrich) (#SCC102). LNCaP/AR, CWR22Pc and LAPC4 cells were cultured in RPMI medium supplemented with 10% fetal bovine serum (FBS), 1% L-glutamine, 1% penicillin-streptomycin, 1% HEPES, and 1% sodium pyruvate (denoted as normal culture medium). E006AA cells were cultured in DMEM medium supplemented with 10% fetal bovine serum (FBS), 1% L-glutamine, 1% penicillin-streptomycin, 1% HEPES, and 1% sodium pyruvate. LNCaP/AR cells were passaged every 3-5 days at a 1:6 ratio, CWR22Pc cells were passaged every 3-5 days at 1:3 ratio. LAPC4 cells were passed every 5-7 days at 1:2 ratio. E006AA cells were passaged every 3-5 days at 1:5 ratio. When treated with 10 μM enzalutamide LNCaP/AR cells were cultured in RPMI medium supplemented with 10% charcoal-stripped serum (denoted as CSS medium). All of the xenograft tumor-derived LNCaP/AR subsequent cell lines were developed from different individual tumors (treatment details as described in main text) that were harvested, disaggregated with collagenase treatments, and then maintained in normal culture medium. After harvesting, cells were cultured on Poly-D-Lysine-coated plates with 2 μg/ml puromycin (Gibco #A1113803) until confluence and were then maintained on standard tissue culture dishes. All cell cultures were assessed for mycoplasma monthly via the highly sensitive MycoAlert$^{TM}$ PLUS Mycoplasma Detection kit from Lonza (Cat #LT07-710). Cell line identification was validated each year through the human STR profiling cell authentication provided by the UT Southwestern genomic sequencing core and compared to ATCC cell line profiles. *Pten*$^{-/-}$ mouse organoids were generated from Pb-Cre4-*Pten*$^{flox/flox}$ mice as previously described (Chen et al., 2013). This organoid (218-5A) is cultured in 3D Matrigel according to established protocol (Karthaus et al., 2014). This organoid is split at 1:3 ratio every 6 days by trypsin or sterile glass pipette.

### shRNA and CRISPR Model Generation

Lentiviral or retroviral transduction of cells for shRNA or guide RNA experiments was performed as previously described with some modifications (Mu et al., 2017; Wheeler et al., 2015). Specifically, retroviral virus was used for shRNA library transduction in Figure 1, as well as shCHD1 KD in Figures 3E, 8A, 8C, 8D, and S2A–S2E. Lentiviral virus was used for CRISPR based KO in Figures 3A–3C, 6C, and S1C and inducible or stable shRNA constructs based KD in Figures S2F–S2H, S3, 6D, 8C, and 8D. For the miR-E based shRNA library transduction, LNCaP/AR cells were transduced with pooled retroviral shRNA hairpins with a 5-20% transduction efficiency to ensure that most shRNAs are transduced at single-copy level. Two days after transduction, infected LNCaP/AR cells were selected with 2 μg/ml puromycin for four days to select a pure GFP positive population. Sequences of all the library shRNAs are listed in Table S2. For all other shRNA or CRISPR mediated modifications, unless otherwise noted, cells were seeded at 400,000 cells per well in 2 ml of media in 6-well plates. The next day, media was replaced with media containing 50% of virus and 50% of fresh culture medium, along with 5 μg/ml polybrene. The lentiviral or retroviral virus containing media was removed after 24 hours and replaced with regular culture medium. Three days post transduction, the cells were selected with 2 μg/ml puromycin for 4 days or 5 μg/ml blasticidin, as described below. The backbones and sequences of all the shRNAs and CRISPR guide RNAs are listed in the Method Details and Key Resources Table.

## METHOD DETAILS

### Generation of the Human PCa Deletome and Construction of the miR-E shRNA Library

To define a comprehensive human prostate cancer deletome, we developed an integrative pipeline to analyze the genomic copy number alterations (CNV) and mRNA expression data from multiple independent genomic studies. First, we examined the original CNV data of the 2010 Taylor dataset and filtered the list of deleted genes present in regions of recurrent focal and chromosome arm length deletion in more than 15% of the prostate cancer patients (generated 2 lists based on either the published CNV or the R.A.E. output) (Taylor et al., 2008; 2010). Then we integrated these CNV data and the corresponding gene expression data to further filtered the recurrent deletion events that are associated with decreased gene expression based on matched gene expression data. In parallel, we utilized this pipeline analysis for another three independent genomic studies and generated 4 additional deleted gene lists, including the 2012 Barbieri dataset, the 2012 Grasso dataset (2 lists based on either the published CNV or the R.A.E. output) and the TCGA dataset (Barbieri et al., 2012; Grasso et al., 2012; Network, 2015). Two more deleted gene lists were generated using similar approaches as our integrative pipeline and therefore added into our final 8 deleted gene lists, including the 2007 Kim dataset and the 2009 Holcomb dataset(Holcomb et al., 2009; Kim et al., 2007). As expected, these 8 deleted gene lists substantially overlap. We then combined the 8 deleted gene lists and refined the final human PCa deletome of 730 genes by only incorporating the genes whose deletion were confirmed by at least two independent studies (Table S1) (Two genes *PTEN* and *DACH1* were removed from the list because they were already deleted in LNCaP/AR cells) (Taylor et al., 2010). To identify genes whose protein product inhibition can confer resistance to antiandrogen therapy in prostate cancer, we built a custom shRNA library targeting 730 genes (5-6 shRNAs/gene, total 4234 shRNAs) (Table S2). The shRNAs were cloned in a LEPC (aka MLP-E) vector, a constitutive expression vector that was previously optimized for more efficient knockdown, by PCR-cloning a pool of oligonucleotides synthesized on 12k customized arrays (CustomArrays) as previously described (Zuber et al., 2010). The shRNAs were designed using an algorithm that predicts potent shRNAs as previously described (Pelossof et al., 2017). The library was subcloned into 43 independent pools each pool consisting of ~100 shRNAs, to ensure that shRNA representation was not lost after grafting the tumors cells *in vivo*.

### *In Vivo* shRNA Mediated Screen and HiSeq

Each pool of the library was transduced into human CRPC tumor cell line LNCaP/AR at low multiplicity of infection (MOI < 1), to ensure a single retroviral integration per cell and achieving a representation of each shRNA in an average of 20,000 cells. Transduced LNCaP/AR cells were selected for 4 days using 2 μg/ml puromycin (Invitrogen) and 2 million cells were subcutaneously injected bilaterally into 5 castrated SCID mice to preserve library representation throughout the experiment (because of unexpected mice loss, we have added additional mice in several pools to get enough tumors). As a negative control group, LNCaP/AR cells transduced with shNT were also injected into 10 castrated mice. All animals were treated with enzalutamide (10 mg/kg/day) one day after the day of bilateral injection to mimic the clinical scenario of enzalutamide usage, with the exception of 5 mice in the negative control group being treated with vehicle. As described in the main text, based on the results of pilot experiments (Figures S1A and S1B), we only harvested the tumors that reached 100 $mm^3$ burden by week 16, before the appearance of background tumors (which usually require more than ~19 weeks to arise) based on the rationale that the shRNAs targeting candidate resistance biomarkers should confer resistance significantly quicker than the stochastic enrichment of the tumor initiating cells (“jackpot effect”).

Genomic DNA from plasmids, pregrafts, and resistant tumors was isolated by two rounds of phenol extraction using Phase-Lock tubes (5prime) followed by isopropanol precipitation. The normalized reads of all shRNAs present in resistant tumors or starting materials were quantified using HiSeq 2500 sequencing of shRNA guide strands PCR amplified from the isolated genomic DNA, as previously described (Zuber et al., 2010; 2011). Sequence processing was performed using a customized Galaxy platform as previously described (Zuber et al., 2011). For each shRNA and condition, the number of matching reads was normalized to the total number of library-specific reads per lane (10 million total reads per pool) and used for further analysis. We only obtained 21 pools of reads in pregrafts therefore reads in plasmids were used as starting material instead. All the HiSeq sequencing results (FASTQ) and normalized reads files were deposited to GEO: GSE127957. To adapt a probabilistic ranking algorithm RIGER-E (RNAi Gene Enrichment Ranking) to analyze the HiSeq results, we recorded the hairpin reads in the tumors which did not score by week 16 as “0” because they failed to enrich quicker than stochastically enriched hairpins, in order to have a working matrix for a probabilistic statistic model. RIGER analysis was performed as previously described (Golden et al., 2017) and the data matrix was deposited to GEO: GSE127957. We then applied two additional cut-offs to further filter out the false positive candidate genes. We chose ‘‘enriched in more than 8% of total tumor xenografted’’ as a first cut-off based on the stochastic enrichment ratio of negative control gene *TBC1D4*. We chose ‘‘4 out of 6 hairpins enriched’’ as the second cut-off based on a triangle thresholding method (Zack et al., 1977) and the results of our pilot experiments. The enrichment of each shRNAs was determined by comparing the normalized reads in the resistant tumors with the normalized reads in plasmids.

## Individual Plasmid Construction and Virus Production

The retroviral (LEPG) and lentiviral (SGEP, LT3GEPIR) miR-E based expression vectors generous gifts from Dr. Johannes Zuber (Research Institute of Molecular Pathology, Vienna, Austria), and described previously(Zuber et al., 2011). LEPC, SCEP and LT3CEPIR vectors were constructed by switching the GFP cassette in the previous three vectors with a mCherry cassette as described previously (Mu et al., 2017).

The sequences of shRNA hairpins are listed below:

LEPG-shNT:

TGCTGTTGACAGTGAGCGCAGGAATTATAATGCTTATCTATAGTGAAGCCACAGATGTATAGATAAGCATTATAATTCCTATGCCTACTGCCTCGGA

*LEPG-shCHD1-1*:

TGCTGTTGACAGTGAGCGACAGGTTAACATTTTAGATAAATAGTGAAGCCACAGATGTATTTATCTAAAATGTTAACCTGGTGCCTACTGCCTCGGACTTCAAGGGGCTAGAATTC

*LEPG-shCHD1-2*:

TGCTGTTGACAGTGAGCGACAGGAAATGGATATAGATGAATAGTGAAGCCACAGATGTATTCATCTATATCCATTTCCTGGTGCCTACTGCCTCGGACTTCAAGGGGCTAGAATTC

LEPG-shCHD1-3:

TGCTGTTGACAGTGAGCGCAACGTTATATATGACAAATTATAGTGAAGCCACAGATGTATAATTTGTCATATATAACGTTTTGCCTACTGCCTCGGACTTCAAGGGGCTAGAATTC

LEPG-shCHD1-4:

TGCTGTTGACAGTGAGCGACAGGAGAGATTCAGTATTTAATAGTGAAGCCACAGATGTATTAAATACTGAATCTCTCCTGGTGCCTACTGCCTCGGACTTCAAGGGGCTAGAATTC

LEPG-shCHD1-5:

TGCTGTTGACAGTGAGCGCTAGGCGGTTTATCAAGAGCTATAGTGAAGCCACAGATGTATAGCTCTTGATAAACCGCCTAATGCCTACTGCCTCGGACTTCAAGGGGCTAGAATTC

LT3CEPIR-shGR-1:

TGCTGTTGACAGTGAGCGCCCAAAGCAGTTTCACTCTCAATAGTGAAGCCACAGATGTATTGAGAGTGAAACTGCTTTGGATGCCTACTGCCTCGGA

LT3CEPIR-shGR-2:

TGCTGTTGACAGTGAGCGAAAGCTGTAAAGTTTTCTTCAATAGTGAAGCCACAGATGTATTGAAGAAAACTTTACAGCTTCTGCCTACTGCCTCGGA

LT3CEPIR-shCHD1-1:

TGCTGTTGACAGTGAGCGACAGGTTAACATTTTAGATAAATAGTGAAGCCACAGATGTATTTATCTAAAATGTTAACCTGGTGCCTACTGCCTCGGACTTCAAGGGGCTAGAATTC

LT3CEPIR-shCHD1-2:

TGCTGTTGACAGTGAGCGACAGGAAATGGATATAGATGAATAGTGAAGCCACAGATGTATTCATCTATATCCATTTCCTGGTGCCTACTGCCTCGGACTTCAAGGGGCTAGAATTC

The All-In-One lentiCRISPR v2 purchased from Addgene (Plasmid #52961) was used to generate the sgCHD1, sgmChd1(for mouse organoid experiment) and sgPTEN constructs. The empty vector served as the sgNT control. The guide RNAs were designed using the online CRISPR designing tool at Benchling (https://benchling.com).

The sequences of sgRNAs are listed below:

lentiCRISPRv2-sgCHD1-1-F: CACCGTCAGCTCCATCAACTTTCGG
lentiCRISPRv2-sgCHD1-1-R: AAACCCGAAAGTTGATGGAGCTGAC
lentiCRISPRv2-sgCHD1-2-F: CACCGGATTTATGGATTGTCGGATT
lentiCRISPRv2-sgCHD1-2-R: AAACAATCCGACAATCCATAAATCC
lentiCRISPRv2-sgmChd1-1-F: CACCGAAAGTGTTAGAAATGGCAG
lentiCRISPRv2-sgmChd1-1-R: AAACCTGCCATTTCTAACACTTTC
lentiCRISPRv2-sgmChd1-2-F: CACCGCAACATTCACGGGTTTCCTG
lentiCRISPRv2-sgmChd1-2-R: AAACCAGGAAACCCGTGAATGTTGC
lentiCRISPRv2-sgPTEN-F: CACCGAAACAAAAGGAGATATCAAG
lentiCRISPRv2-sgPTEN-R: AAACCTTGATATCTCCTTTTGTTTC

All information related to constructs used for CRISPR function screening are discussed below in the functional screening section.

The *CHD1* expressing vectors pCDH-EF1-Chd1-T2A-copGFP and pCDH-EF1-Chd1-P2A-puro were generous gift from Dr. Ping Chi’s laboratory at MSKCC.

## FACS-Based Growth Competition Assay

LNCaP/AR cells were transduced with 5 different shRNAs targeting *CHD1* or shNT individually with a viral infection efficiency of ~20%, verified by GFP percentage by FACS. The competition cell mixture of ~20% transduced LNCaP/AR cells and ~80% wild-type cells was treated with 10 μM enzalutamide and the percentage of GFP positive cells were measured by FACS on day 0, day 6, day 12, day 17 and day 24. Relative cell number fold change was calculated as follows:
$\frac{T2\times Y}{T1\times X}\div\frac{T2\times(1-Y)}{T1\times(1-X)}=\frac{Y\times(1-X)}{X\times(1-Y)}$, where T1 is the total cell number of cell mixture on day 0 and T2 is the total cell number on day 6, 12,17, or 24; X is the percentage of GFP positive cells measured on day 0 and Y is the percentage of GFP positive cells measured on day 6,12,17, or 24; then 1-X is the percentage of wild-type uninfected cells on day 0 and 1-Y is the percentage of wild-type uninfected cells on day 6, 12, 17 or 24. FACS-based competition assay in Figures 8C and S8D is analogous to the one in Figures 3D and 3E described above, except the shCHD1-XE-1 cells transduced with LT3CEPIR-shGRs were treated with doxycycline for 48 hours at 250 ng/ml before the day 0 was measured.

## Cell Growth Assay, Cell Viability Assays and Dose Response Curve

LNCaP/AR cells transduced with CRISPR/sgRNAs were seeded at 20,000 cells per well in a 24-well cell culture plate, in CSS medium and treated with enzalutamide (10 μM) or vehicle (DMSO) for 6 days. Cell numbers were counted using a Countess II FL automatic cell counter (Invitrogen) on day 7 and the relative cell growth (Enz/DMSO) was calculated. Cell growth assays were conducted in triplicate and mean ± SEM were reported. Dose response curve and all other cell viability assays were measured by CellTiter-Glo luminescent cell viability assay (Promega cat #7570). 4000 LNCaP/AR cells were seeded in 96-well dish and treated with different dosages of enzalutamide for 3 days before performing the assay. 3000 CWR22Pc cells were seeded in 96-well plate and treated with different dosages of enzalutamide for 6 days before performing the assay. 5000 LAPC4 cells were seeded in 96-well plate with different dosages of enzalutamide for 12 days before perform the assay. 500 E006AA cells were seeded in 3D Matrigel in human organoid media (Gao et al., 2014; Karthaus et al., 2014) with enzalutamide for 6 days, because E006AA cells are not very sensitive to enzalutamide treatment in 2D culture condition. Mouse organoid were seeded in 3D Matrigel (1000 cells/per 50 μl sphere) in mouse organoid media (Karthaus et al., 2014) with 1 μM enzalutamide for 6 days before the cell viability was read.

## Gene Expression Assay by qPCR

Total RNA from cells or homogenized tissues was extracted using Trizol (Ambion, Cat 15596018) following manufacturer's instructions. cDNA was made using the SuperScript™ IV VILO™ Master Mix with ezDNase™ Enzyme (Thermo Fisher, 11766500) following manufacturer's instructions, with 200 ng/μl RNA template. 2X PowerUp™ SYBR™ Green Master Mix (Thermo Fisher, A25778) was used in the amplification of the cDNA. Assays were performed in triplicate and normalized to endogenous β-Actin expression. Heatmaps represent the gene expression difference were generated by prism 8, using the log10 of expression fold change compared to control cell lines (shNT or sgNT transduced LNCaP/AR). Qiagen RT2 qPCR primer assays are used as primers for gene expression detection, unless otherwise noted. Individual primer assays are listed, as well as in Table S6.

AR, Qiagen RT2, Cat# PPH01016A
*KLK3*, Qiagen RT2, Cat# PPH01002B
*NKX3-1*, Qiagen RT2, Cat# PPH02267C
*TMPRSS2*, Qiagen RT2, Cat# PPH02262C
*NDRG1*, Qiagen RT2, Cat# PPH02202B
*NR3C1* (GR), Qiagen RT2, Cat# PPH02652A
*TBX2*, Origene, F-AGCAGTGGATGGCTAAGCCTGT
R-GGATGTCGTTGGCTCGCACTAT
*NR2F1*, Origene, F-TGCCTCAAAGCCATCGTGCTGT
R-CAGCAGCAGTTTGCCAAAACGG
*POU3F2*, Origene, F-GTGTTCTCGCAGACCACCATCT
R-GCTGCGATCTTGTCTATGCTCG
*SGK1*, Qiagen RT2, Cat# PPH00387F
*NPC1*, Sigma KiCqStart, Cat#H_NPC1_1, 4864
*KRT8*, Qiagen RT2, Cat# PPH02214F
*KRT18*, Qiagen RT2, Cat# PPH00452F
*KRT5*, Qiagen RT2, Cat# PPH02625F
*KRT14*, Qiagen RT2, Cat# PPH02389A
*TP63*, Qiagen RT2, Cat# PPH01032F
*SYP*, Qiagen RT2, Cat# PPH00717A
*CHGA*, Qiagen RT2, Cat# PPH01181A
*ENO2*, Qiagen RT2, Cat# PPH02058A
*SOX2*, Qiagen RT2, Cat# PPH02471A

Please cite this article in press as: Zhang et al., Loss of *CHD1* Promotes Heterogeneous Mechanisms of Resistance to AR-Targeted Therapy via Chromatin Dysregulation, Cancer Cell (2020), https://doi.org/10.1016/j.ccell.2020.03.001

*SNAI2*, Qiagen RT2, Cat# PPH02475A
*TWIST1*, Qiagen RT2, Cat# PPH02132A
*SNAI1*, Qiagen RT2, Cat# PPH02459B
*ZEB1*, Qiagen RT2, Cat# PPH01922A
*CDH2*, Qiagen RT2, Cat# PPH00636F

## Western Blot

Proteins were extracted from whole cell lysate using RIPA buffer. Proteins were then measured with Pierce BCA Protein Assay Kit (cat #23225) following manufacturer's instructions. Protein lyses were mixed with 5X laemmli buffer and boiled at 95°C for 5 minutes. Proteins were run on the NuPAGE 4-12% Bis-Tris gels (Invitrogen, Cat #NP0323) using Novex sharp pre-stained protein standards as a marker (Invitrogen, LC8500) and 1X NuPAGE MES SDS buffer as running buffer (Novex, Cat #NP0002) and run at 120 volts. Gels were transferred in 1X Bolt Transfer buffer (Novex, Cat #BT00061) diluted with water and ethanol. Nitrocellulose membrane paper (Immobilon, Cat#IPVH00010) was used and was activated with 100% methanol (Fisher, Cat#A412-20). Transfer was conducted at 4°C for 1 hour at 100 volts. Membranes were blocked in 5% non-fat milk for 15 minutes prior to addition of primary antibody and washed with 1X TBST (10X stock from Teknova, T9511).

Antibodies used for western blot are (also listed in Key Resources Table):

(1) CHD1 (D8C2) Rabbit mAb, Cell Signaling, Cat #4351
(2) AR Antibody (N-20), Santa Cruz, sc-816
(3) KLK3 (D6B1) XP® Rabbit mAb, Cell Signaling, Cat # 5365
(4) PMEPA1 Antibody (P-15), Santa Cruz, Cat # sc-85829
(5) STEAP Antibody (B-4), Santa Cruz, Cat # sc-271872
(6) β-Actin (13E5) Rabbit mAb, Cell Signaling, Cat # 4970
(7) Glucocorticoid Receptor (D6H2L) XP® Rabbit mAb, Cell Signaling, Cat #12041
(8) SGK1 (D27C11) Rabbit mAb, Cell Signaling, Cat #12103
(9) c-Myc (D84C12) Rabbit mAb, Cell Signaling, Cat #5605

## Immunofluorescence (IF)

LNCaP/AR cells were seeded on round glass coverslips. After 24 hr, cells were washed with PBS and fixed with 4% paraformaldehyde for 20 min at room temperature, followed by permeabilization with 0.5% Triton X-100 for 5 min. Then cells were incubated with primary antibodies (Rabbit anti-GR, CST, #12041; mouse anti-NR2F1 R&D, PP-H8132-00), overnight at 4°C after blocking with 3% BSA/PBS for 30 min at room temperature, followed by incubation with Alexa Fluor-labeled secondary antibodies (Alexa Fluor® 488 AffiniPure Goat Anti-Mouse IgG (H+L), Jackson Immunoresearch; Alexa Fluor® 594 AffiniPure Goat Anti-Rabbit IgG (H+L), Jackson Immunoresearch) for 1hr at room temperature. Nuclei were stained with DAPI. Images were acquired on Leica DMi8 microscope and Zeiss LSM 700 confocal Laser Scanning Microscope. Three biological replicated, representative images of each cell line were used to quantify the fluorescence intensity of GR and NR2F1 signals, using imageJ.

## Immunohistochemistry (IHC)

Tumors were fixed in 4% paraformaldehyde overnight at 4°C. Then tumors were embedded in paraffin and sectioned at 5 μm. Immunohistochemistry was performed following standard procedures. After incubated with primary antibodies (Rabbit anti-GR, CST, #12041; mouse anti-NR2F1 R&D, PP-H8132-00), VECTASTAIN® ABC HRP Kit (Peroxidase, Rabbit IgG) and HRP conjugated Goat anti-mouse IgG were used, followed by ImmPACT® DAB Peroxidase (HRP) Substrate. Images were acquired on ECHO revolve microscope. Representative images of four tumors of each group were used to quantify the IHC signals of GR and NR2F1, using imageJ and the IHC Profiler plugin (Varghese et al., 2014).

## FACS-based Functional Screen Mediated by CRISPR/Cas9

LNCaP/AR-shCHD1 cells (GFP positive) were transduced with lentiCas9-Blast purchased from Addgene (Plasmid #52962) and then selected with 5 μg/ml blasticidin (Gibco #A1113903) for 5 days. Four individual guide RNAs were designed to target each of the top 22 candidate TFs using the online CRISPR designing tool at Benchling (https://benchling.com). The sequences of sgRNAs can be found in Table S5. These guide RNAs were individually cloned into pLKO5.sgRNA.EFS.tRFP purchased from Addgene (Plasmid #57823). Then the LNCaP/AR-shCHD1-Cas9-Blast cells were transduced with these guide RNAs (guide RNAs targeting the same TF were pooled together) or sgNT with a viral infection efficiency of 50-90%, as measured by percentage of RFP positive cells (achieving a cell mixture of RFP positive cells vs RFP negative cells). The transduced cells were treated with 10 μM enzalutamide and the percentage of RFP positive cells were measured by FACS on day 0 and day 7. If deletion of any TF by CRISPR/Cas9 compromised the resistance to enzalutamide, it will give the infected cells with a growth disadvantage that will in turn be reflected by a reduction in the percentage of RFP positive cells.

Please cite this article in press as: Zhang et al., Loss of *CHD1* Promotes Heterogeneous Mechanisms of Resistance to AR-Targeted Therapy via Chromatin Dysregulation, Cancer Cell (2020), https://doi.org/10.1016/j.ccell.2020.03.001

## QUANTIFICATION AND STATISTICAL ANALYSIS

### Statistics Methods

All of the statistical details of experiments can be found in figure legends as well as the Method Details section. For all comparisons between two groups of independent datasets, multiple t tests were performed, p value and standard error of the mean (SEM) were reported. For all comparisons among more than two groups (>2), one-way or two-way ANOVA were performed, p values and SEM were reported; and p values were adjusted by multiple testing corrections (Bonferroni) when applicable. For dose response curve, p values were calculated by non-linear regression with extra sum-of-squares F test. For all figures, **** represents $p<0.0001$. *** represents $p<0.001$. ** represents $p<0.01$. * represents $p<0.05$. The usage of all statistical approaches was examined by our biostatistical collaborators. All bioinformatic analysis and comparisons are described in details below.

### Analysis of Human Prostate Cancer Dataset

Processed 444 SU2C metastatic prostate cancer patient cohort (Abida et al., 2019) RNA-seq data and enzalutamide/abiraterone treatment data were downloaded from cBioPortal (http://www.cbioportal.org/). 128 patients of this cohort with metastatic CRPC have baseline biopsy and matched clinical data. 75 patients of this 128 sub-cohort have gene expression data captured by Poly-A RNA-seq. 56 patients of this 75 sub-cohort have records of time on either enzalutamide/apalutamide or abiraterone. 4 patients of this cohort were excluded because they have *SPOP* mutations, which demonstrate elevated sensitivity to antiandrogen treatment (Boysen et al., 2018). Histogram of *CHD1* mRNA distribution was generated by R Studio (Version 1.1.453). The probability of treatment duration figure was generated by prism 8 using Mantel-Cox test.

The same SU2C cohort (Abida et al., 2019) RNA-seq data was used to analyze expression patterns of 4 TFs (*NR3C1*, *POU3F2*, *NR2F1* and *TBX2*) and their relationship with *CHD1* level. Among these patients, RNA-seq data (Capture platform) for all 5 genes were available for 212 patients. We excluded patients with only polyA RNA-seq data because *NR2F1* expression is not available from the polyA platform. Expression matrix of all 5 genes was analyzed by “hclust” method (Müllner, 2013), with the parameter k-means= 5, scale = “column” (normalized value centered by gene). Unsupervised clustering resulted in 5 distinct groups, using the “pheatmap” package of R (V1.0.12). Each cluster contains different number of tumors (Cluster:1 Size:102, Cluster:2 Size:27, Cluster3: Size:2, Cluster:4 Size:4, Cluster:5, Size:40).

### Sample and library preparation for RNA-seq and ATAC-seq

$1\times10^6$ LNCaP/AR cells was plated in 6-well plate, growing under regular RPMI-1640 containing 10% FBS. After 48 hours, cells were trypsinized and collected by spinning at 500 g for 1.5 min, 4° C. Cells were then washed once with cold 1X PBS and spinned down at 500 g for 1.5 min, 4° C. After discarding supernatant, cells were lysed using 50 μL cold lysis buffer (10 mM Tris-HCl pH 7.4, 10 mM NaCl, 3 mM $MgCl_2$, 0.1% IGEPAL CA-360) and spinned down immediately at 500 g for 10 min, 4 ° C. Total RNA from cells was extracted using Trizol (Ambion, Cat 15596018) following manufacturer’s instructions. RNA-Seq libraries were prepared using the Illumina TruSeq stranded mRNA kit, with 10 cycles of PCR amplification, starting from 500 ng of total RNA, at the Genome Technology Center (GTC) at NYU. Barcoded RNA-Seq were run as single read 50 nucleotides in length on the Illumina HiSeq 2500 (v4 chemistry) and Poly-A selection was performed. For ATAC-seq, $5\times10^5$ LNCaP/AR cells were precipitated and kept on ice and subsequently resuspended in 25 μL 2X TD Buffer (Illumina Nextera kit), 2.5 μL Transposase enzyme (Illumina Nextera kit, 15028252) and 22.5 μL Nuclease-free water in a total of 50 μL reaction for 1 hr at 37° C. DNA was then purified using Qiagen MinElute PCR purification kit (28004) in a final volume of 10 μL. ATAC-Seq- Libraries were prepared following the Buenrostro protocol (https://www.ncbi.nlm.nih.gov/pmc/articles/PMC4374986/) and ATAC-Seq libraries were sequenced as 50 base paired-end reads on the Illumina HiSeq 4000 at the Genome Technology Center (GTC) at NYU.

### Analysis of RNA-seq Data

Reads with Phred quality scores less than 20 and less than 35 bp after trimming were removed from further analysis using trimgalore (v0.4.1) (Martin, 2011). Quality-filtered reads were then aligned to the human reference genome GRCh38 using the HISAT (v2.0.1) (Pertea et al., 2016) aligner with default settings and marked duplicates using Sambamba (v0.6.6) (Tarasov et al., 2015). Aligned reads were quantified using featureCounts (v1.4.6) (Liao et al., 2014) per gene ID against GENCODE v10 GRCh38.p10 (Mudge and Harrow, 2015). Differential gene expression analysis was performed using the R package DEseq2 (v1.6.3) (Love et al., 2014). Cutoff values of absolute fold change greater than 2 and FDR<0.1 were used to select for differentially expressed genes between sample group comparisons. All RNA-seq data have been deposited in the Sequence Read Archive (SRA) with the accession numbers GSE126917, also listed in Key Resources Table.

### GO Analysis

GeneOntology Enrichment Pathway analysis was performed using PANTHER to determine molecular and biological functional categories which were enriched in CHD1-depelted cells (Mu et al., 2017). The input gene lists were generated from the overlapping of differentially expressed genes in four compilations (shCHD1-1 compared to shNT, shCHD1-2 compared to shNT, shCHD1-XE-1 compared to shNT, shCHD1-XE-2 compared to shNT), which consistence of 150 genes in total. Cutoff values of FDR<0.05 was used to select top enriched pathways. To avoid pathways with too few genes, we excluded the gene lists with less than 10 hits changed in our datasets.

### GSEA Analysis

GSEA statistical analysis was carried out with publicly available software from the Broad Institute (http://www.broadinstitute.org/gsea/index.jsp). Weighted GSEA enrichment statistic and Signal2Noise metric for ranking genes were used. The AR selective gene score was calculated by the sum of RPKM of all genes in the AR selective gene list as previously defined (Arora et al., 2013).

### Analysis of ATAC-seq Data

We utilized trimgalore (v0.4.1) (Martin, 2011) for the raw reads to remove reads shorter than 35 bp or with Phred quality scores less than 20 and then aligned those trimmed reads to the human reference genome (GRCh38) using default parameters in BWA (v0.7.12) (Li and Durbin, 2009). The aligned reads were subsequently filtered for quality and uniquely mappable reads were retained for further analysis using Samtools (v1.3) (Li et al., 2009) and Sambamba (v0.6.6) (Tarasov et al., 2015). Library complexity was measured using BEDTools (v2.26.0) (Quinlan and Hall, 2010) and meets ENCODE data quality standards (Landt et al., 2012). Relaxed peaks were called using MACS (v2.1.0) (Feng et al., 2012) with a p value of $1x10^{-2}$. Consensus peaks were calculated by taking the overlap of peaks for sample, its replicates, and pseudoreplicates. All ATAC-seq data have been deposited in the Sequence Read Archive (SRA) with the accession numbers GSE127241, also listed in Key Resources Table.

### Differential Binding Analysis

To detect differentially bound sites, we used R (v3.3.2) and package DiffBind (v2.2.12) (Stark and Brown, 2011; R Core Team, 2016) Default parameters were used in DiffBind workflow. To identify overlapping peaks between conditions we used BEDtools (v2.26.0), using intersect (Quinlan and Hall, 2010).

### ATAC-seq Differential Peak and RNA-Seq Fold Change CDF Plots

We filtered the above annotated differential peak data for peak locations having fold changes of greater than 2 and greater than 5 separately, with associated p values of 0.01 or less. We then took the gene name from these filtered peak annotations and plotted the cumulative distribution of the gene's RNA-seq differential expression log2 fold change values against the cumulative distribution of the log2 expression fold change of all genes.

### Annotation and Differential Motif Detection

To identify motif presence in peaks, we created a list of possible binding sites across the human reference (GRCh38) genome of motifs obtained from the JASPAR 2018 core vertebrate non-redundant database using the *fimo* command from the MEME suite (v4.11.1) (Bailey et al., 2015; Khan et al., 2017). We then performed differential motif analysis using DAStk (v0.1.5) on ATAC-seq peaks (Tripodi et al., 2018). ATAC-seq peaks were annotated using the annotatePeaks. script in HOMER (v4.9) (Heinz et al., 2010).

### Predicting Driver TFs Using RNA-seq and ATAC-seq Data

We developed a workflow (Barnes et al., 2019) that combines RNA-seq and ATAC-seq data with TF motif information to predict driver TFs in prostate cancer resistance, similar as the method as previously described (Franco et al., 2018).

Transcription Factor Expression using RNA-seq: For each cell line (2 shCHD1-XE lines and two shCHD1 lines) we calculated the RNA-Score as the RNA-seq log2 fold change values compared to shNT cells.

Motif Predictions using ATAC-seq: For each cell line (2 shCHD1-XE lines and two shCHD1 lines) we calculated the ATAC-seq from the DAStk derived motif differential scores.

Determining driver Transcription Factors: To avoid having results from one of the four cell lines dominate the entire analysis, a weight $\gamma$ was first calculated for each group by dividing the sum of the absolute value shCHD1-XE RNA-seq fold change values by the sum of the absolute value of shCHD1 RNA-Scores. A $\gamma$ was also calculated for ATAC-Scores by dividing the sum of shCHD1-XE motif differential scores by the sum of shCHD1 ATAC-Scores, as shown in this equation: $\gamma = \frac{\sum |\mathrm{shCHD1-XEs}|}{\sum |\mathrm{shCHD1s}|}$. RNA fold change values and motif differential Scores were then multiplied by the respective weights, and then summed to create overall RNA-Scores and ATAC-Scores, respectively (Table S5). Then a Combined-Score is calculated by multiplying the overall RNA-Score and ATAC-Score.

If the TF has both negative value of RNA-Score and ATAC-Score, the Combined-Score was multiplied by -1 to get the adjusted Combined-Score. Furthermore, because some TFs may upregulate the downstream signaling pathway without significant changes in chromatin accessibility, or upregulate the downstream signaling pathway with only changes in chromatin accessibility, the Combined-Score of TFs with top 12 RNA-Scores and/or top 5 ATAC-Scores was also multiplied by -1 if it was a negative value (cut-off was picked based on the previously known function of these TFs). Then all the TFs are ranked using the adjusted Combined-Score (Figure 5H). The top 20 TFs with highest adjusted Combined-Score plus the 2 TFs with highest ATAC-Score are selected as final candidate resistant drivers for further functional screen.

Please cite this article in press as: Zhang et al., Loss of *CHD1* Promotes Heterogeneous Mechanisms of Resistance to AR-Targeted Therapy via Chromatin Dysregulation, Cancer Cell (2020), https://doi.org/10.1016/j.ccell.2020.03.001

### Generating Density Heatmaps and Profiles

For heatmaps and profiles, we used deepTools (v2.5.0) (Ramírez et al., 2016) to generate read abundance from all datasets around peak center (± 2.5 kb/ 2.0 kb), using ‘computeMatrix’. These matrices were then used to create heatmaps and profiles, using deepTools commands ‘plotHeatmap’ or ‘plotProfile’ respectively.

## DATA AND CODE AVAILABILITY

Library shRNA HiSeq data has been deposited in GEO: GSE127957. RNA-Seq data has been deposited in GEO: GSE126917. ATAC-Seq data has been deposited in GEO: GSE127241.

Cancer Cell, Volume *37*

## Supplemental Information

# Loss of *CHD1* Promotes Heterogeneous Mechanisms of Resistance to AR-Targeted Therapy via Chromatin Dysregulation

**Zeda Zhang, Chuanli Zhou, Xiaoling Li, Spencer D. Barnes, Su Deng, Elizabeth Hoover, Chi-Chao Chen, Young Sun Lee, Yanxiao Zhang, Choushi Wang, Lauren A. Metang, Chao Wu, Carla Rodriguez Tirado, Nickolas A. Johnson, John Wongvipat, Kristina Navrazhina, Zhen Cao, Danielle Choi, Chun-Hao Huang, Eliot Linton, Xiaoping Chen, Yupu Liang, Christopher E. Mason, Elisa de Stanchina, Wassim Abida, Amaia Lujambio, Sheng Li, Scott W. Lowe, Joshua T. Mendell, Venkat S. Malladi, Charles L. Sawyers, and Ping Mu**

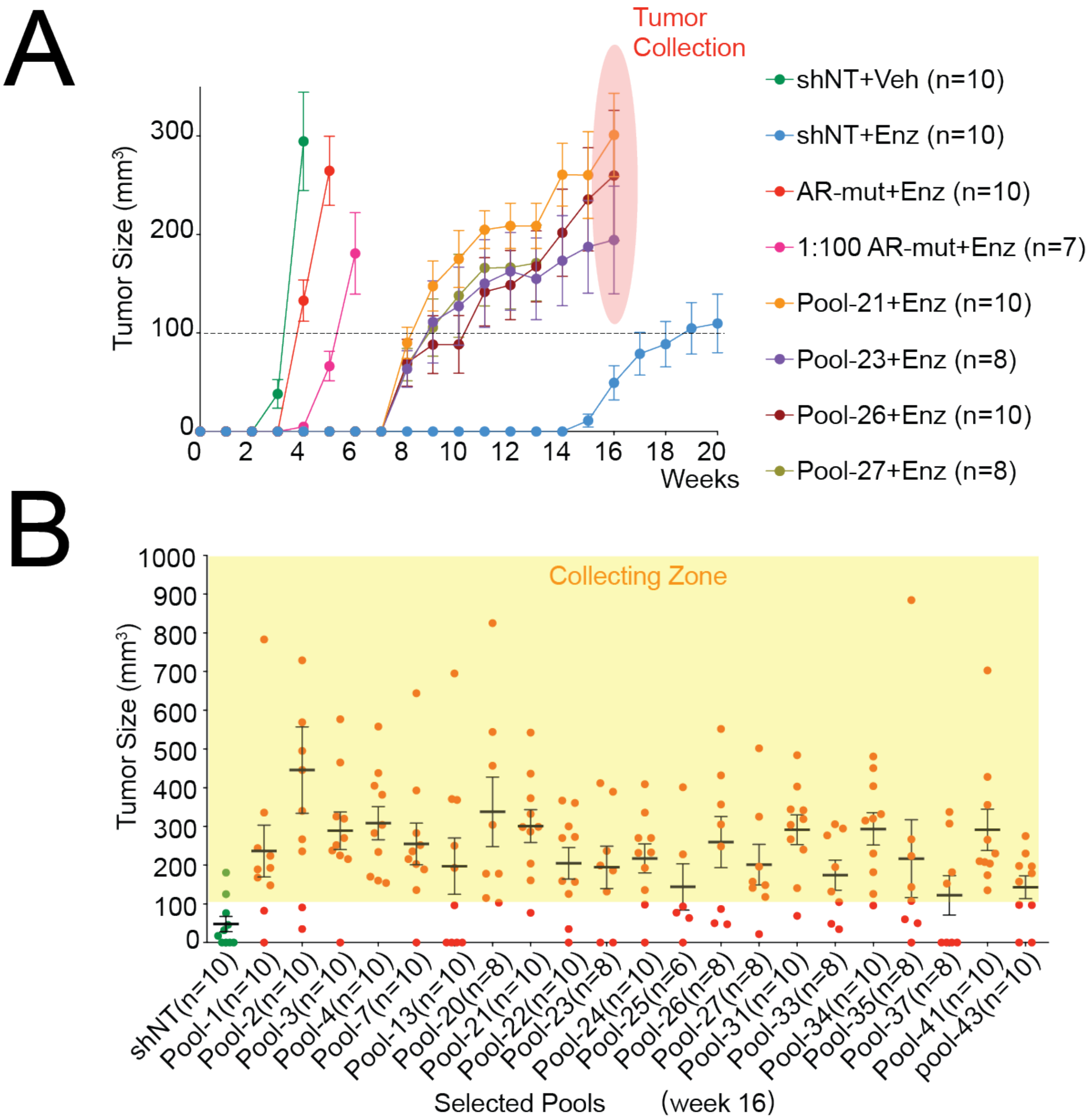

**Figure S1 related to Figure 1. Pilot experiments and the validation of other two top hits emerged from the *in vivo* library screen.** (A) Tumor growth curve of xenografted LNCaP/AR cells transduced with annotated plasmids or pools of library. Enz denotes enzalutamide treatment at 10 mg/kg orally one day after grafting. Veh denotes 0.5% CMC + 0.1% Tween 80 treatment at same dosage. (B) Tumor measurement of xenografted LNCaP/AR cells transduced with shNT and 21 representative pools at week 16. For all panels unless otherwise noted, mean ± SEM. is represented.

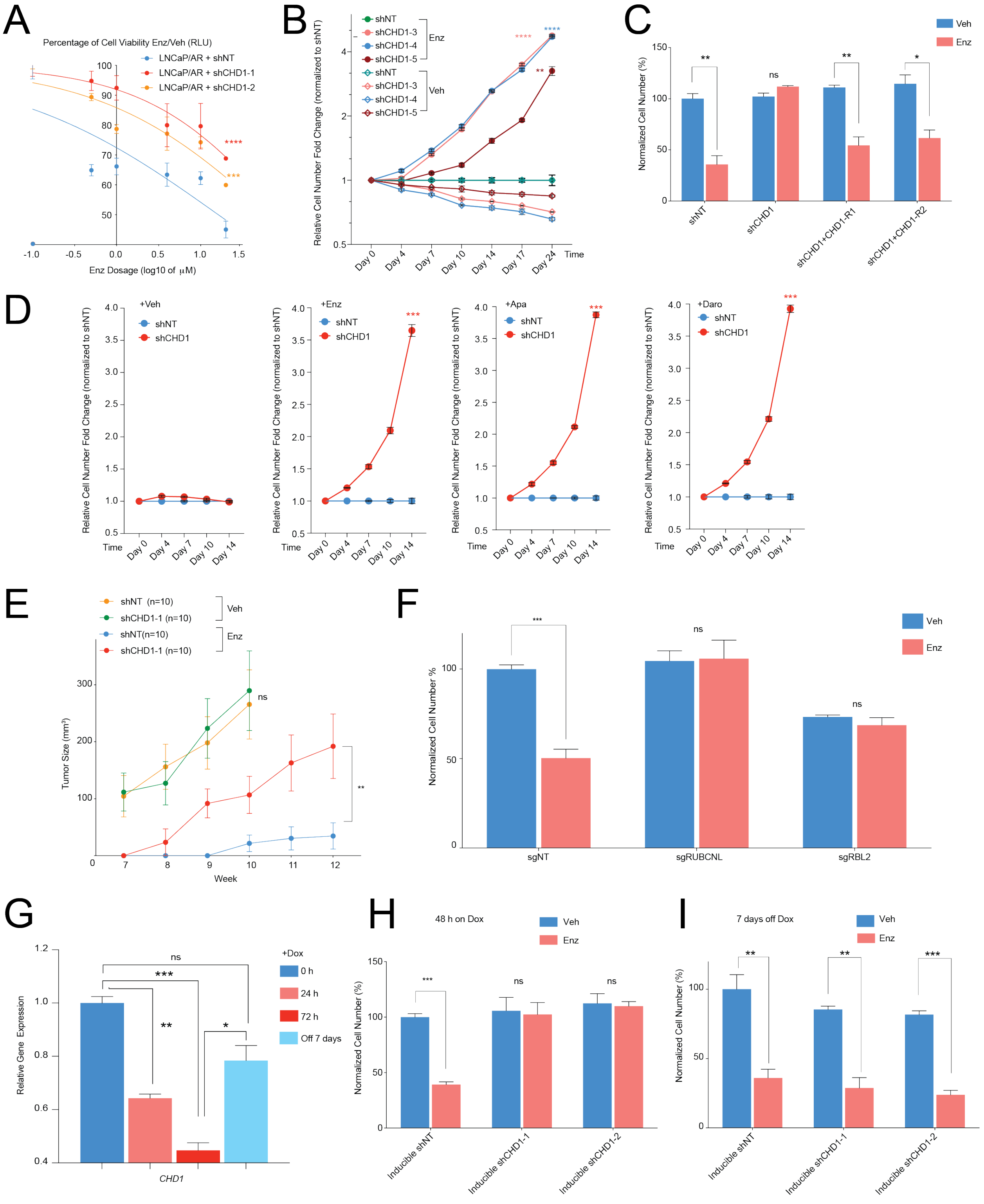

**Figure S2 related to Figure 3. Resistance conferred by *CHD1* KD is reversible.** (A) Dose response curve of LNCaP/AR cells transduced with annotated shRNAs. Mean ± SEM is represented, and p values were calculated by non-linear regression with extra sun-of-squares F test, 3 biological replicates were used for each data point. (B) Relative cell number fold change compared to shNT group, based on the results of FACS-based competition assay. Enz denotes enzalutamide of 10 µM and Veh denotes DMSO. Mean ± SEM is represented, and p values were calculated using two-way ANOVA, 3 biological replicates in each group. (C) Relative cell number of LNCaP/AR cells transduced with annotated shRNAs and rescue plasmids expressing CHD1 cDNA (R1/R2), normalized to shNT+Veh group. Cells were treated with 10 µM enzalutamide (Enz) or DMSO (Veh) for 7 days and cell numbers were counted. Mean ± SEM is represented, and p values were calculated using multiple t tests, 3 biological replicates in each group. (D) Relative cell number fold change compared to shNT group, based on the results of competition assay. Veh denotes DMSO. Enzalutamide (Enz), apalutamide (Apa) and darolutamide (Daro) all denotes dosage of 10 µM. Mean ± SEM is represented, and p values were calculated using multiple t tests, 3 biological replicates in each group. (E) Tumor growth curve of xenografted LNCaP/AR cells transduced with annotated shRNAs. Enz denotes 10 mg/kg orally one day after grafting. Veh denotes 0.5% CMC + 0.1% Tween 80 at same dosage. Mean ± SEM is represented, and p values were calculated using two-way ANOVA. Experiments have been done with two independent repeats. (F) Relative cell number of LNCaP/AR cells transduced with annotated guide RNAs, normalized to shNT+Veh group. Cells were treated with 10 µM enzalutamide (Enz) or DMSO (Veh) for 7 days and cell numbers were counted. Mean ± SEM is represented, and p values were calculated using multiple t tests, 3 biological replicates in each group. (G) Relative gene expression level of *CHD1* in LNCaP/AR cells transduced with annotated inducible shRNAs at various time points. Mean ± SEM is represented, p values were calculated by one-way ANOVA, compared to 0 hr condition, 3 technical replicates in each group. (H) Relative cell number of LNCaP/AR cells transduced with annotated shRNAs in an inducible vector system, normalized to shNT+Veh. Cells were treated with 250 ng/ml doxycycline (Dox) for 48 hours, and then treated with 7 days of 10 µM enzalutamide (Enz) or DMSO (Veh), and cell numbers were counted. Mean ± SEM is represented, and p values were calculated using multiple t tests, 3 biological replicates in each group. (I) Relative cell number of LNCaP/AR cells transduced with annotated shRNAs in an inducible vector system, normalized to shNT+Veh. Cells were treated with 250 ng/ml doxycycline (Dox) for 48 hours, removed doxycycline for 7 days, and then treated with 7 days of 10 µM enzalutamide (Enz) or DMSO (Veh), then cell numbers were counted. Mean ± SEM is represented, and p values were calculated using multiple t tests, 3 biological replicates in each group. For all panels, **** $p<0.0001$. *** $p<0.001$. ** $p<0.01$. * $p<0.05$.

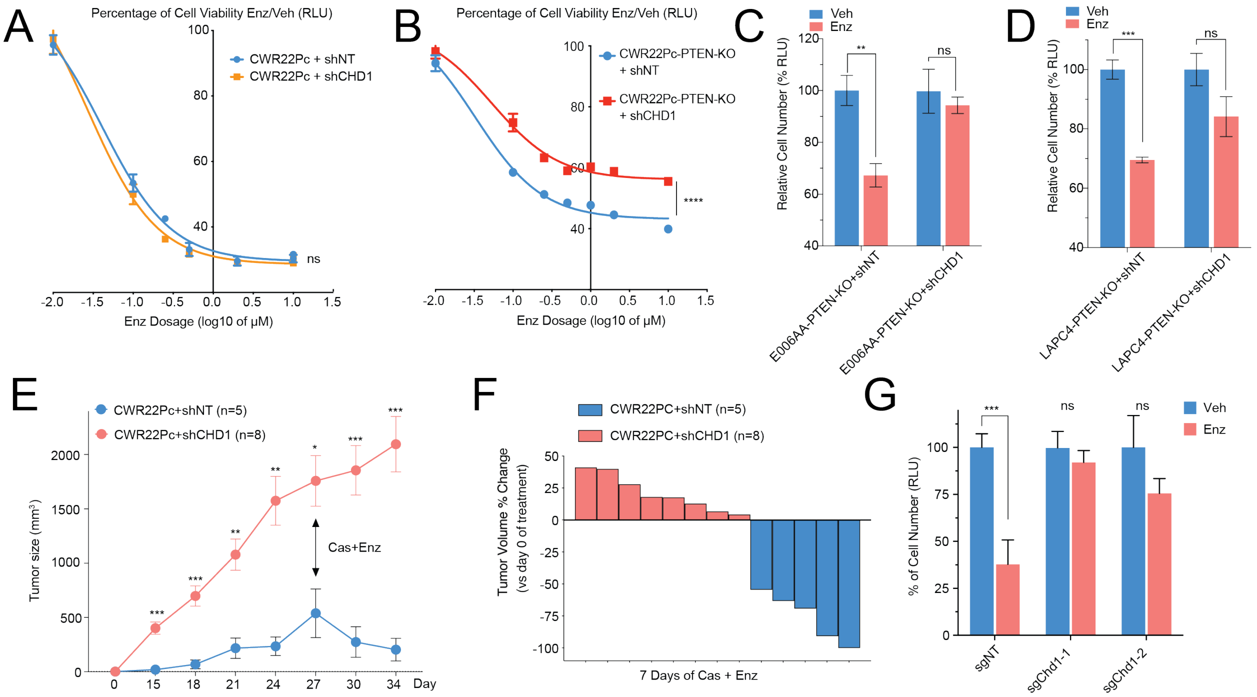

**Figure S3 related to Figure 3. *CHD1* KD confers resistance in other PCa models.** (A) Enzalutamide (Enz) dose response curve of CWR22Pc cells transduced with annotated shRNAs. Mean ± SEM is represented, and p values were calculated by non-linear regression with extra sun-of-squares F test, 3 biological replicates were used for each data point. (B) Enzalutamide (Enz) response curve of CWR22Pc-PTEN-KO cells transduced with annotated shRNAs. Mean ± SEM is represented, and p values were calculated by non-linear regression with extra sun-of-squares F test, 3 biological replicates were used for each data point. (C) Relative cell number of E006AA-PTEN-KO cells transduced with annotated hairpins. Cells were treated with 15 µg/ml enzalutamide (Enz) or DMSO (Veh) for 6 days in 3D Matrigel and cell number was measured using CellTiter-Glo assay. Mean ± SEM is represented, and p values were calculated using multiple t tests, 3 biological replicates in each group. (D) Relative cell number of LAPC4-PTEN-KO cells transduced with annotated hairpins. Cells were treated with 30 µg/ml enzalutamide (Enz) or DMSO (Veh) for 6 days and cell number was measured using CellTiter-Glo assay. Mean ± SEM is represented, and p values were calculated using multiple t tests, 3 biological replicates in each group. (E) Tumor growth curve of xenografted CWR22Pc cells in intact mice. All animals were castrated (Cas) and treated with enzalutamide (Enz) at 10 mg/kg orally from day 27. Mean ± SEM is represented and p values were calculated using two-way ANOVA. (F) Waterfall plot displaying changes in tumor size of xenografted CWR22Pc cells after 1 week of castration and enzalutamide treatments. Cas denotes castration. Enz denotes enzalutamide treatment at 10 mg/kg orally. (G) Relative cell number of mouse organoid (*Pten*$^{-/-}$) cultured in 3D. Organoids were treated with DMSO (Veh) or 1 µM enzalutamide (Enz) for 6 days. Mean ± SEM is represented, and p values were calculated using multiple t tests, 3 biological replicates in each group. For all panels, **** $p<0.0001$. *** $p<0.001$. ** $p<0.01$. * $p<0.05$.

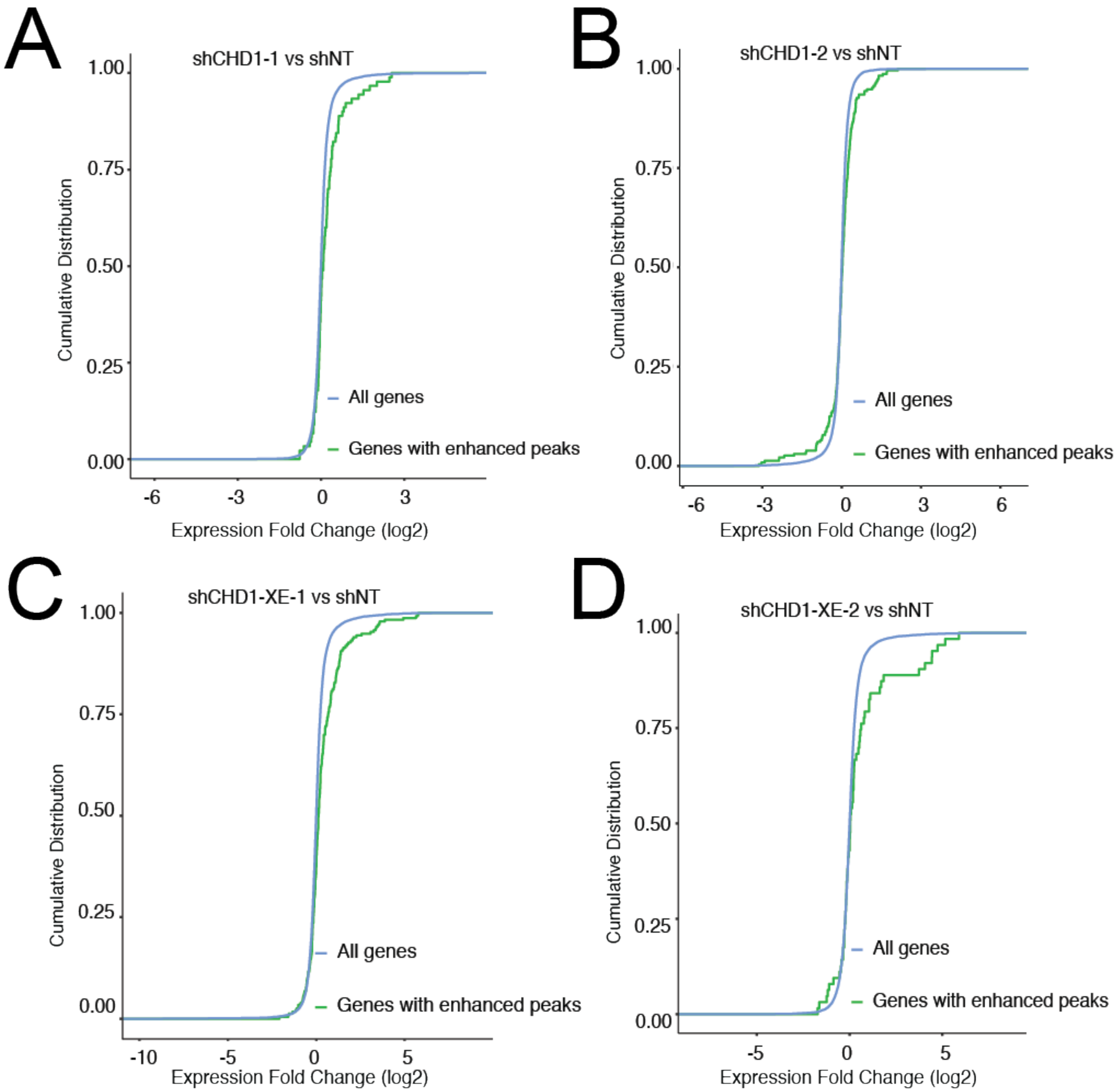

**Figure S4 related to Figure 5. ATAC-seq analysis reveals global changes in chromatin accessibility after *CHD1* loss.** (A-D) Cumulative distribution of log2 expression changes in shCHD1-1 cell line compared to shNT(A); shCHD1-2 cell line compared to shNT (B); shCHD1-XE-1 cell line compared to shNT (C); shCHD1-XE-2 cell line compared to shNT (D). For all panels, the blue line denotes all of the expressed genes. Green line denotes the genes with significant upregulated ATAC-peaks compared to shNT (enhanced peaks, combined increasing of peaks>6). For all panels, reads from 3 biological replicates were pooled to calculated the consensus peaks.

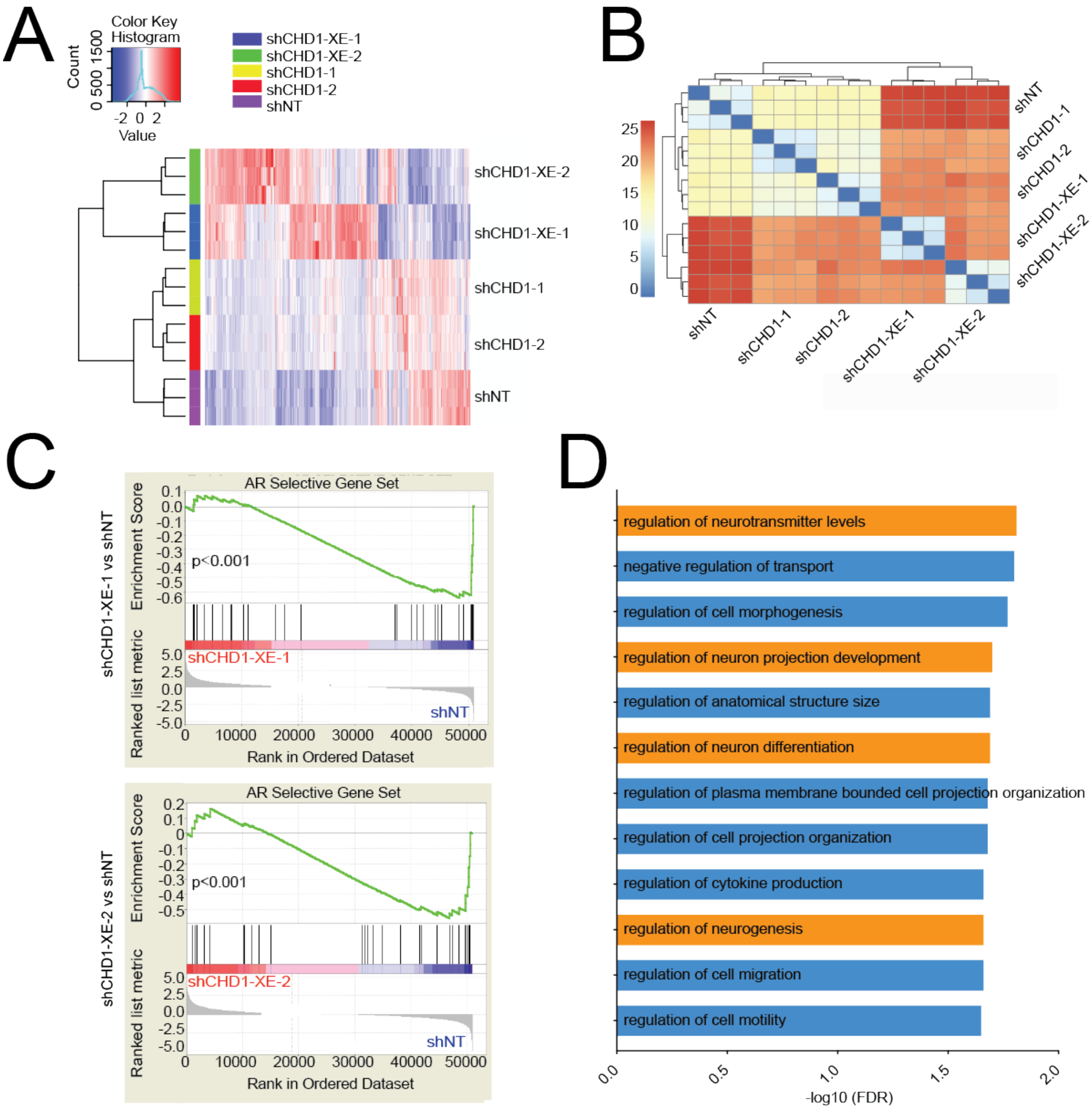

**Figure S5 related to Figure 5. RNA-seq analysis reveals global changes in transcriptome profiling after *CHD1* loss.** (A) Unsupervised hierarchical clustering of normalized expression of differentially expressed genes whose expression was significantly changed in any of the four other cell lines (shCHD1-1, shCHD1-2, shCHD1-XE-1, shCHD1-XE-2) comparing to shNT. 3 biological replicates in each group are shown. (B) Heatmap depicting the Euclidean distances between samples based on Pearson correlation. Reads from 3 biological replicates in each group were used for analysis. (C) GSEA analysis of AR selected genes (Arora et al. 2013) expression in shCHD1-XE groups compared to shNT group. Reads from 3 biological replicates were used for analysis. (D) Pathways enriched in the overlapped 150 significantly upregulated genes (see also Figure 5E) in the four cell groups compared to shNT. Reads from 3 biological replicates in each group were used for analysis.

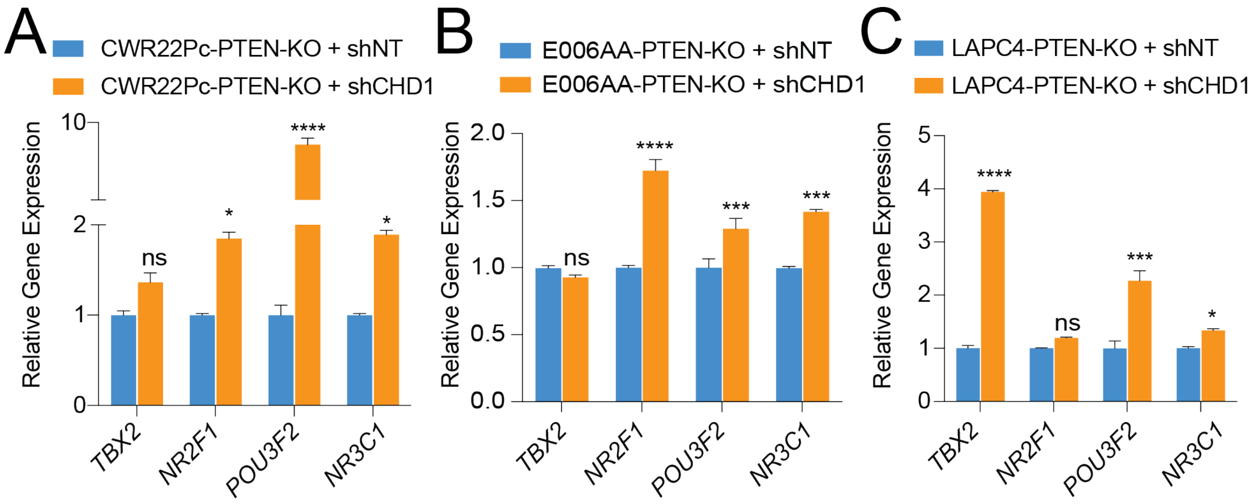

**Figure S6 related to Figure 6. *CHD1* loss leads to induction of 4 TFs in other PCa models.** (A) Relative gene expression of 4 TFs in CWR22Pc-PTEN-KO cells transduced with annotated shRNAs, all normalized and compared to shNT. (B) Relative gene expression of 4 TFs in E006AA-PTEN-KO cells transduced with annotated shRNAs, all normalized and compared to shNT. (C) Relative gene expression of 4 TFs in LAPC4-PTEN-KO cells transduced with annotated shRNAs, all normalized and compared to shNT. For all panels, mean ± SEM is represented and p values were calculated by multiple t test, 3 technical replicates in each group and **** $p<0.0001$. *** $p<0.001$. ** $p<0.01$. * $p<0.05$.

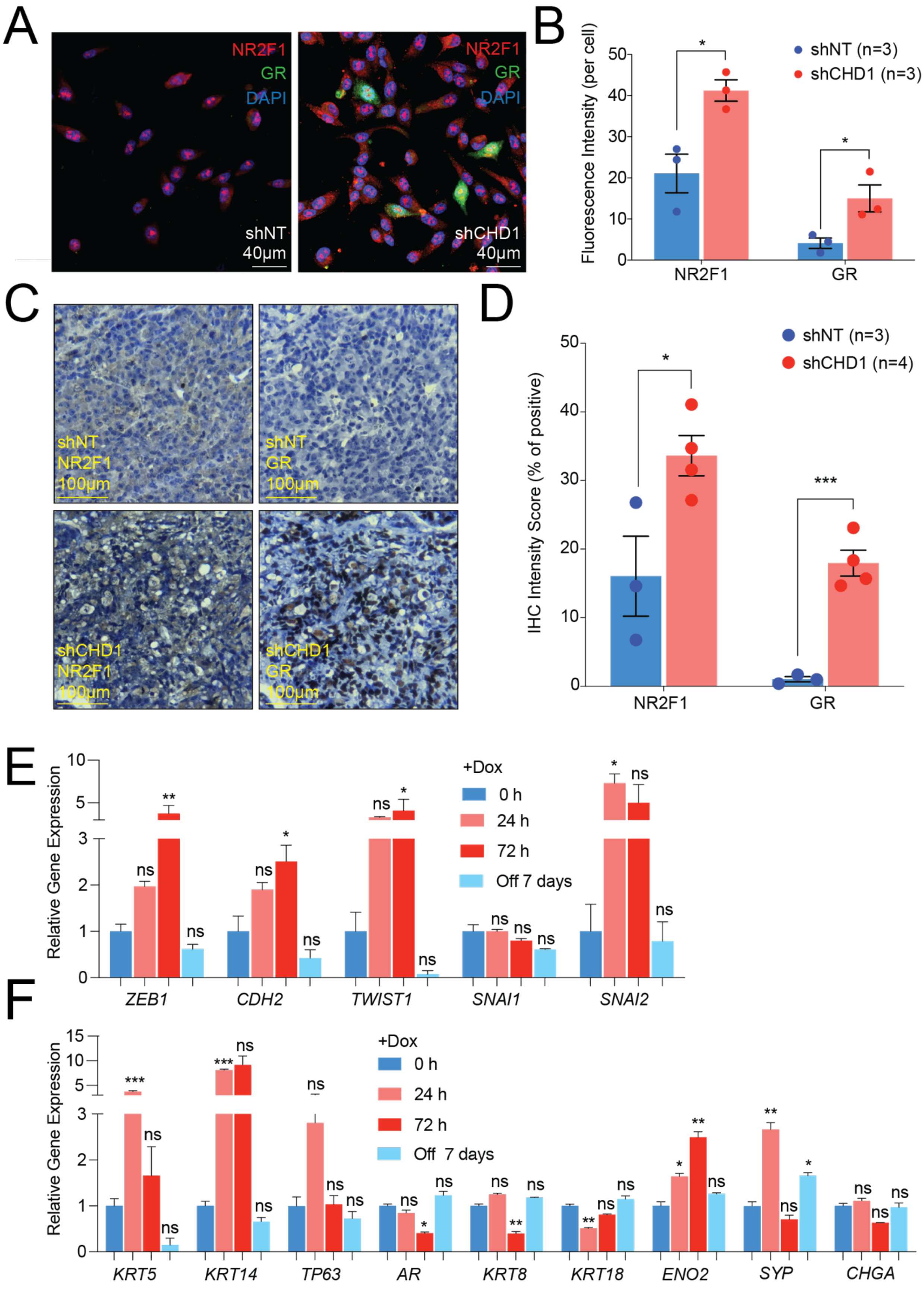
A
NR2F1
GR
DAPI
shNT
40µm
NR2F1
GR
DAPI
shCHD1
40µm
B
Fluorescence Intensity (per cell)
50
40
30
20
10
0
*
*
shNT (n=3)
shCHD1 (n=3)
NR2F1
GR
C
shNT
NR2F1
100µm
shNT
GR
100µm
shCHD1
NR2F1
100µm
shCHD1
GR
100µm
D
IHC Intensity Score (% of positive)
50
40
30
20
10
0
*
***
shNT (n=3)
shCHD1 (n=4)
NR2F1
GR
E
Relative Gene Expression
10
5
3
2
1
0
+Dox
0 h
24 h
72 h
Off 7 days
ns
**
ns
ns
*
ns
ns
*
ns
ns
ns
ns
*
ns
ns
ZEB1
CDH2
TWIST1
SNAI1
SNAI2
F
Relative Gene Expression
15
10
5
3
2
1
0
+Dox
0 h
24 h
72 h
Off 7 days
***
ns
ns
***
ns
ns
ns
ns
ns
ns
*
ns
ns
**
ns
**
ns
ns
*
**
ns
**
ns
*
ns
ns
ns
KRT5
KRT14
TP63
AR
KRT8
KRT18
ENO2
SYP
CHGA

**Figure S7 related to Figure 7. *CHD1* loss enhanced prostate cancer cell heterogeneity and lineage plasticity.** (A) Immunofluorescence staining of NR2F1 and GR in shCHD1-XE cells. (B) Quantification of representative immunofluorescence images. Mean ± SEM is represented and p value was calculated by multiple t test. (C) Immunohistochemical staining of NR2F1 and GR on shCHD1 enzalutamide resistant tumor slides. (D) Quantification of representative immunohistochemical images. Mean ± SEM is represented and p value was calculated by multiple t test. (E-F) Relative gene expression level of the EMT genes (E) and lineage specific marker genes (F) in LNCaP/AR cells transduced with annotated inducible shRNAs at various time points. Mean ± SEM is represented and p values were calculated by two-way ANOVA, all compared to 0 hr, 3 technical replicates in each group. For all panels, **** $p<0.0001$. *** $p<0.001$. ** $p<0.01$. * $p<0.05$.

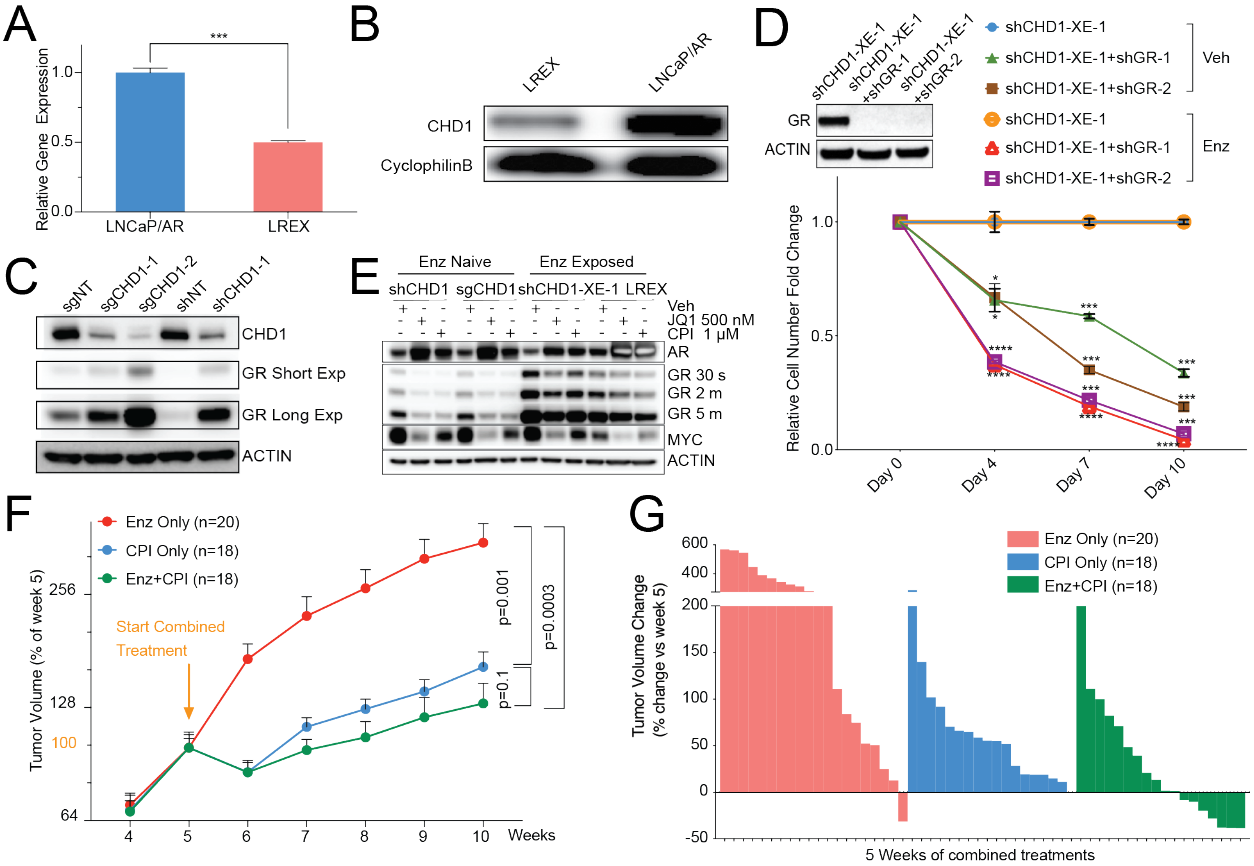

**Figure S8 related to Figure 8. BET Bromodomain inhibition restores enzalutamide sensitivity.** (A) Relative gene expression level of the *CHD1* in LNCaP/AR and LREX cells. Mean ± SEM is represented and p values were calculated by t test, 3 technical replicates in each group. (B) Western blot showing CHD1 protein levels in LNCaP/AR and LREX cells. (C) Western blot showing GR protein levels in LNCaP/AR cells transduced with annotated shRNAs or sgRNAs. (D) Relative cell number fold change compared to shCHD1-XE-1 group, based on the results of FACS-based competition assay. p values were calculated using two-way ANOVA. Mean ± SEM is represented and p values were calculated by two-way ANOVA, all compared to shCHD1-XE-1+Veh, 3 biological replicates in each group. Western blot showing GR protein levels in shCHD1-XE-1 cells transduced with annotated shRNAs. (E) Western blot of AR, GR, and MYC protein levels in different cell lines with enzalutamide resistance. (F) Tumor growth curve of xenografted LNCaP/AR shCHD1-XE-1 cells. All animals were treated with enzalutamide at 10 mg/kg orally 1 day after grafting. Beginning from week 5 of xenografting, animals were randomized into 3 groups and treated with enzalutamide only (Enz), CPI-0610 only (CPI) or the combination of enzalutamide plus CPI-0610. Mean ± SEM is represented and p values were calculated using two-way ANOVA. (G) Waterfall plot displaying changes in tumor size of xenografted LNCaP/AR shCHD1-XE-1 cells after 3 weeks of treatments. For (F) and (G), Enz denotes enzalutamide treatment at 10 mg/kg orally. CPI denotes CPI-0610 treatment at 60 mg/kg orally. For all panels, **** $p<0.0001$. *** $p<0.001$. ** $p<0.01$. * $p<0.05$.